5-12-2005

Continuous Late Pleistocene Paleoclimate Record from the Southwest African Margin: A Multi-Proxy Approach

Julia Keegan Shackford

CONTINUOUS LATE PLEISTOCENE PALEOCLIMATE RECORD
FROM THE
SOUTHWEST AFRICAN MARGIN: A MULTI-PROXY APPROACH

by
JULIA KEEGAN SHACKFORD

Under the Direction of Beth A. Christensen

ABSTRACT

Late Pleistocene sediments recovered from ODP Leg 175, Site 1085 are used to generate a high-resolution (500 yr) record of continental climate change in Southern Africa. The location of Site 1085, the SW African continental slope, provides a continuous hemipelagic section with a significant terrigenous component. Terrigenous sediments are transported via fluvial and/or eolian transport mechanisms with MIS 1 being dominated by eolian transport. Analyses, including grain-size, color reflectance, biogenic sediment geochemistry (%$CaCO_3$, %TOC, and C/N), bulk sediment geochemistry, and clay mineralogy, are used to identify continental climate conditions in southern Africa. Analyses indicate glacial/interglacial variation. Median grain-size peaks are associated with changes in transport. Clay mineralogy indicates the presence of kaolinite, smectite, and illite in varying percentages. Smectite and illite dominate the clay mineral assemblages except during MIS 2. Maximum kaolinite was found during MIS 2 and is associated with poleward transport by the Angola Counter Current.

INDEX WORDS: Benguela, Clay mineralogy, MIS, Multi-proxy, Paleoclimate, Pleistocene, Productivity, South Africa, Upwelling

CONTINUOUS LATE PLEISTOCENE PALEOCLIMATE RECORD FROM THE SOUTHWEST AFRICAN MARGIN: A MULTI-PROXY APPROACH

by

JULIA KEEGAN SHACKFORD
Colgate University, A.B. 2003

A Thesis Submitted in Partial Fulfillment of Requirements for the Degree of

Master of Science

Georgia State University

2005

CONTINUOUS LATE PLEISTOCENE PALEOCLIMATE RECORD FROM THE SOUTHWEST AFRICAN MARGIN: A MULTI-PROXY APPROACH

by

JULIA KEEGAN SHACKFORD

Major Professor:	Beth A. Christensen
Committee:	W. Crawford Elliott
	Eirik J. Krogstad
	Deborah Freile
Department Chair:	Timothy E. La Tour

Electronic Version Approved:

Office of Graduate Studies
College of Arts and Sciences
Georgia State University
May 2005

TABLE OF CONTENTS

ACKNOWLEDGEMENTS

This study was funded by a grant from the Georgia State University Research Program Enhancement to Drs. Christensen, Elliott, and Williams. I thank Dr. Beth Christensen, my thesis advisor, for all of her help, support, direction, and encouragement with this project. I thank Dr. Crawford Elliott for his help with the clay mineralogical analyses and instruction. I also thank Dr. Deborah Freile for all of her help and comments on my thesis, as well as her participation on my thesis committee. I would also like to thank Dr. Eirik Krogstad for his participation on my committee. I thank Eric Tappa at the University of South Carolina for help with and analysis of biogenic sediment geochemistry. I thank Mark Shaffer and Ryan Perry for their help in sample preparation, as well as Julian Gray for his help with quantitative clay mineralogical analysis. I thank my friends for all of their support and encouragement. Finally, I thank my parents, Paul and Barbara Shackford, and my sister, Kathryn, for all of their love, encouragement, and support throughout everything I have done.

LIST OF TABLES

LIST OF FIGURES

LIST OF ABBREVIATIONS

AAIW	Antarctic Intermediate Water	XRD	X-ray diffraction
AC	Angola Current	Å	Angstrom
ACC	Angola Counter Current	α	Alpha
ABF	Angola-Benguela Front	Δ	Delta
APF	Antarctic Polar Front	FWHM	full width-half maximum
BC	Benguela Current	kV	kilovolt
BOC	Benguela Oceanic Current	λ	wavelength
BCC	Benguela Coastal Current	mA	milliamp
CDW	Circumpolar Deep Water	(00*l*)	Miller Index
NADW	North Atlantic Deep Water	θ	theta
ITCZ	Inter-Tropical Convergence Zone	ºC	degrees Celsius
bsf	below seafloor	IR	Intensity ratio (5Å/10Å) of clay diffraction peaks
SH	Southern Hemisphere		
DSDP	Deep Sea Drilling Project	g	gram
ODP	Ocean Drilling Project	mL	milliliter
cm	centimeter	N	normality
μm	micrometer	C/N	Carbon to nitrogen ratio
mm	millimeter	Cu	Copper
m	meter	$CaCl_2$	Calcium chloride
nm	nanometer	$CaCO_3$	Calcium carbonate
ICP-AES	Inductively coupled plasma-atomic emission spectrometry	CO_2	carbon dioxide
My	million years	H_2O_2	Hydrogen peroxide
ky	thousand years	NaOAc	sodium-acetate acetic acid buffer
MIS	Marine Isotope Stage		
T1	Termination 1 – boundary between MIS 2 and 1	TOC	total organic carbon
		MAR	mass accumulation rate
T2	Termination 2 – boundary between MIS 6 and 5	BAR	bulk accumulation rate

CHAPTER 1: INTRODUCTION

1.0 Objectives

The primary objective of this study is to develop an understanding of southern African climate change during the late Pleistocene by establishing a continuous high-resolution late Pleistocene continental paleoclimate record for the southwest African margin. This is the first record of its kind for southern Africa and uses the terrigenous component of marine sediment as terrestrial climatic proxies to determine the geochemical, sedimentological, and clay mineralogical variations over the past 150 ky. Due to the location of the study area, offshore of the Orange River (29º22'S – 13º59'E; 1713 m water depth), analysis of the recovered marine sediments provides insight into relative differences in sedimentation rates and continental weathering in southern Africa. The results provide data (records of clay mineralogy, textural analysis and biogenic sediment geochemistry) to reconstruct late Pleistocene South African paleoclimatic changes using a multi-proxy approach. These proxies are listed in Table 1.1.

TABLE 1.1 Paleoclimate proxies used in this study

Proxy	Method	Interpretation			Reference
Clay Mineralogy	X-ray Diffraction	Source Region:	Transport Mechanism:	Clay Assemblage:	Diekmann et al., 1999
		Northern Angola Basin	Aerosol dust	kaolinite	Petschick et al., 1996
		Northern Angola Basin	ACC from Congo River	kaolinite	
		Guinea Basin	Tradewinds (?)	illite	Petschick et al., 1996
		Walvis Ridge	ACC	smectite	Petschick et al., 1996
		Angola	ACC	illite, kaolinite, smectite	
		Southern Africa	BC	illite, kaolinite	Petschick et al., 1996
		Southern Africa	NADW	illite, kaolinite (?)	Petschick et al., 1996
		Southern Africa	CDW	illite, kaolinite, smectite	Petschick et al., 1996
		Southern Africa	AAIW	Al-illite, smectite	Petschick et al., 1996
		Southern Africa	Agulhas Current	kaolinite	Rau et al., 2002
		Clay:	Properties:		
		Illite	5A/10A Intensity Ratio (0.45 - 0.60) - CDW, NADW, high mixing		Petschick et al., 1996
		Illite	5A/10A Intensity Ratio (> 0.60) - aerosols, rivers, NADW (?)		Petschick et al., 1996
		Illite	5A/10A Intensity Ratio < 0.05 - Fe (+Mg)-rich		Petschick et al., 1996
		Illite	5A/10A Intensity Ratio > 0.60 - Al-rich		Petschick et al., 1996
		Illite	d-spacing (9.98 - 10.1) - ACC from Angola Basin		Petschick et al., 1996
		Illite	d-spacing > 10.1 - CDW, AAIW		Petschick et al., 1996
		Illite	d-spacing < 9.98A - Muscovite-type		Petschick et al., 1996
		Illite	d-spacing > 10.1A - Biotite-type		Petschick et al., 1996
		Illite	IB $\Delta^{o}2\theta$ (crystallinity) (0.50 - 0.65) - NADW		Petschick et al., 1996
		Illite	IB $\Delta^{o}2\theta$ (0.65 - 0.80) - BC, CDW, AAIW, NADW (?)		Petschick et al., 1996
		Illite	IB $\Delta^{o}2\theta$ > 0.80 - CDW, AAIW		Petschick et al., 1996
		Illite	IB $\Delta^{o}2\theta$ < 0.35 - more crystalline		Petschick et al., 1996
		Illite	IB $\Delta^{o}2\theta$ > 0.8 - less crystalline		Petschick et al., 1996
		Smectite	IB $\Delta^{o}2\theta$ (1.0 - 1.5) - AAIW		Petschick et al., 1996
		Smectite	IB $\Delta^{o}2\theta$ (1.5 - 2.0) - CDW, NADW		Petschick et al., 1996
		Smectite	IB $\Delta^{o}2\theta$ < 1.0 - more crystalline		Petschick et al., 1996
		Smectite	IB $\Delta^{o}2\theta$ > 2.5 - less crystalline		Petschick et al., 1996

TABLE 1.1 (continued)

Proxy	Method		Interpretation	Reference
Grain Size	Grain-size Analyzer following digestion of organic material and $CaCO_3$	Transport Mechanism:	Grain Sizes:	
		Eolian	< 4μm, distal from continental source	Rea and Hovan, 1995; Joseph et al., 1998
			Negatively skewed normal grain size distribution	Rea and Hovan, 1995; Joseph et al., 1998
			< 2μm, long term suspension over large vertical range	Sun et al., 2002
			Median grain size < 6μm, proximal to source	Stuut et al., 2002
		Fluvial	< 4μm, closer to continental source	Rea and Hovan, 1995; Joseph et al., 1998
			Extremely platykurtic, bimodal grain size distribution	Rea and Hovan, 1995; Joseph et al., 1998
			Partially overlapping coarse & fine components	Sun et al., 2002
			Median grain size > 6μm, distal from source	Stuut et al., 2002
Weight % Sand	Material remaning in <63 μm sieve following washing with DI water	Indicating:	Response:	
		Productivity	Increased weight % sand with increased surface productivity	Diester-Haass et al., 2002
			Increased productivity with younger AAIW	
		Dissolution	Decreased weight % sand due to dissolution by NADW	Berger et al., 1998
		Dilution	Decreased weight % sand due to an influx of other material	Diester-Haass et al., 2002
Percent $CaCO_3$	Perkin Elmer 2400 Elemental Analyzer and JY Horiba Ultima-C ICP-AES	Indicating:	Response:	
		Productivity	Increased $\%CaCO_3$ with increased surface productivity	Diester-Haass et al., 2002
			Increased $\%CaCO_3$ associated with light-color sediment layers	Robinson et al., 2002
		Dissolution	Decreased $\%CaCO_3$ due to corrosive, older water	Diester-Haass et al., 2002
		Dilution	Decreased $\%CaCO_3$ due to an influx of other material	Diester-Haass et al., 2002

TABLE 1.1 (continued)

Proxy	Method	Interpretation			Reference
C/N	Perkin Elmer 2400 Elemental Analyzer and JY Horiba Ultima-C ICP-AES	Indicating:	Source:	C/N Ratio:	
		Organic carbon origin	Pure marine algae	5 - 8	Meyers, 1994; Meyers, 1997
			Vascular land plants	$\geq$ 20	Meyers, 1994; Meyers, 1997
			Mixed source	~ 10 - 20	Meyers, 1994; Meyers, 1997
		Nitrogen	Nitrogen utilization yields very low or negative ratios		Robinson et al., 2002
		Refractory nitrogen	Carbon utilization or low productivity yields falsely high ratios		Robinson et al., 2002
		Decreased productivity - greater recycling of nitrogen with increased flux of TOC to seafloor			Twichell et al., 2002
Percent TOC	Perkin Elmer 2400 Elemental Analyzer and JY Horiba Ultima-C ICP-AES	Indicating:	Response:		
		Productivity	Decreased surface productivity with increased %TOC		Jahn et al., 2003
		Dilution	Increased %TOC can cause dilution of $\%CaCO_3$ and weight % sand		Jahn et al., 2003
			Increased %TOC associated with dark-color sediment layers		Robinson et al., 2002
Color Reflectance	Shipboard measurement of reflectance in 10 nm increments between 400 - 700 nm	Increased color reflectance positively correlates with increased $\%CaCO_3$, weight % sand			Vidal et al., 1998
		Decreased color reflectance positively correlates with increased %TOC, dark-sediment layers			Vidal et al., 1998

1.1 Study Area

During Ocean Drilling Project (ODP) Leg 175, a series of sites were drilled along the southwest African margin to investigate changes in the Angola-Benguela Current system throughout the Neogene (Wefer et al., 1998). Four of the Leg 175 sites (1084, 1085, 1086, and 1087) were drilled as part of a latitudinal transect from the present northern and southern boundaries of the Benguela upwelling system. ODP Leg 175 Site 1085B was selected for analysis in order to construct a paleoclimate record for the Southwest African Margin. The study area is located within the southern Cape Basin on the continental slope off of western Africa at ODP Leg 175, Site 1085 (29º22'S – 13º59'E) (Figure 1.1). The samples used are from core B and consist of the upper 7.2 m of hemipelagic sediment. The age model is based on the oxygen isotope record developed by Foote (2005) and tuned to orbital variations by Christensen. It is controlled by biostratigraphic data (Wefer et al., 1998).

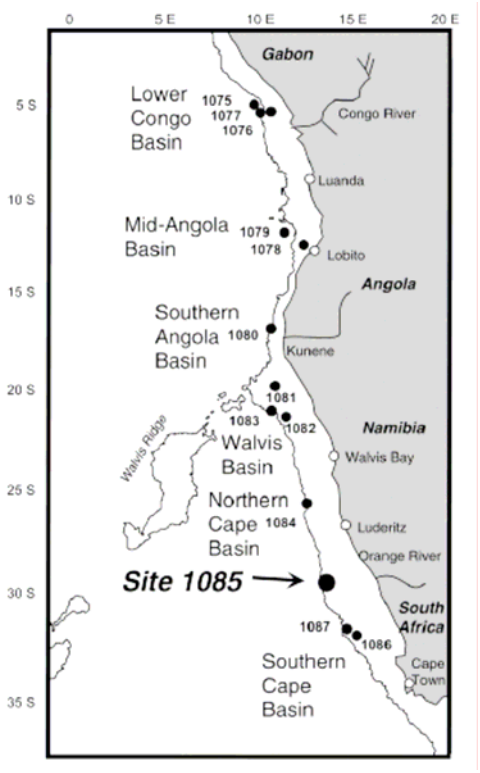

FIGURE 1.1: ODP Leg 175 sites, including the Site 1085 study area in the Cape Basin. Note, Site 1085 is on the slope, not the shelf as may be interpreted from the figure. (from Murray et al., 2002).

1.2 Oceanographic Setting

Through heat exchange and primary production, the Benguela Current (BC) system plays a significant role in global climate, exerting influence on the global carbon budget and atmospheric CO_2 (Wefer et al., 1999). The BC system includes the Benguela Oceanic Current (BOC) and the Benguela Coastal Current (BCC) and forms the northeastern limb of the anticyclonic gyre of the South Atlantic (Figure 1.2). The BOC is the equatorward drift of cooler surface waters from 34˚S to 23˚S. Around 23˚S the current diverges from the coast (Little et al., 1997). The BCC flows as far north as 14˚S, where it meets the Angola Current (AC) at the Angola-Benguela Front (ABF) (Jahn et al., 2003). There is also influence from the Agulhas

Current on the BC system (Rau et al., 2002). The dominant influence at 1713 m water-depth from the BC system is the BOC, since it is a deep-water site. Antarctic Intermediate Water (AAIW) and upper component North Atlantic Deep Water (NADW) also impact this water depth (Figure 1.3). The Angola Counter Current is a poleward surface current running along the shelf from the Angola Basin to the Cape Basin and provides a transport mechanism for bringing Angola Basin sediment to the study area.

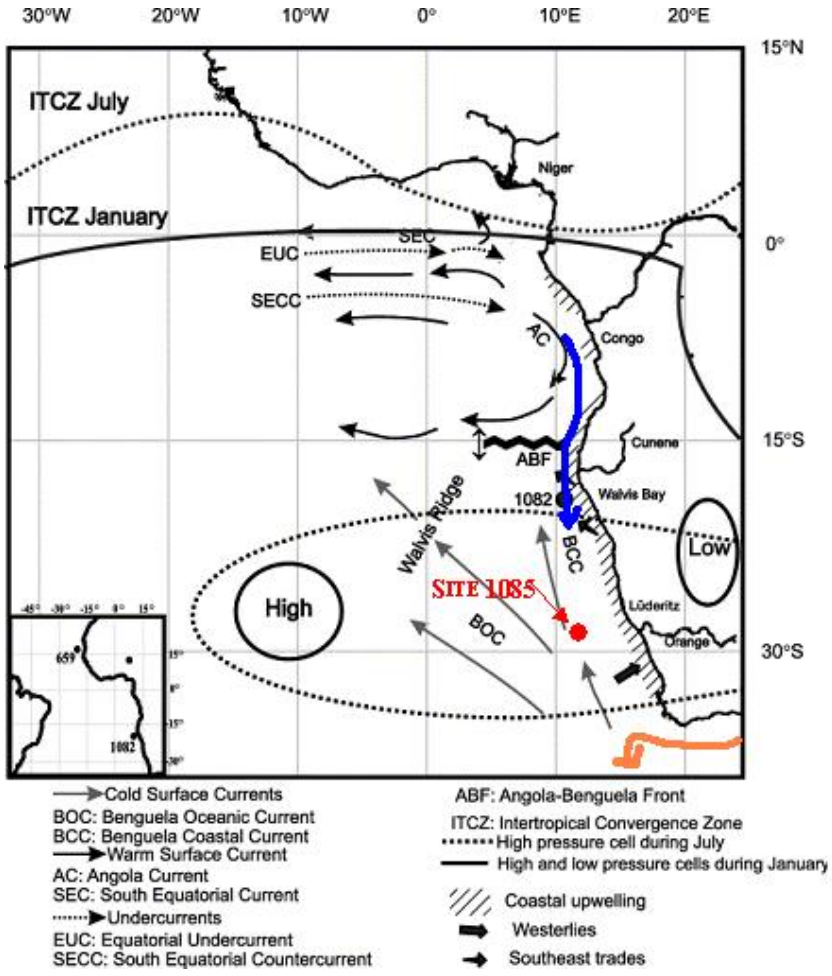

FIGURE 1.2: Oceanographic setting of the Cape and Walvis Basins. The poleward Angola Counter Current is shown in blue and the Agulhas Current Retroflection is shown in orange (modified from Jahn et al., 2003).

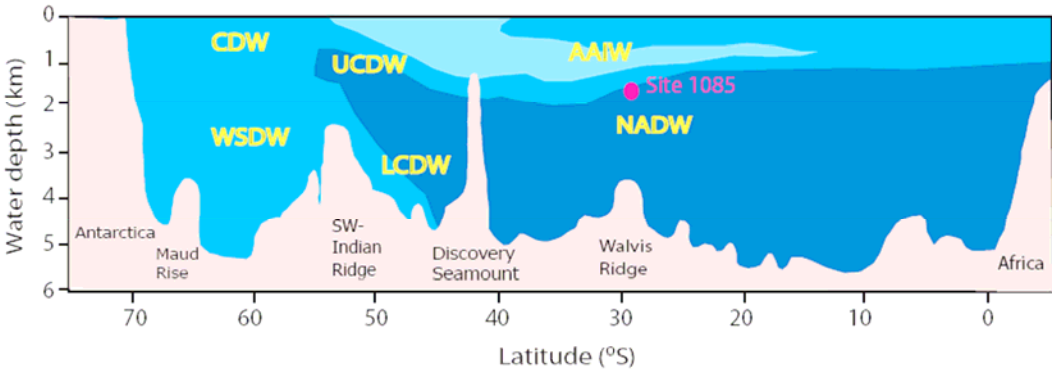

FIGURE 1.3: Water mass and location of Site 1085B (modified from Reid, 1989).

1.3 Atmospheric Circulation and Winds

Site 1085 is at the boundary of the westerlies and the southeasterly trade winds in a subtropical high-pressure belt (Figure 1.4). With the exception of surface winds, the mean circulation of the atmosphere over southern Africa is anticyclonic throughout the year with intensification and northward movement of the anticyclone during winter (Tyson and Preston-Whyte, 2000). Northward expansion and intensification of the circumpolar westerlies is also evident during winter months.

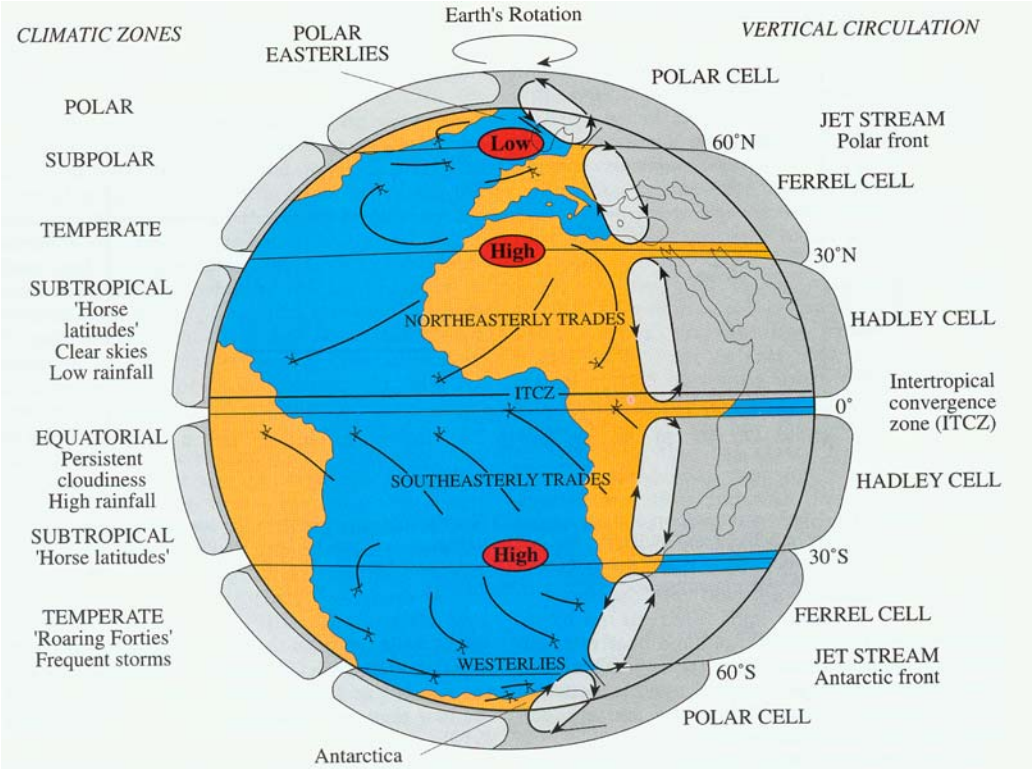

FIGURE 1.4: The six-cell model of global air circulation (from Charnook, 1996).

The Inter-Tropical Convergence Zone (ITCZ) is the area where the northeasterly trade winds meet the southeasterly trade winds and converge. Over Africa, the ITCZ migrates from the southern to the northern hemisphere between January and July (Figure 1.5) (Tyson and Preston-Whyte, 2000). The migration of the ITCZ causes seasonal intensification of ocean highs, affecting the ocean currents and upwelling. This causes increased upwelling in the BC and lower sea-surface temperatures along the coast (Tyson and Preston-Whyte, 2000).

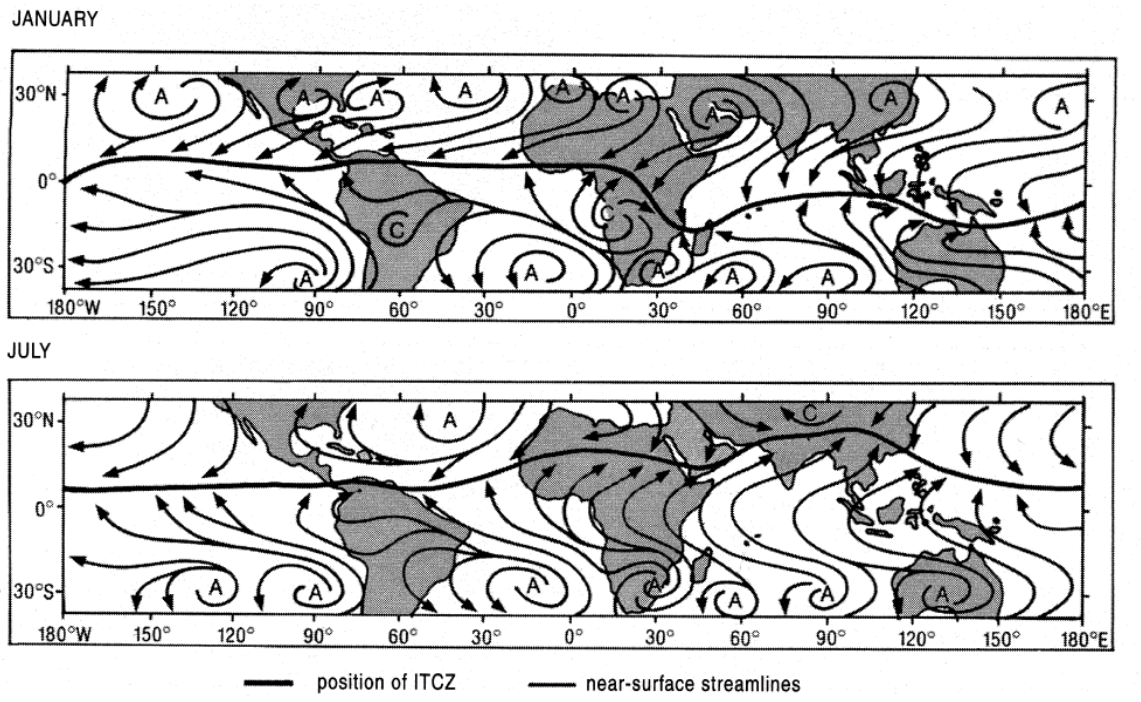

FIGURE 1.5: Schematic streamlines of near-surface flow showing mean inter-tropical convergence. A indicates an anticyclonic (counterclockwise) center, C indicates a cyclonic (clockwise) center. (from Tyson and Preston-Whyte, 2000)

A more local, yet extremely important part of the atmospheric circulation for the region are the Berg winds stemming from the Kalahari. These winds transport eolian material offshore, with some reaching the study area in the Cape Basin in visible plumes (Figure 1.6). Of course, there must be a dust supply to the study area. In areas with increased rainfall there is a reduced amount of dust particles available for transport due to vegetation stabilizing land surfaces (Pye, 1989). Finer sediment is more easily removed from more arid regions with less vegetation, resulting in a net increase in dust particle supply. Hyperarid regions are areas with < 100 mm annual rainfall and there is very little dust available for transport from these areas (Pye, 1989). This is due to the majority of smaller particles having already been blown away and little moisture to break down larger grains. Coarse weathering debris accumulates and stabilizes the

land surface (Pye, 1989). Variations in eolian accumulation rates provide evidence of the regional climate history of the source area (Hovan and Rea, 1992).

Berg winds occur in concert with coastal atmospheric lows initiated on the west coast and propagate towards Cape Town (Tyson and Preston-Whyte, 2000). These coastal lows produce warm offshore airflow ahead of the weather system and cool onshore airflow behind it. Berg winds are associated with the coastal weather system and the large-scale pre-frontal divergence and warming of subsiding air moving offshore with the anticyclonic curvature (Tyson and Preston-Whyte, 2000). These winds may blow for a few hours to a number of days and are most common in early spring and late winter (Tyson and Preston-Whyte, 2000).

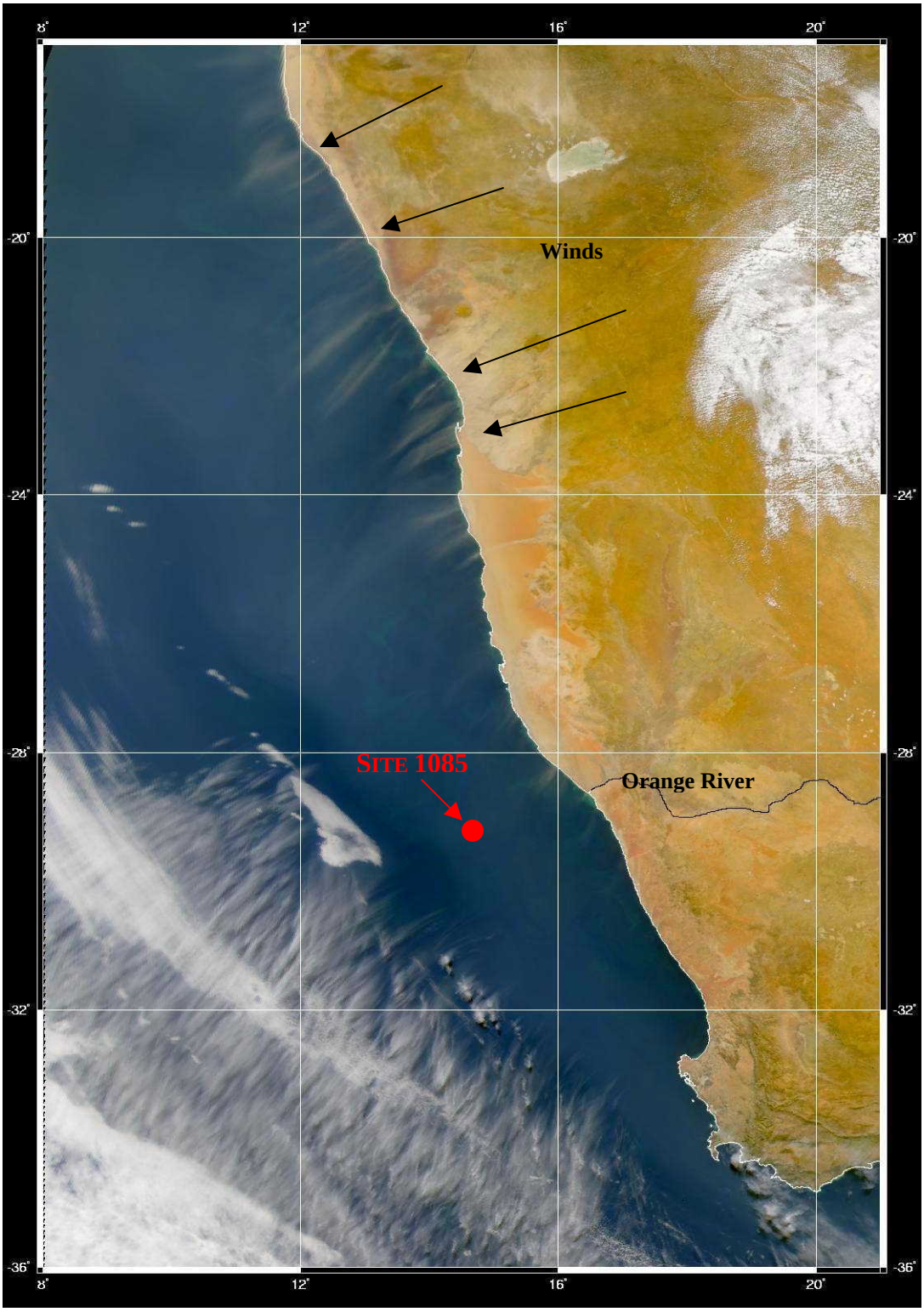

FIGURE 1.6: SeaWiFS photograph of dust plume over the South Atlantic (SeaWiFS, June 6, 2000).

1.3 Clay Mineralogy

Clay (phyllosilicate) mineralogical assemblages are useful in documenting source and transport of clastic material to marine study areas. Their role as paleoclimatic and paleoceanic indicators for the South Atlantic has been investigated using X-ray diffraction (XRD) techniques (Petschick et al., 1996). The Recent clay distribution is controlled by climatic and weathering zonation on the adjacent landmasses and the majority of the clays studied have a terrigenous origin. In arid regions, such as North and Southwest Africa, wind transport is the major process supplying terrigenous matter to the ocean (Petschick et al., 1996). However, Site 1085 is not proximal to the Kalahari Desert or significantly affected by Berg winds and is closely associated with the Orange River, so a fluvial contribution is anticipated. Clays can also be used to identify marine conditions as an alternative deep-water proxy to benthic foraminiferal proxies and carbonate preservation indices (Diekmann et al., 1999). Varying specific clay phyllosilicate ratios, such as kaolinite/illite, should indicate input and transport by different deeper water masses (AAIW, NADW) (Diekmann et al., 1999; Petschick et al., 1996) or by surface eolian input (via Berg winds and other air masses) and fluvial contribution (via the Orange River).

The dominant phyllosilicate clay minerals found in the Recent Cape Basin sediments are smectite and illite (Petschick et al., 1996) with some input by Agulhas Current leakage. The Agulhas Current brings warm, saline water from the Indian Ocean, around southern Africa. The current then kicks back, termed the Agulhas Current Retroflection, and eddies spin off, bringing some of that warm, saline Indian Ocean water to the Southern Cape Basin. Kaolinite is present as well, with periods of increased accumulation indicating potential changes in source and transport mechanism. Kaolinite and illite can have a continental source due to intense weathering of southern Africa. It is also possible to transport kaolinite and illite to the study site

from the Angola Basin via the poleward Angola Counter Current or via AAIW from the southwestern Atlantic and near Antarctica (Petschick et al., 1996). Smectite is generally volcanic and is brought in by Agulhas Current leakage around the Cape of Good Hope or via AAIW and CDW from the weathering of submarine basalt (Petschick et al., 1996).

1.5 Textural Analysis

Different grain-size populations are associated with particular transport and depositional mechanisms (Sun et al., 2002), and can reflect continental aridity and humidity (Stuut et al., 2002). At Site 1085, terrigenous sediment is transported via eolian and/or fluvial mechanisms. Changes in median grain-size downcore provide evidence not only of transport and depositional processes, but of continental climate as well.

In eolian sediment populations, there are coarse- and fine-grained components. The coarse-grained fraction of eolian sediment is transported via surface winds and moves in short suspension episodes (Sun et al., 2002). This results in the preferential deposition of this material downwind, yet adjacent to its source. The fine-grained or clay fraction (<2 μm) of eolian sediment is transported in a wide altitudinal range, mainly in the upper level of airflow (Sun et al., 2002). Deposition of this material is generally spread over a wider range and further from its source. Both types of material provide information about source and potentially have environmental significance. Eolian sediment transported to the deep sea is generally finer-grained (<2 μm) and transported by long term suspension over a large vertical range, as well as being deposited over a wide range (Sun et al., 2002). Farther from the continental source, the modal size of eolian suspension dust is smaller than dust deposited closer to the source or in shallower waters (Stuut et al., 2002).

Coarse- and fine-grained material is transported via fluvial transport mechanisms as well. Fluvial mechanisms can transport sediment in three ways: 1) suspension, 2) saltation, or 3) traction (bed load), depending on particle size (Sun et al., 2002). Suspended material has a smaller median grain-size than traction and saltation sediment owing to the ease of its transport. The traction and saltation sediment, therefore, will be preferentially deposited closer to its original source while the suspended load can be transported and deposited further away (Sun et al., 2002). When examining deep-sea sediment, changing grain-size and grain-size populations can be a proxy for changing wind and/or fluvial strength (Sun et al., 2002; Stuut et al., 2002).

The use of grain-size to determine sediment source is not straightforward. In the grain-size study most proximal to Site 1085, Stuut et al. (2002) uses median grain-size as a humidity proxy in which the flux of hemipelagic sediment to his study area on the Walvis Ridge (Figure 1.7) is associated with continental runoff. The end member model of terrigenous contribution to the site defines three end members. End members (EM) 1 and 2 have a larger median grain-size (>6 μm), while EM3 has a median grain-size of <6 μm (fine silts, very fine silts, and clays) and changes in the ratios between the three end members indicate changing continental paleoclimate in SW Africa. The eolian grains are interpreted to come from EM1 and EM2 and the fluvial grains from EM3 (hemipelagic), settled out of suspension from the nepheloid layers originating from ephemeral rivers that drain the Central Namib Desert and/or the Orange River to the south (Stuut et al., 2002). This interpretation is in contrast to many other studies, which indicate fine silt to very fine silts and clays are transported via hemipelagic mechanisms (Joseph et al., 1998).

The difference in interpretation is probably due to the strong winds and proximity of Stuut's (2002) site to the Kalahari. Changes in the ratio between the two eolian end members reflect changes in the intensity of the SE trade winds, with increased velocity of trade winds

during glacial periods as opposed to interglacials (Stuut et al., 2002). The record of aridity shows more arid conditions during interglacial periods and more humid conditions during glacials, as evidenced by EM1 and EM2 dominating in interglacial periods and EM3 dominating glacial periods. However, the trade winds less clearly impact Site 1085.

Because of the likely differences in study areas and their interpretations, a more conservative interpretation can also be explored using studies from other regions such as the North Pacific (Rea and Hovan, 1995), Bermuda Rise (Joseph et al., 1998) and Indian Ocean (Hovan and Rea, 1992). Grain-sizes between 2 and 4 μm are transported by upper atmospheric winds and are considered background eolian input to deep-sea sediment (Joseph et al., 1998; Rea and Hovan, 1995; Hovan and Rea, 1992). In the range of 1 to 30 μm, eolian grains show a distinct size mode of 2 μm, while hemipelagic grains have a flatter size distribution curve and a broader mode of 2 μm (Rea and Hovan, 1995). The dominant grain-size distribution at a classical hemipelagic site has a range of 6.5 to 16 μm (Joseph et al., 1998). Hemipelagic sites also exhibit a platykurtic, bimodal grain-size distribution while sites influenced more by eolian sediment transport exhibit a negatively skewed normal grain-size distribution (Figure 1.8) (Joseph et al., 1998; Rea and Hovan, 1995).

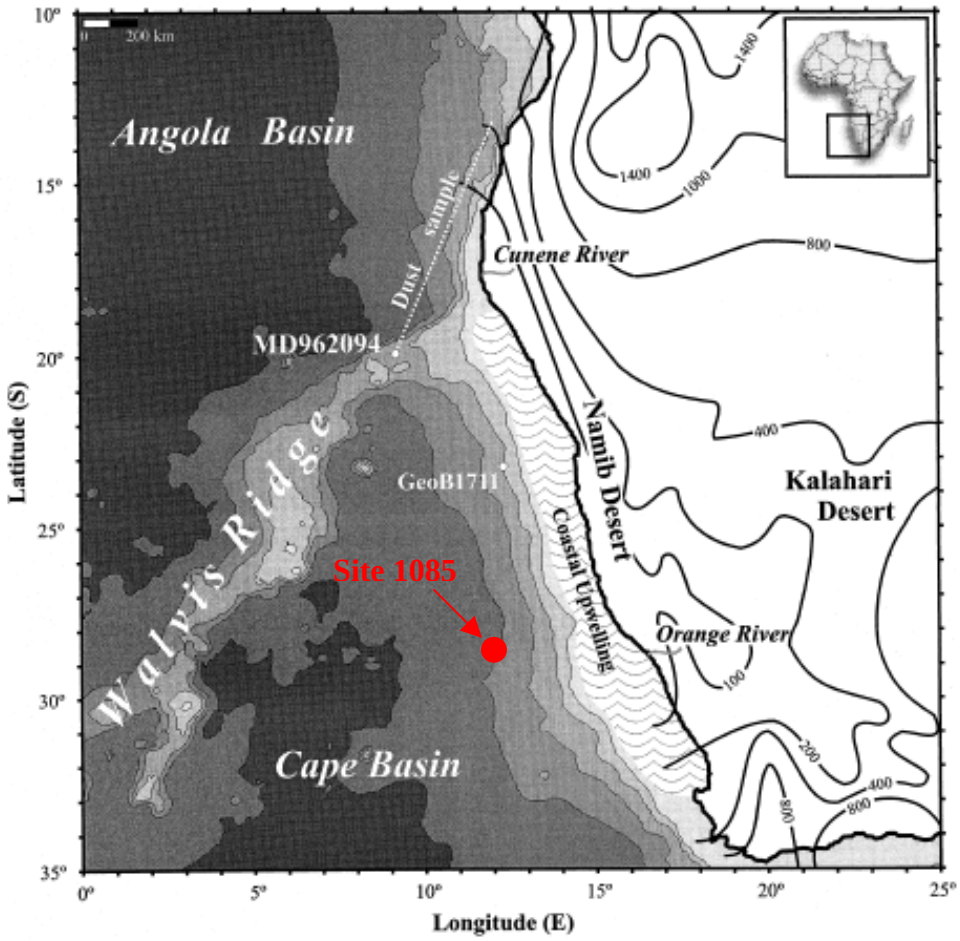

FIGURE 1.7: Location of cores MD962094 and GeoB 1711 (Little et al., 1997) in the SE Atlantic Ocean. The white dotted line shows the transect along which the present-day dust sample was collected. Bathymetry is shown in 1000 m contour intervals and annual rainfall is indicated in mm. The wavy lines indicate the zone of wind driven upwelling. (from Stuut et al., 2002)

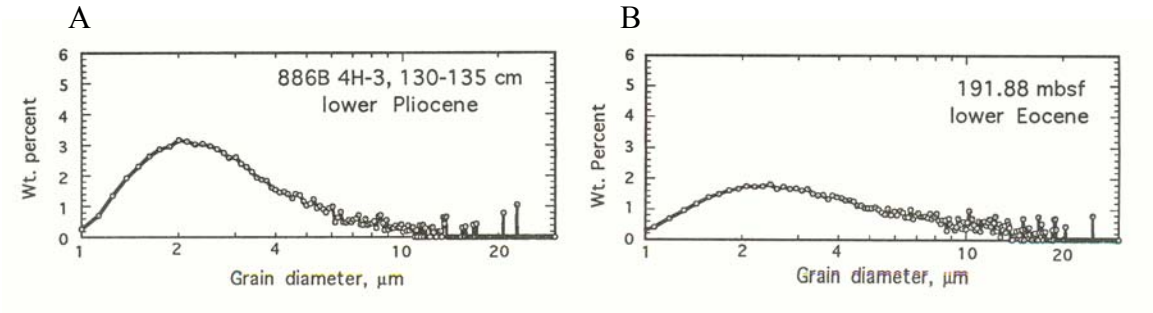

FIGURE 1.8: Typical grain-size distribution: (A) Mineral component from a pelagic clay core at ODP Site 886 exhibiting typical eolian grain-size distribution. (B) Mineral component from DSDP Site 527 exhibiting typical hemipelagic grain-size distribution (from Rea and Hovan, 1995).

1.6 Biogenic Sediment Geochemistry and Physical Properties

1.6.1 Weight Percent Sand and %$CaCO_3$

The reconstruction of paleoclimate in margin environments can be difficult because of the difficulty in separating the productivity signal from material transport downslope (dilution) and/or dissolution of carbonate microfossils (Diester-Haass et al., 2002). Weight percent sand, which at Site 1085 is a measure of the weight percent of foraminiferal tests, is used as a dilution/dissolution indicator and an increase in weight percent sand should show a corresponding increase in %$CaCO_3$. Changes in the dissolution of carbonate microfossils can be due to changes in paleoproductivity. Periods of darker sediment accumulation are considered a measure of dissolution due to increased productivity and transport of organic carbon to the study area. For example, an increase in the supply of organic matter can increase microbial respiration, which will increase carbonate dissolution (Diester-Haass et al., 2002). The oxygen content of bottom water, sedimentation rates, and depth of burial can also influence calcite dissolution, however Diester-Haass et al. (2002) found that the benthic foraminifera at Site 1085 were not markedly dissolved and it is possible, therefore, to use foraminifera as a productivity indicator.

$CaCO_3$ and TOC concentrations vary with sediment color and are found to have a strong inverse relationship at Sites 1082 and 1084 (Figure 1.1) (Robinson et al., 2002). Increased $CaCO_3$ indicates more oxic bottom waters, less dissolution, a smaller influx of reactive organic matter (TOC), and is characterized by lighter colored sediment layers. In contrast, darker sediment layers show increased TOC concentrations and imply greater dissolution of calcite (Robinson et al., 2002). Both TOC and $CaCO_3$ contribute to the $CaCO_3$ signal seen in marine sediments.

1.6.2 %TOC

The %TOC is also used as a paleoproductivity indicator (Jahn et al., 2003). In the northern BC (Site 1082, Figure 1.1), the magnitude of TOC can be influenced by three factors: 1) productivity in surface water; 2) filaments and eddies transporting organic carbon in surface waters; and 3) near-bottom supply during sea-level regressions. These same controls apply at Site 1085. At Site 1082, the TOC maxima do not correspond to glacial periods, rather they occur at glacial-interglacial transitions and occasionally during interglacials (Jahn et al., 2003). Although this atypical response is known from previous studies, Berger et al. (2002) concluded that marine productivity would be greatest during times when both physical upwelling and nutrient contents of upwelled subsurface waters were both sufficiently high. The enhanced TOC, therefore, is attributed to an increased marine paleoproductivity along the coast and in the filaments of upwelled surface waters, which do not always correspond to full glacial conditions (Jahn et al., 2003).

1.6.3 C/N

Source and paleoenvironmental information is preserved in the marine environment in the molecular, elemental, and isotopic composition of organic matter (Meyers, 1994). The C/N and $\delta^{13}C$ values undergo little change through diagenetic processes and therefore can be used to determine the original source of the sediment. The C/N ratio can be an identifier of the source of carbon found in the sediment, since marine algal C/N values range from 5 to 8 while vascular land plants have a C/N ratio $\geq$ 20 (Meyers, 1997). Thus, proportions of marine-derived and land-derived organic matter can be identified using C/N ratios.

Lake studies show that the bulk source character is preserved over long periods of time during which organic matter resides in sediment, even if that organic matter continues to

degrade, thereby allowing identification of source even after extensive degradation of the original organic matter (Meyers, 1994). The decrease in C/N ratios seen at Lake Baikal, Russia, indicates a shift from dominantly land-derived organic matter to a more mixed algal and land-derived source (Meyers, 1994). This change was accompanied by an increase in %TOC as productivity of the lake increased (Meyers, 1994). Lake Bosumtwi, Ghana, provides further evidence of the usefulness of this proxy. Analysis of a ~17m core shows no selective diagenesis affecting C/N ratios and variations of the C/N ratios record changes in delivery of land-derived organic matter to the lake as climate changed (Meyers, 1994).

Normally, organic matter accumulates more slowly and over a longer period of time in marine sediments than in lake sediments and therefore it is possible to record longer paleoclimatic histories in the marine realm. DSDP Site 619 is located in the Pygmy Basin in 2259 m water depth, within the northern Gulf of Mexico. Increased %TOC is found between 25 and 8 ky, corresponding to the maximum C/N values (Meyers, 1994). During this period, sediment from the Mississippi River dominated the area, thereby increasing the land-derived organic matter input and the C/N ratios. The changes in C/N ratios represent changes in the proportion of land-derived versus algal organic carbon (Meyers, 1994).

C/N ratios have been used closer to the Site 1085 study area as well. DSDP Site 532 is located on the Walvis Ridge in the South Atlantic, north of the Cape Basin. Sediments record enhanced marine productivity associated with the initiation of the Benguela Current upwelling system that began ~10 My (Siesser, 1980). Diester-Haass et al. (2002) found light-dark variations in color that could be linked to Milankovitch-type fluctuations in marine productivity. At this site, the C/N ratios seem to be higher than anticipated with an increase in marine productivity. These elevated C/N values would normally be indicative of increased land-derived

organic matter input, however there are several pieces of evidence to the contrary including: 1) the sparsely vegetated coastal Namib Desert can provide little organic matter; 2) there is little clastic input as the sediments are biogenic oozes; and 3) isotopic values indicate a marine source of organic matter (Meyers, 1994).

Another possibility for elevated C/N values could be a decreased amount of nitrogen available in the system, thereby leading to higher over all C/N ratios (Meyers, 1997). C/N ratios and TOC are used together to infer productivity and carbon origin at marine study sites (Robinson et al., 2002; Meyers, 1994). At Site 1082, an organic carbon-rich environment, higher C/N values correlate with higher TOC concentrations. This correlation is probably due to enhanced sedimentation of marine organic matter and therefore not necessarily a reliable indicator of organic matter source at this particular study site (Robinson et al., 2002). The elevated C/N ratios result from the selective loss of nitrogen as the organic matter settles out of the photic zone. In organic carbon-poor environments, a lower than expected C/N ratio is generally preserved due to the presence of excess nitrogen. In these areas, C/N elevations are most pronounced with high TOC concentrations, which indicate a higher rate of organic matter delivery leading to reduced relative degradation (Robinson et al., 2002).

C/N values of TOC generally retain source signatures for million-year time spans (Meyers, 1994). Since these values undergo little change through diagenetic processes, these ratios can be used as an identifier of the source of carbon to a marine system. Values ranging from 5 to 8 indicate a marine algal source, while values $\geq$ 20 indicate a land-derived source of organic matter (Meyers, 1997). Values between 8 and 20 therefore imply a mixed carbon source with varying proportions of marine and terrestrial carbon or the selective use of nitrogen in organic carbon-rich environments (Meyers, 1994 and 1997; Robinson et al., 2002).

1.6.4 Color Reflectance

Color reflectance data is a suitable proxy for reconstructing paleoproductivity and changes in carbonate sedimentation (Vidal et al., 1998). The color reflectance was measured aboard ship in 10nm increments between 400 and 700nm, the visible spectrum. The ratios between reflectance values of the red (650nm) and blue (450nm) wavelengths were also taken for each increment. The interpretation of the data comes from percent reflectance as a function of wavelength, so that even small and subtle changes in color, not visible to the naked eye, can be detected and are potentially due to lithologic changes (Vidal et al., 1998). Most lithologic changes in this study area are gradual and driven by changing concentrations of diatoms, nannofossils, and foraminifera.

Shipboard data indicate that the major control on color reflectance at Site 1085 is changing carbonate content, seen by a positive correlation between %$CaCO_3$ and color reflectance (Vidal et al., 1998). Site 1085 is a carbonate rich environment with > 20wt.% $CaCO_3$ so, color reflectance is high, regardless of individual red (650 nm) and blue (450 nm) wavelength bands (Vidal et al., 1998). For instance, the presence of pyrite downcore at site 1085 does not influence the reflectance spectrum by lowering values in the red band (Vidal et al., 1998). Individual layers with higher concentrations of organic carbon, however, generally have lower color reflectance, indicating that there is some control on color reflectance by %TOC. This positive correlation, especially during times of high total reflectance, indicates either better $CaCO_3$ preservation at those periods in time or higher marine productivity. Vidal et al. (1998) also found that cycles of total color reflectance exhibit orbital scale cyclicity, regardless of depth.

1.7 Previous African Climate Studies

A continuous sedimentary sequence is necessary to study climate change but, although some work has been done to develop the Pleistocene paleoclimate record in Southern Africa, there is no area on the continent with a continuous record of sedimentation during the Pleistocene. The majority of the records from Southern Africa are incomplete, as they come from discontinuous terrestrial sources, such as various caves and lake sediments (Russell et al., 2003) or are not sufficiently long enough to document climate change during the Pleistocene (Holmgren et al, 2003). In addition, they do not come from western South Africa or Namibia. Currently, the best record of Pleistocene paleoclimate for Southern Africa comes from the rainfall record in the Pretoria Saltpan (Partridge et al., 1997). Additional data are necessary because the majority of existing African records come from eastern and northern Africa and these regions have different climate controls than those controlling the continental input at Site 1085.

1.7.1 Late Pleistocene Paleoclimate

Global climates during the late Pleistocene were characterized by glacial/interglacial cycles in the higher latitudes, which impacted climates in the sub-tropics (Tyson and Preston-Whyte, 2000). Early in the Pleistocene, glacial/interglacial cycles followed a 41-ky periodicity due to changes in the Earth's obliquity. In the late Pleistocene, there was a shift in glacial/interglacial cycles to follow a 100-ky periodicity in response to changes in the Earth's eccentricity. There was also a 23-ky climate signal due to changes in the precession of the equinoxes.

1.7.2 Southern African Climate Studies

In Southern Africa, to some extent, climatic fluctuations were modulated by orbital eccentricity, but they were also very strongly influenced by atmospheric and oceanic circulation (Tyson and Partridge, 2002). When the earth is closest to the sun (perihelion) during austral summer, as it is at present, the temperature gradient between the equator and South Pole is strengthened, the southern hemisphere ITCZ is strengthened and tropical forcing of summer southern Africa climates is enhanced (Figure 1.9) (Tyson and Partridge, 2002). At these times, wetter climates should exist. Drier climates should occur when the earth is furthest from the sun (aphelion) during austral summer. This weakens the temperature gradient between the equator and the South Pole, as well as the ITCZ, and tropical forcing of southern Africa will be diminished. These changes should be 180˚ out-of-phase north and south of the equator (Tyson and Partridge, 2002; deMenocal, 1995).

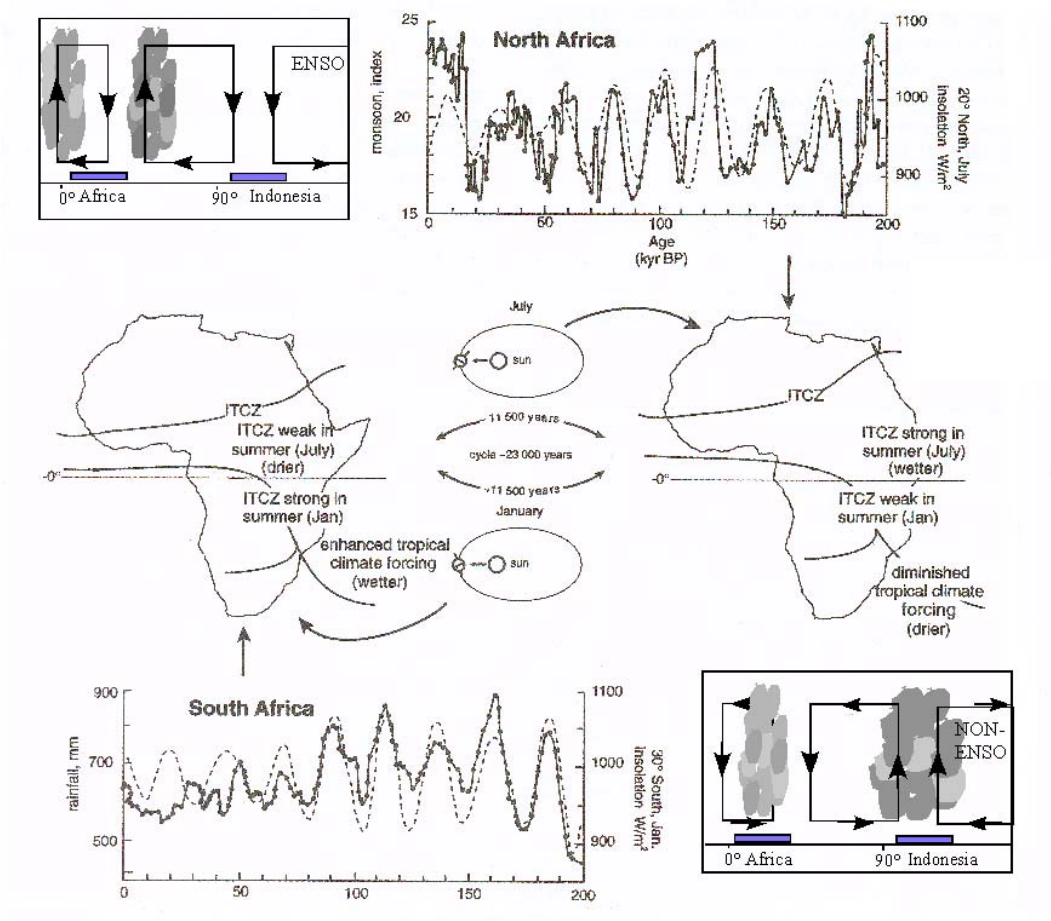

FIGURE 1.9: Forcing of climatic change over Africa in response to the 23-ky cycle of orbital precession. (modified from Partridge et al., 1997)

The paleoclimate record available in Partridge et al. (1997) is from the rainfall record found in the Pretoria Saltpan (Figure 1.10), one of the few suitably long continental paleoclimate records from Southern Africa. It shows that South African summer rainfall covaried with changes in southern hemisphere summer insolation with a 23,000-year periodicity, resulting from orbital precession. The lithologic data and the soil texture-precipitation regression were combined in order to produce the desired continuous late Pleistocene proxy record for South African rainfall variations and the corrected and calibrated ages from ^{14}C-dating suggest an average sedimentation rate of 37cm/ky. The resulting extrapolated age for the onset of lacustrine

sedimentation is roughly 195 ky (Partridge et al., 1997). This age and that of the fission-track data are consistent, however the age of the Saltpan is limited to 200 ky.

Initially the rainfall time series was calibrated using radiocarbon dates and the 200 ky age for the onset of lacustrine sedimentation. This resulted in a rainfall series characterized by very well defined, periodic (23,000 year) variations. The concurrent development of cooler and drier glacial conditions in North Africa and South Africa has been attributed to the coeval expansion of both northern and southern hemisphere polar ice sheets and upon tuning to southern hemisphere solar insolation at 30˚S the 23,000 year variations remained evident in the record (Partridge et al., 1997). This indicates that variations in the southern hemisphere record are 180˚ out-of-phase with respect to the northern hemisphere records, since both the northern and southern hemispheres respond to changes in summer season insolation resulting from orbital precession (Partridge et al., 1997).

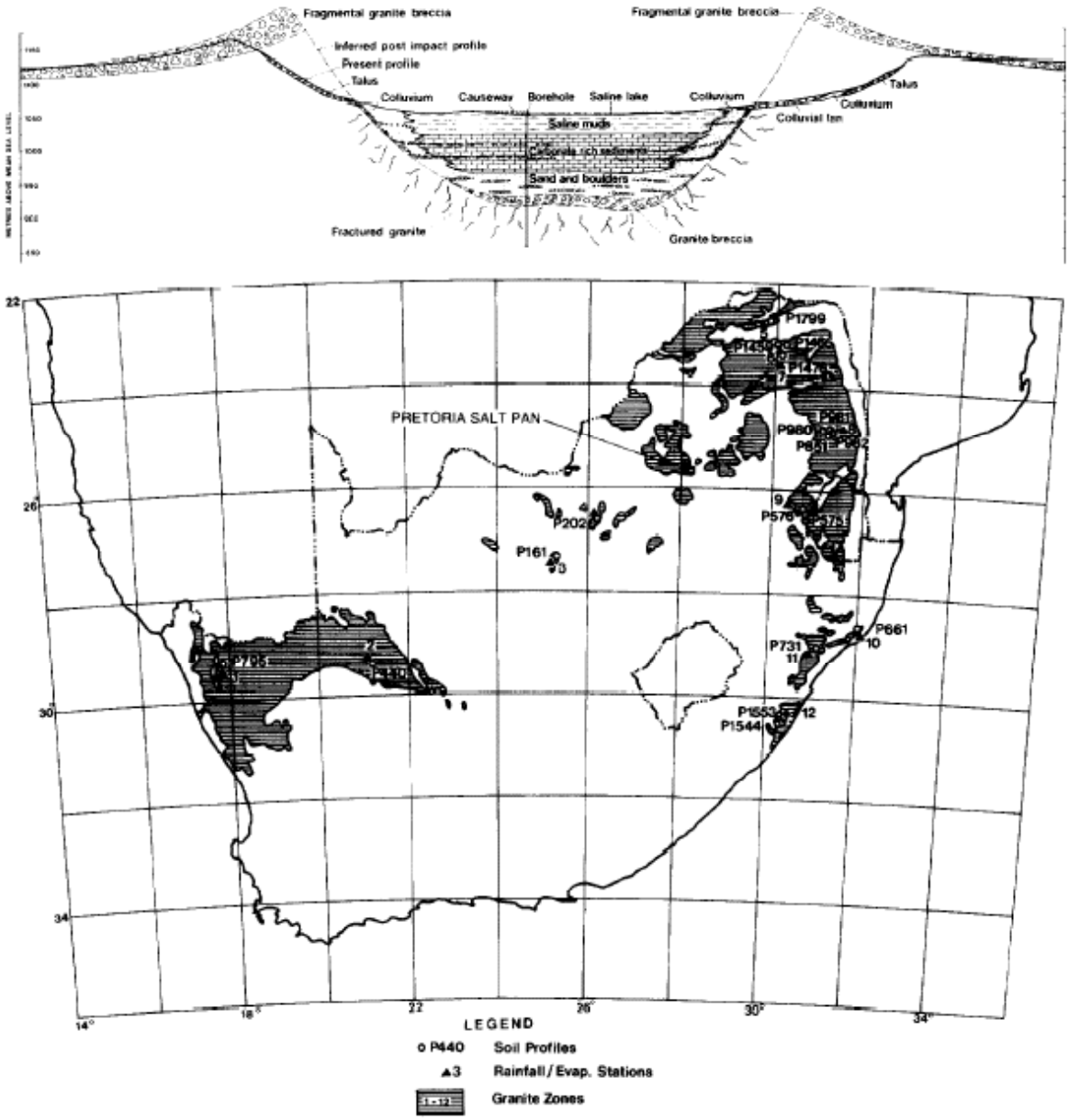

FIGURE 1.10: Location and schematic cross-section of the Pretoria Saltpan (from Partridge et al., 1997).

A high-resolution and near continuous record is available from Makapansgat Valley, documenting climate change in southern Africa from the latest glacial period through the Holocene (Figure 1.11) (Holmgren et al., 2003). The record is not as secure for the latest Pleistocene due to a hiatus in the speleothem record between 12.7 and 10.2 ky. The record

generated from nearby pollen and ground water isotope data, however, aids in constraining the dates on the stalagmites (Holmgren et al., 2003). Mean temperatures for both the Holocene and the Pleistocene have been calculated for this study area with a mean difference of about 5.7˚C. This detailed record allows for interpretations to be made of climatic change and variability in the summer rainfall region of South Africa and it is a more complete record than has been previously published (Holmgren et al., 2003), however the study area is still more likely than the marine sediments to be affected by some local phenomenon or other atmospheric changes.

FIGURE 1.11: Location of Makapansgat Valley (from Holmgren et al., 2003).

1.7.3 Northern and Eastern African Climate Studies

In Northern Africa, deMenocal (1995) shows that precipitation in subtropical, northern Africa is dominated by the West African monsoon, which is highly seasonal and follows an

annual cycle. There is evidence that the intensity of the African monsoon has been regulated by 23- to 19-ky variations in low-latitude insolation due to orbital precession and after the glacial climate extremes, which increased dramatically after 1 My, the dominant period of variation shifted from the 19- and 23-ky cycles to a 100-ky cycle (deMenocal, 1995). Because of these changes in climate and periodicities, the variations in subtropical African aridity can be seen in the variable quantities of eolian dust preserved in the marine sediments.

The study area examined by Russell et al. (2003), is found at Lake Edward (0˚N, 30˚E), an equatorial rift lake in central Africa found in the East African rift valley (Figure 1.12). High-resolution analyses of the chemical and stable isotopic composition (C and O) of the endogenic calcite show large oscillations in African climate over the past 5,400 years (Russell et al., 2003). Moisture balance is also seen in the oscillations and it is possible to see a series of droughts that ultimately define a drought period of roughly 725 years, possibly correlated with variations in the Indian Ocean monsoons. The similarities between the periodicities of Lake Edward and the Indian Ocean may indicate that the low-frequency variability dominates the millennial scale African moisture balance and Holocene climate of the Indian Ocean (Russell et al., 2003). The $\delta^{18}O_{calcite,}$ which is a function of the isotopic composition of the water in which the calcite forms, is expected to rise as the ratio of precipitation to evaporation of a lake decreases. This record shows submillennial variability on top of a long-term trend and these trends are in agreement with the late Holocene lake level history of Lake Edward (Russell et al., 2003).

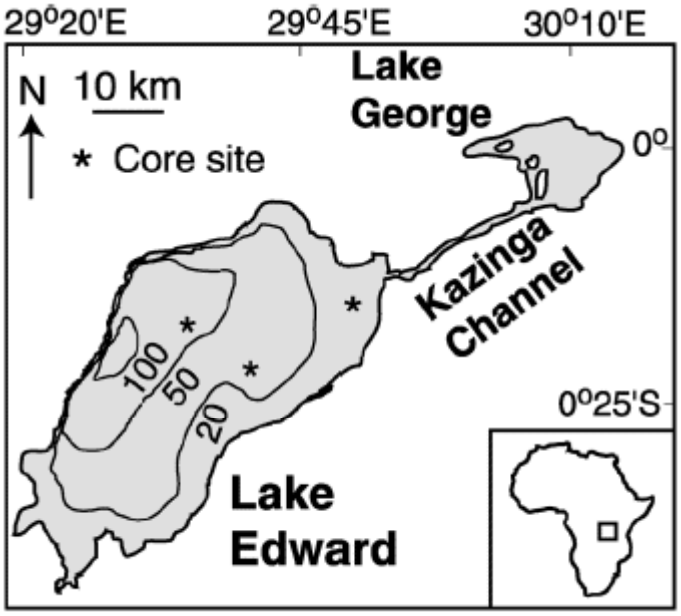

FIGURE 1.12: Location and bathymetry from Lake Edward (from Russell et al., 2003).

CHAPTER 2: METHODS

One hundred twenty five Pleistocene sediment samples were collected from the core at Site 1085B from ODP Leg 175 at 2-cm intervals, from the top 7.2 m of the recovered core. Table 2.1 provides a list of samples, as well as depth in cm bsf and age in ky. Color reflectance data were collected aboard ship (Wefer et al., 1997).

2.0 Sample Preparation

Samples were analyzed for weight percent sand, biogenic sediment geochemistry, terrigenous grain-size, and clay mineralogy. Aliquots (~0.5 to 1g) of each sample were taken after drying and ground using an agate mortar and pestal for use in biogenic sediment geochemical (C/N, %TOC, and %$CaCO_3$) analyses. C/N analyses were completed using a CHN analyzer while %TOC and %$CaCO_3$ analyses were completed using an ICP-AES at the University of South Carolina. Remaining analyses were preformed at Georgia State University.

TABLE 2.1 Identification, depth below seafloor and age for the analyzed samples

Sample	Depth (cm bsf)	Age (ky)	Sample	Depth (cm bsf)	Age (ky)	Sample	Depth (cm bsf)	Age (ky)	Sample	Depth (cm bsf)	Sample	Depth (cm bsf)
1-H 1-W 0-2	1	0.0	1-H 2-W 0-2	151	26.7	1-H 3-W 0-2	301	115.1	1-H 4-W 0-2	451	1-H 5-W 0-2	601
1-H 1-W 6-8	7	2.0	1-H 2-W 6-8	157	29.0	1-H 3-W 6-8	307	116.0	1-H 4-W 6-8	457	1-H 5-W 6-8	607
1-H 1-W 12-14	13	4.0	1-H 2-W 12-14	163	31.3	1-H 3-W 11-13	312	116.9	1-H 4-W 14-16	465	1-H 5-W 14-16	615
1-H 1-W 18-20	19	6.0	1-H 2-W 18-20	169	33.7	1-H 3-W 18-20	319	117.7	1-H 4-W 18-20	469	1-H 5-W 18-20	619
1-H 1-W 24-26	25	8.0	1-H 2-W 24-26	175	36.0	1-H 3-W 24-26	325	118.6	1-H 4-W 24-26	475	1-H 5-W 24-26	625
1-H 1-W 30-32	31	9.0	1-H 2-W 30-32	181	42.7	1-H 3-W 30-32	331	119.4	1-H 4-W 30-32	481	1-H 5-W 30-32	631
1-H 1-W 36-38	37	10.0	1-H 2-W 36-38	187	49.3	1-H 3-W 36-38	337	120.3	1-H 4-W 36-38	487	1-H 5-W 36-38	637
1-H 1-W 42-44	43	11.0	1-H 2-W 42-44	193	56.0	1-H 3-W 40-42	341	121.1	1-H 4-W 44-46	495	1-H 5-W 40-42	641
1-H 1-W 48-50	49	12.0	1-H 2-W 48-50	199	64.0	1-H 3-W 48-50	349	122.0	1-H 4-W 48-50	499	1-H 5-W 48-50	649
1-H 1-W 54-56	55	12.4	1-H 2-W 54-56	205	67.2	1-H 3-W 54-56	355	122.9	1-H 4-W 54-56	505	1-H 5-W 54-56	655
1-H 1-W 60-62	61	12.8	1-H 2-W 61-63	212	70.9	1-H 3-W 60-62	361		1-H 4-W 60-62	511	1-H 5-W 60-62	661
1-H 1-W 66-68	67	13.2	1-H 2-W 66-68	217	73.9	1-H 3-W 65-67	366		1-H 4-W 66-68	517	1-H 5-W 66-68	667
1-H 1-W 72-74	73	13.6	1-H 2-W 72-74	223	76.8	1-H 3-W 70-72	371		1-H 4-W 74-76	525	1-H 5-W 70-72	671
1-H 1-W 78-80	79	14.0	1-H 2-W 78-80	229	80.0	1-H 3-W 78-80	379		1-H 4-W 78-80	529	1-H 5-W 78-80	679
1-H 1-W 84-86	85	14.4	1-H 2-W 84-86	235	88.0	1-H 3-W 84-86	385		1-H 4-W 84-86	535	1-H 5-W 84-86	685
1-H 1-W 90-92	91	14.8	1-H 2-W 90-92	241	92.0	1-H 3-W 90-92	391		1-H 4-W 90-92	541	1-H 5-W 90-92	691
1-H 1-W 96-98	97	15.2	1-H 2-W 96-98	247	96.0	1-H 3-W 96-98	397		1-H 4-W 96-98	547	1-H 5-W 96-98	697
1-H 1-W 102-104	103	15.6	1-H 2-W 102-104	253	100.0	1-H 3-W 104-106	405		1-H 4-W 100-102	551	1-H 5-W 100-102	701
1-H 1-W 108-110	109	16.0	1-H 2-W 108-110	259	105.0	1-H 3-W 108-110	409		1-H 4-W 108-110	559	1-H 5-W 108-110	709
1-H 1-W 114-116	115	17.2	1-H 2-W 114-116	265	110.0	1-H 3-W 114-116	415		1-H 4-W 114-116	565	1-H 5-W 114-116	715
1-H 1-W 120-122	121	18.4	1-H 2-W 120-122	271	110.9	1-H 3-W 120-122	421		1-H 4-W 120-122	571	1-H 5-W 120-122	721
1-H 1-W 126-128	127	19.6	1-H 2-W 126-128	277	111.7	1-H 3-W 126-128	427		1-H 4-W 126-128	577	1-H 5-W 126-128	727
1-H 1-W 132-134	133	20.8	1-H 2-W 132-134	283	112.6	1-H 3-W 134-136	435		1-H 4-W 130-132	581	1-H 5-W 130-132	731
1-H 1-W 138-140	139	22.0	1-H 2-W 138-140	289	113.4	1-H 3-W 138-140	439		1-H 4-W 138-140	589	1-H 5-W 138-140	739
1-H 1-W 144-146	145	24.3	1-H 2-W 144-146	295	114.3	1-H 3-W 144-146	445		1-H 4-W 144-146	595	1-H 5-W 144-146	745

2.0.1 Coarse-grained Fraction Determination

Samples were dried over night in a 60ºC oven. An aliquot was removed and the remaining sample was then weighed, rehydrated and washed through a <63μm sieve using deionized water. The fine-grained fraction was collected for clay and grain-size analysis. The coarse-grained fraction remained in the sieve was dried at 60ºC over night and stored for foraminiferal analysis. The weight percent of the coarse-grained fraction was determined as follows:

$$[(Mass_{coarse}) / Mass_{total\ sample}] \times 100 \qquad [1]$$

The weight percent of the coarse-grained fraction is referred to as "weight percent sand," and, based on microscopic analysis of the sample, is composed of foraminiferal tests.

2.0.2 Fine-grained Fraction Determination

Two aliquots were taken from each fine-grained fraction: 1) 20 mL to find the mass of the fine-grained fraction and 2) 200 mL for grain-size analysis. These aliquots were taken after agitation of the 1000 mL graduated cylinder and timed settling. The 20 mL aliquot, for mass determination, was taken from a depth of 20 cm in the cylinder, 20 seconds after agitation was completed. This aliquot was then placed in a 60˚C oven and allowed to completely dehydrate. The weight percent of the fine-grained fraction was determined as follows:

$$[(Mass_{20mL\ aliquot} \times 50) / Mass_{total\ sample}] \times 100 \qquad [2]$$

Twenty mL of deionized water was added to bring the volume in the graduated cylinder back up to 1000 mL. Ten seconds after agitation and again, at a depth of 20 cm in the cylinder, four

successive 50 mL aliquots were taken for a total aliquot of 200 mL. This aliquot was centrifuged until the supernatant liquid was clear, decanted, and then processed further to remove carbonates and organics.

2.1 Grain-size Analysis

The removal of carbonates and organics was accomplished following the methods described by Jackson (1979). Carbonates were removed by the addition of 50 mL of 1N sodium acetate-acetic acid (NaOAc) buffer (pH 4.5) to each sample and placing it in a 70ºC water bath for 30 minutes. Following the water bath, samples were centrifuged until the supernatant liquid was clear and decanted. Samples were washed twice more with the NaOAc buffer, and twice with deionized water. Following each washing, samples were centrifuged and decanted. Organics were removed using 30% H_2O_2. Each sample was subjected to a total of 30 mL 30% H_2O_2, added 5 mL at a time, over the course of 3 hours while in a 50ºC water bath. Again, samples were centrifuged until the supernatant liquid was clear, decanted, and washed twice with deionized water. The grain-size aliquots were then ready for processing.

The Micromeritics Sedigraph 5100 uses Stoke's Law (see Equation 3) to determine sedimentation rate and particle size. The instrument is composed of particle size analyzers and a PC compatible computer system. The analyzer includes a variable speed stirrer to keep particles in suspension prior to analysis, a fixed X-ray source and detector, a cell movement assembly, an external mixing chamber, an external sedimentation liquid container, an external waste container, and a de-aeration chamber to remove air bubbles.

Sedimentation rate, as described by Stoke's Law, is used by the Sedigraph 5100 to determine particle size. It is measured using low energy X-ray beams passed through the transparent sample cell containing the sample solution to a detector. Only a portion of the X-

rays generated reach the detector owing to the absorption of a percentage of the X-rays by the grains within the solution. The dispersal of particle mass throughout the cell affects the number of X-ray pulses that reach the detector and these are the raw data used to derive the particle size distribution and median grain-size of each sample (Micromeritics, 2002). A baseline was run at the beginning of each day of grain-size analysis in order provide a measure of reproducibility.

2.2 Clay Mineralogical Determination

The fine-grained fraction (<63 μm) remaining in the 1000 mL cylinder was flocculated over the course of two days using $CaCl_2$ as the flocculant. Fifty mL 1M $CaCl_2$ was added to each cylinder twice, for a total of 100 mL 1M $CaCl_2$ added to each sample. Once flocculation was complete, the liquid was decanted and the remaining sediment was prepared for clay mineralogical analysis. The same procedures for removal of carbonates and organics were followed for the clay aliquots as had been previously used on the grain-size aliquots.

Forty samples from the upper three meters of the core were selected for clay mineralogical analysis and were resuspended using 2% Na-hexametaphosphate. The <2 μm fraction was separated from the larger grain-sizes using centrifuge sedimentation (Jackson, 1979). The time for sedimentation using a centrifuge was determined using Stoke's Law:

$$T = [63x108 \bullet \eta \bullet \log_{10}(R/S)] / [N^2 \bullet D^2 \bullet \Delta s] \qquad [3]$$

Where time (T, in minutes) for particles of a given size depends on the viscosity (η) of the settling fluid, which further depends on the fluid's temperature. R is the radius of rotation at the top of the sediment in the centrifuge bottle (cm). S is the radius of rotation of the suspension surface in the centrifuge bottle (cm). N is the rotational velocity (rpm) of the centrifuge. D is

the particle diameter and Δs is the difference in specific gravity between the particle and water (Jackson, 1979).

After the <2 μm fraction was separated off, further digestion of calcite was required. The samples were placed on a 60ºC hotplate and 100 mL of 10% acetic acid was added. The samples were allowed to digest over night for roughly six to eight hours. Samples were centrifuged until the supernatant liquid was clear and decanted. Each sample was then washed in deionized water and centrifuged to <50 mL. Using a transfer pipette, part of the clay fraction was dropped onto a glass petrographic slide and allowed to dry in air. This preparation resulted in an oriented mount in which the c-axis of the phyllosilicate crystals was perpendicular to the slide surface (Moore and Reynolds, 1996). Two slides were made for each sample; one was left and analyzed in the air-dried condition and the second was solvated in an ethylene glycol tank for 24 hours prior to analysis. Following analysis, glycol-solvated slides were heated to 550ºC for one hour and re-analyzed, resulting in three separate analyses for each of the 40 clay samples selected for mineralogical identification.

2.2.1 X-Ray Diffraction

Clay mineralogy was determined using X-ray diffraction, following Moore and Reynolds (1996). The oriented mounts were analyzed on a Philips Model 12045 X-Ray Diffractometer with MDI Data Box® from 2-32° 2θ, at a scanning speed of 1° 2θ/minute with counts taken over 0.02° 2θ intervals, using Cu-Kα radiation of wavelength (λ) 1.54 angstroms (Å), filtered through a graphite monochrometer.

X-ray diffraction can occur only when Bragg's Law is satisfied:

$$n\lambda = 2d\sin\theta \qquad [4]$$

Where n is an integral number of wavelengths (λ) of the diffracted X-ray, d is the spacing between layers of atoms within the crystal lattice, and θ is the angle between the incident X-ray beam and the plane of atoms. When Bragg's Law is satisfied, diffraction (coherent constructive scattering) results in a peak, which is detected using a scintillation counter and filtered using a graphite monochrometer. The d-spacing (Å) is determined using Bragg's Law [4] from the angle at which peaks occur and corresponds to a Miller Index.

For each sample, diffraction peaks from the air-dried, ethylene glycol solvated, and 550ºC heated oriented mounts were identified and measured in order to determine clay mineralogy. The data patterns for each sample can be found the Appendix. A quartz standard was run at the beginning of each day of XRD analysis in order ensure proper alignment of the goniometer and provide a measure of reproducibility. Stacked data patterns for the quartz standards are also provided in the Appendix.

2.2.2 Clay Mineralogical Analysis

Analysis of clay mineralogy was performed using the MacDiff 4.2.5 computer program (Petschick, 2000). MacDiff is a program for the analysis and display of X-ray diffractograms on Apple Macintosh platforms designed to complement XRD applications distributed by Philips. It is not limited to analysis of clay mineral diffractograms. Standard single-scan formats (ASCII, MDI) are identified automatically and data and plots can be exported to other programs (MS Excel) for tabulation and further analysis (Petschick, 2000).

Following XRD analysis of the clay fraction, the *.MDI files were exported as *.ASCII files. It is important to put the data in the proper order (angle, counts, d-spacing in columns 1, 2, and 3, respectively) prior to opening up and converting to *.TEXT files. This allows MacDiff to

calculate a baseline. Upon selecting the folder where the data is stored, MacDiff converts the files to *.TEXT files and overwrites the folder with the converted files. The following options were selected prior to conversion to *.TEXT: single peak correction (Quartz, d = 3.343Å), find base, anode (Cu, 1.54 Å), smooth (MacDiff 21 steps). Other options are available depending on the anode used and the type of analysis desired.

Two analysis programs were set up to determine the peak area of each of the following peaks: air-dried smectite (001), illite (001, 002, 003), kaolinite (001), quartz (101) and ethylene glycol solvated smectite (001) and illite (001, 003) (Table 2.2). Also determined were the full width – half maximum (FWHM), peak intensity and relative area percentages of the phyllosilicates. Once analysis following the established programs was completed, each peak was recorded and the data was saved to a separate report file.

TABLE 2.2 MacDiff Analysis Programs (Petschick, 2000)**.**

Analysis Program	Mineral	d-spacing (A)	Range	Peak Analysis	Relative %	Desired Analysis	Formula
1	Smectite (001)	14.4	1.5	Center	Yes	Area	#1:2#
	Illite (001)	10	0.3	Center	Yes	Area	#2:2#
	Illite (002)	5	0.3	Center	Yes	Area	#3:2#
	Illite (003)	3.3	0.3	Center	Yes	Area	#4:2#
	Kaolinite (001)	7.5	0.5	Center	Yes	Area	#5:2#
	Quartz (101)	3.3	0.1	Center	Yes	Area	#6:2#
2	Smectite $(001)_{glycol}$	17	1.5	Center	Yes	Area	#1:2#
	Illite $(001)_{glycol}$	10	0.3	Center	Yes	Area	#2:2#
	Illite $(003)_{glycol}$	3.3	0.3	Center	Yes	Area	#3:2#

Crystallinity values were determined for smectite and illite by calculating the IB (integral breadth) of the 17Å-smectite and 10Å-illite peaks following solvation in ethylene glycol (Petschick et al., 1996). The IB is the width (in $\Delta^{o}2\theta$) of the rectangle of the same height and

area as the measured peak and is more sensitive for peak tail variations than FWHM (full width at half maximum) calculations of crystallinity (Petschick et al., 1996; Petschick, 2000). It is calculated as follows:

$$(A)(0.02) / (I) \quad [5]$$

Where A is the area of the rectangle of the same height as the peak, 0.02 (μm) is the scan step size used during X-ray diffraction and I is the intensity of the peak. The illite intensity ratio was also calculated by taking a ratio of the intensity of the 5Å (002) peak to the 10Å (001) peak. This illite intensity ratio differs from the (003)/(001) ratio used by Moore and Reynolds (1996). The (002)/(001) ratio is used in order to have comparable data to Petschick et al., (1996).

2.3 Biogenic Sediment Geochemistry

The analysis of biogenic sediment geochemistry (C/N, %TOC, $\%CaCO_3$) was performed at the University of South Carolina. Between 5 – 10 mg of dried ground material was analyzed on a Perkin Elmer 2400 Elemental Analyzer to measure total nitrogen (TN) and total carbon (TC). A similar amount of material was used for analysis of inorganic carbon (TI). Inorganic carbon was determined on a JY Horiba Ultima-C ICP-AES. The calcium concentrations were used to determine $\%CaCO_3$. Total organic carbon (TOC) was determined by the difference:

$$TC – TI = TOC \quad [6]$$

Where TC is the measured total carbon, TI is the measured inorganic carbon and TOC is total organic carbon. C/N ratios are determined by:

$$TOC / TN = C/N \quad [7]$$

2.4 Age Model and MAR

The age model is based on the oxygen isotope curve developed by Foote (2005) and tuned to SPECMAP by Christensen. The SPECMAP Oxygen Isotope Curve is a stacked record of the $\delta^{18}O$ from benthic foraminifera and is a measure of changes in sea-ice volume (Imbrie et al., 1984). The age model is constrained by the *Emiliani huxleyi* acme datum found at 529 cm bsf (Wefer et al., 1998). The acme datum has been dated to 90 ky and provides a biostratigraphic point for correlation with the SPECMAP Oxygen Isotope Curve (Imbrie et al., 1984). The first occurrence of *E. huxleyi* at 260 ky also provides a constraint on the age of these samples.

The mass accumulation rate (MAR) ($g/cm^2/ky$) is calculated to take away the dilution factor using the following equation:

$$MAR = BAR \times Proxy\ Percentage \qquad [8]$$

Where BAR is the bulk accumulation rate provided by Christensen, determined by the sedimentation rate, and Proxy Percentage is the concentration percentage of the proxy being analyzed.

CHAPTER 3: RESULTS

3.0 Age Model

The age model is constrained by the biostratigraphy of the whole core, taken aboard ODP Leg 175 (Wefer et al., 1998), and $\delta^{18}O$ values of *Globigerina bulloides*. The acme datum of the calcareous nannofossil, *Emiliani huxleyi*, is at 529 cm bsf at Site 1085B and dates to 90 ky. Table 3.1 provides $\delta^{18}O$ values for *G. bulloides*, the sample and depth at which the foraminifera were found and their corresponding age. Upon correlation with SPECMAP (Imbrie et al., 1984), boundaries between Marine Isotope Stages (MIS) 1 through 5 were tentatively determined for the upper 355 cm bsf constrained by *G. bulloides*.

TABLE 3.1 **Age model for the upper 355 cm bsf of the core analyzed.** $\delta^{18}O$ values are from analysis of the planktonic foraminifera *Globigerina bulloides* and are provided by Christensen. Interglacial (IG) stages are identified in yellow (MIS 1, 3, 5) and glacial (G) stages are identified in blue (MIS 2, 4).

	Sample	Depth (cm bsf)	Age (ky)	$\delta^{18}O$
MIS 1	1-H 1-W 0-2	1	0.0	0.65
	1-H 1-W 6-8	7	2.0	-0.25
	1-H 1-W 12-14	13	4.0	-0.04
	1-H 1-W 18-20	19	6.0	
	1-H 1-W 24-26	25	8.0	0.76
	1-H 1-W 30-32	31	9.0	
	1-H 1-W 36-38	37	10.0	0.98
	1-H 1-W 42-44	43	11.0	0.90
MIS 2	1-H 1-W 48-50	49	12.0	1.30
	1-H 1-W 54-56	55	12.4	0.47
	1-H 1-W 60-62	61	12.8	0.69
	1-H 1-W 66-68	67	13.2	
	1-H 1-W 72-74	73	13.6	0.81
	1-H 1-W 78-80	79	14.0	1.02
	1-H 1-W 84-86	85	14.4	1.24
	1-H 1-W 90-92	91	14.8	1.36
	1-H 1-W 96-98	97	15.2	
	1-H 1-W 102-104	103	15.6	1.49
	1-H 1-W 108-110	109	16.0	1.51
	1-H 1-W 114-116	115	17.2	1.52
	1-H 1-W 120-122	121	18.4	1.43
	1-H 1-W 126-128	127	19.6	1.24
	1-H 1-W 132-134	133	20.8	1.25
	1-H 1-W 138-140	139	22.0	1.84
	1-H 1-W 144-146	145	24.3	1.17

	Sample	Depth (cm bsf)	Age (ky)	$\delta^{18}O$
MIS 2	1-H 2-W 0-2	151	26.7	1.04
	1-H 2-W 6-8	157	29.0	
	1-H 2-W 12-14	163	31.3	0.88
	1-H 2-W 18-20	169	33.7	
	1-H 2-W 24-26	175	36.0	0.96
MIS 3	1-H 2-W 30-32	181	42.7	0.84
	1-H 2-W 36-38	187	49.3	
	1-H 2-W 42-44	193	56.0	0.67
MIS 4	1-H 2-W 48-50	199	64.0	1.49
	1-H 2-W 54-56	205	67.2	1.17
	1-H 2-W 61-63	212	70.9	1.06
	1-H 2-W 66-68	217	73.9	
	1-H 2-W 72-74	223	76.8	1.07
MIS 5	1-H 2-W 78-80	229	80.0	0.83
	1-H 2-W 84-86	235	88.0	0.86
	1-H 2-W 90-92	241	92.0	
	1-H 2-W 96-98	247	96.0	
	1-H 2-W 102-104	253	100.0	0.56
	1-H 2-W 108-110	259	105.0	
	1-H 2-W 114-116	265	110.0	0.59
	1-H 2-W 120-122	271	110.9	0.37
	1-H 2-W 126-128	277	111.7	
	1-H 2-W 132-134	283	112.6	
	1-H 2-W 138-140	289	113.4	0.19
	1-H 2-W 144-146	295	114.3	

	Sample	Depth (cm bsf)	Age (ky)	$\delta^{18}O$
MIS 5	1-H 3-W 0-2	301	115.1	
	1-H 3-W 6-8	307	116.0	
	1-H 3-W 11-13	312	116.9	
	1-H 3-W 18-20	319	117.7	
	1-H 3-W 24-26	325	118.6	
	1-H 3-W 30-32	331	119.4	
	1-H 3-W 36-38	337	120.3	
	1-H 3-W 40-42	341	121.1	
	1-H 3-W 48-50	349	122.0	-0.05
	1-H 3-W 54-56	355	122.9	-0.02

3.1 Clay Mineralogy

Forty samples were selected for clay mineralogical analysis ranging from 1 cm bsf through 295 cm bsf (Table 3.2). Stacked patterns are available in the Appendix. Relative percentages of kaolinite, smectite and illite are plotted against depth (cm bsf) and age (ky) in Figure 3.1. Kaolinite input ranges between 6.11% and 16.35% over the past 120 ky. Maximum kaolinite (16.35%) is found at 79 cm bsf, 14 ky in sample 1H1W 78-80. Minimum kaolinite input (6.11%) occurred 265 cm bsf, 110 ky in sample 1H2W 114-116. Smectite input has a range of 3.37% to 32.51% over the past 120 ky. The maximum smectite input (32.51%) is found at 7 cm bsf, 2 ky in sample 1H1W 6-8 while the minimum input (3.37%) is found at 49 cm bsf, 12 ky in sample 1H1W 48-50. The input of illite ranges between 10.46% and 28.99% over the past 120 ky. The maximum illite input (28.99%) occurs at 49 cm bsf, 12 ky in sample 1H1W 48-50, the same sample as the smectite low. The minimum illite input (10.46%) is found at 181 cm bsf, 42.7 ky in sample 1H2W 30-32.

Smectite and illite crystallinity are plotted with depth (cm bsf) and age (ky) in Figure 3.2. Smectite has a crystallinity range between 0.15 (7 cm bsf, 2 ky, sample 1H1W 6-8) and 7.62 (13 cm bsf, 4 ky, sample 1H1W 12-14). Smectite crystallinity generally ranges between ~ 1.00 and 1.50, with a few values between 1.50 and 2.00 and only one point < 1.00 and one > 2.00. The range of illite crystallinity is between 0.50 (1 cm bsf, 0 ky, sample 1H1W 0-2) and 1.01 (25 cm bsf, 8 ky, sample 1H1W 24-26). There are greater amplitude oscillations of illite crystallinity in the first meter of sediment, corresponding to roughly the past 20 ky.

Illite d-spacing (Å) is plotted against depth (cm bsf) and age (ky) in Figure 3.3. The illite d-spacing values range from 10.01 Å in sample 1H1W 60-62 (61 cm bsf, 12.4 ky) to 10.258 Å in samples 1H2W 61-63, 84-86 (212 and 235 cm bsf, 70.9 and 88 ky, respectively). Below 150 cm bsf, the average d-spacing is 10.20 Å, while above 150 cm bsf, the average is 10.13 Å and has a wider range of variation. The illite intensity ratio is plotted against depth (cm bsf) and age (ky) in Figure 3.4 and is the ratio of the intensity of the 5 Å (002) illite peak to the 10 Å (001) illite peak. This intensity ratio ranges from 0.41 to 1.43 (25 cm bsf, 8 ky, sample 1H1W 24-26 and 157 cm bsf, 28.99 ky, sample 1H2W 6-8, respectively).

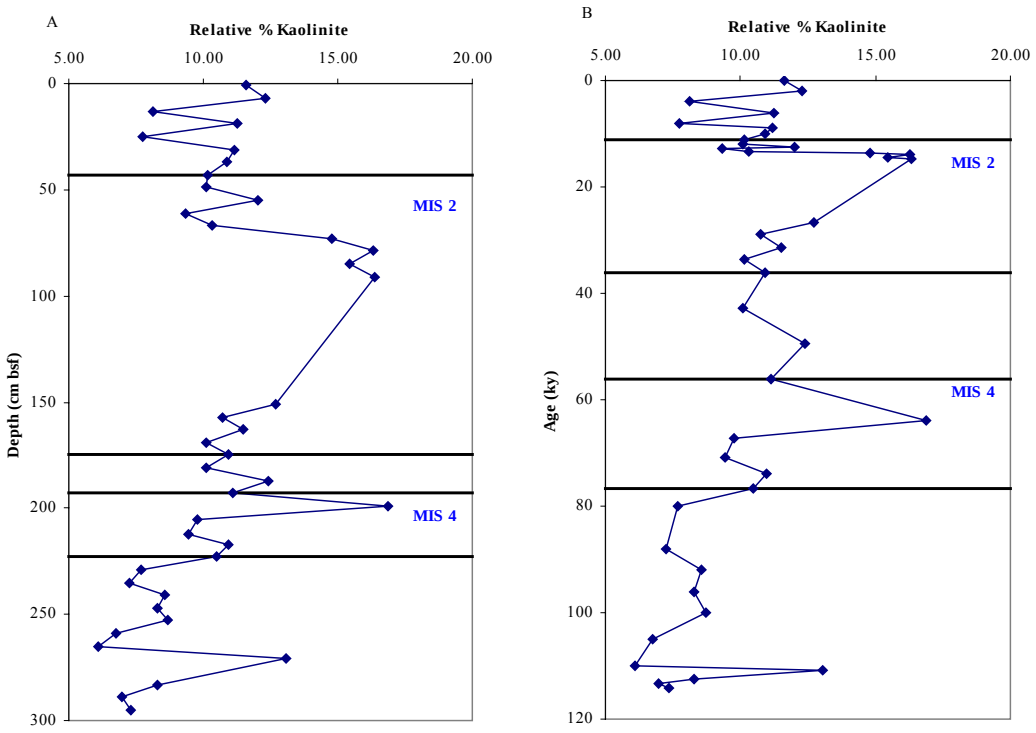

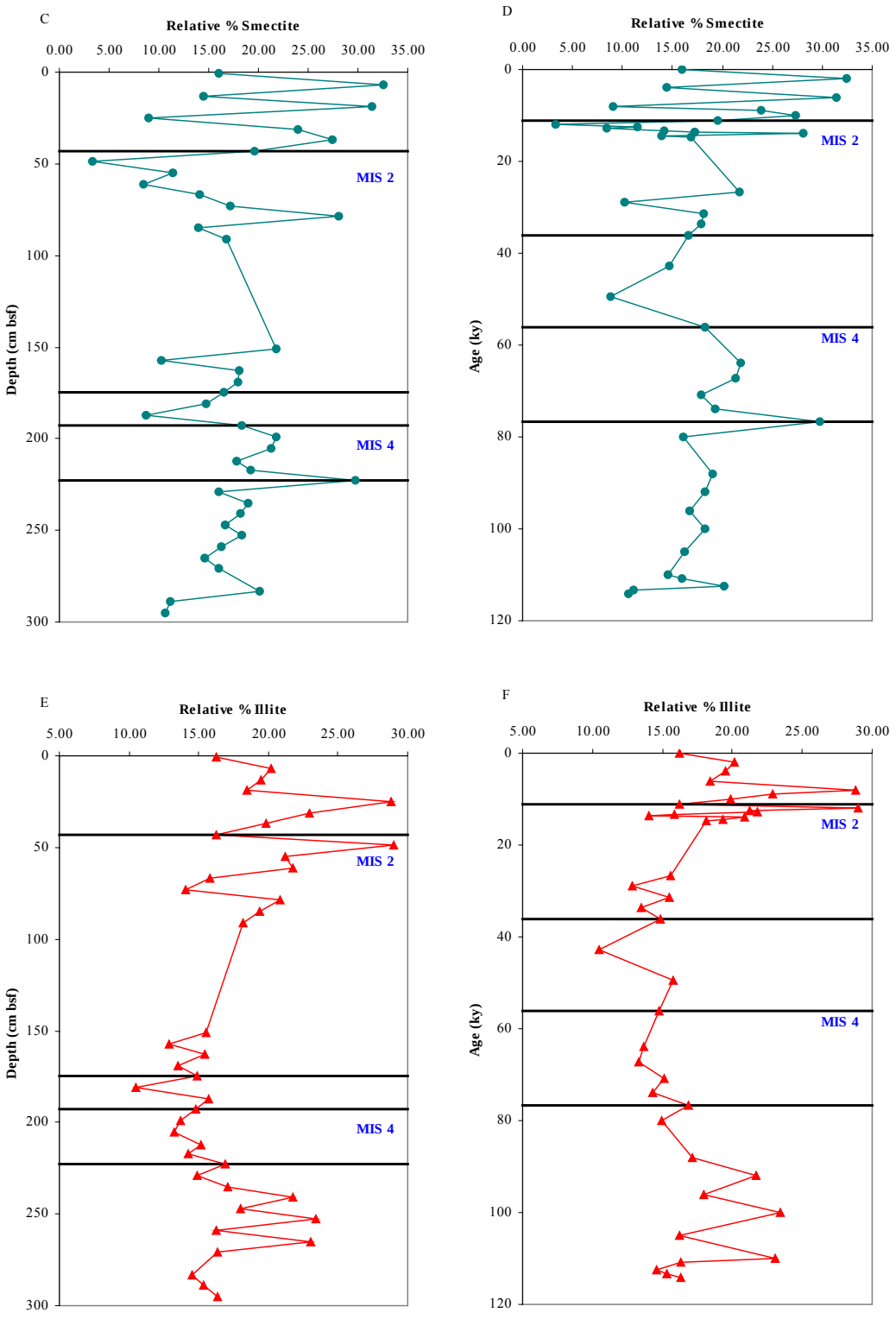

FIGURE 3.1: Relative percentages of kaolinite (A, B), smectite (C, D) and illite (E, F) plotted with depth (A, C, E) and age (B, D, F).

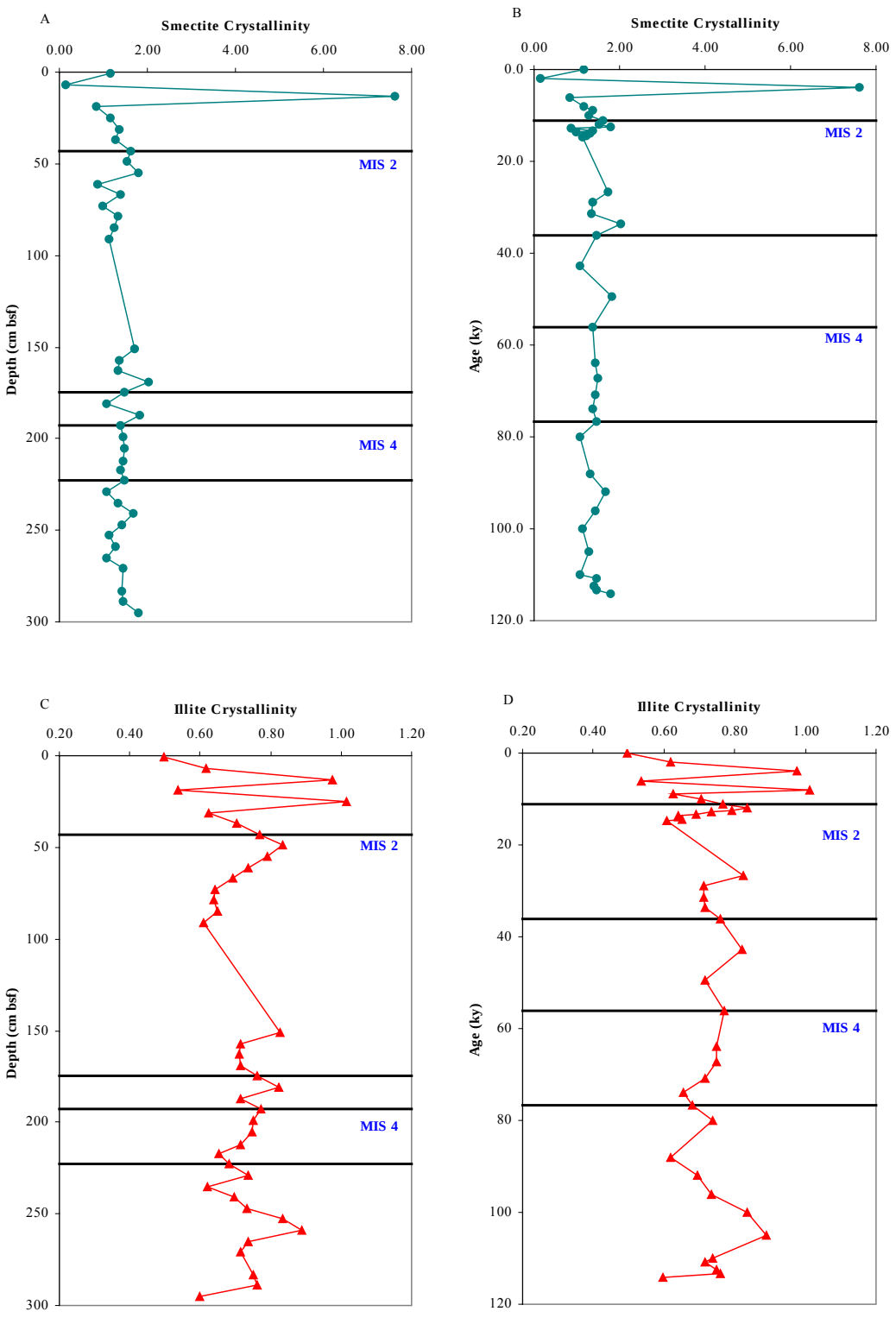

FIGURE 3.2: Smectite (A, B) and illite (C, D) crystallinity plotted with depth (A, C) and age (B, D).

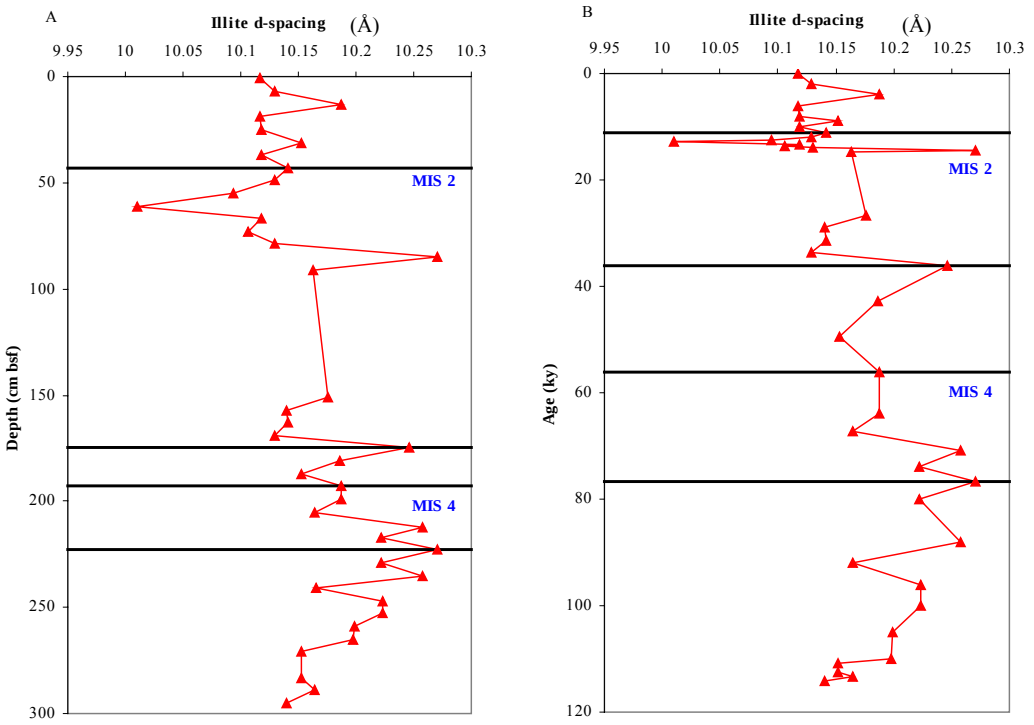

FIGURE 3.3: Illite d-spacing (Å) plotted with depth (A) and age (B).

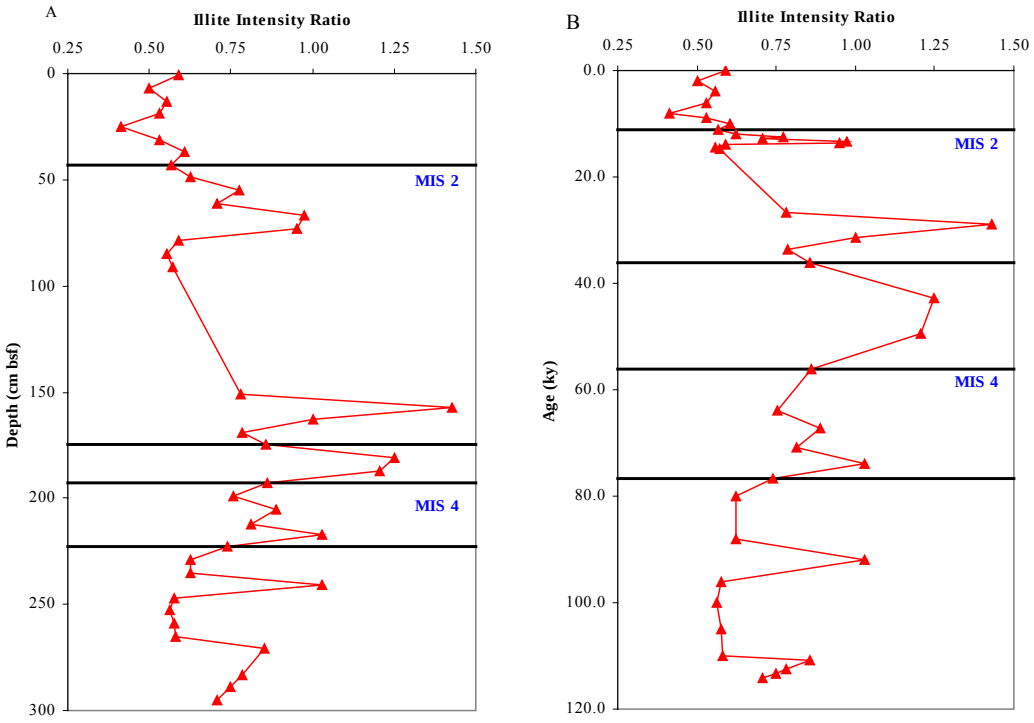

FIGURE 3.4: Illite intensity ratio (5Å/10Å) plotted with depth (A) and age (B).

TABLE 3.2 Clay data, depth and age for each clay sample analyzed.

Sample	Depth	Age	Bulk Clay	Relative Percentages				Ratios			Crystallinity		Illite	Illite
	(cm bsf)	(ky)	Minerals	Kaolinite	Smectite	Illite	Quartz	K/S	K/I	I/S	Smectite	Illite	d-spacing (A)	IR
1-H 1-W 0-2	1	0.0	kaolinite, smectite, illite	11.61	15.97	16.24	56.19	0.73	0.71	1.02	1.15	0.50	10.12	0.59
1-H 1-W 6-8	7	2.0	kaolinite, smectite, illite	12.31	32.51	20.17	35.01	0.38	0.61	0.62	0.15	0.62	10.13	0.50
1-H 1-W 12-14	13	4.0	kaolinite, smectite, illite	8.12	14.49	19.46	57.93	0.56	0.42	1.34	7.62	0.98	10.19	0.56
1-H 1-W 18-20	19	6.0	kaolinite, smectite, illite	11.24	31.44	18.43	38.89	0.36	0.61	0.59	0.85	0.54	10.12	0.53
1-H 1-W 24-26	25	8.0	kaolinite, smectite, illite	7.75	9.03	28.83	54.39	0.86	0.27	3.19	1.15	1.01	10.12	0.41
1-H 1-W 30-32	31	9.0	kaolinite, smectite, illite	11.18	23.92	22.91	41.99	0.47	0.49	0.96	1.38	0.62	10.15	0.53
1-H 1-W 36-38	37	10.0	kaolinite, smectite, illite	10.90	27.39	19.85	41.86	0.40	0.55	0.72	1.27	0.71	10.12	0.61
1-H 1-W 42-44	43	11.0	kaolinite, smectite, illite	10.15	19.61	16.25	53.99	0.52	0.62	0.83	1.62	0.77	10.14	0.57
1-H 1-W 48-50	49	12.0	kaolinite, smectite, illite	10.09	3.37	28.99	57.55	3.00	0.35	8.61	1.54	0.83	10.13	0.63
1-H 1-W 54-56	55	12.4	kaolinite, smectite, illite	12.03	11.45	21.23	55.29	1.05	0.57	1.85	1.79	0.79	10.09	0.77
1-H 1-W 60-62	61	12.8	kaolinite, smectite, illite	9.35	8.48	21.75	60.43	1.10	0.43	2.56	0.86	0.74	10.01	0.71
1-H 1-W 66-68	67	13.2	kaolinite, smectite, illite	10.32	14.14	15.81	59.72	0.73	0.65	1.12	1.39	0.69	10.12	0.98
1-H 1-W 72-74	73	13.6	kaolinite, smectite, illite	14.79	17.21	14.05	53.95	0.86	1.05	0.82	0.99	0.64	10.11	0.95
1-H 1-W 78-80	79	14.0	kaolinite, smectite, illite	16.30	28.08	20.88	34.73	0.58	0.78	0.74	1.32	0.64	10.13	0.59
1-H 1-W 84-86	85	14.4	kaolinite, smectite, illite	15.46	13.95	19.34	51.26	1.11	0.80	1.39	1.23	0.65	10.27	0.56
1-H 1-W 90-92	91	14.8	kaolinite, smectite, illite	16.35	16.81	18.17	48.66	0.97	0.90	1.08	1.13	0.61	10.16	0.57
1-H 2-W 0-2	151	26.7	kaolinite, smectite, illite	12.72	21.78	15.56	49.95	0.58	0.82	0.71	1.72	0.83	10.18	0.78
1-H 2-W 6-8	157	29.0	kaolinite, smectite, illite	10.74	10.25	12.86	66.15	1.05	0.83	1.26	1.37	0.71	10.14	1.43
1-H 2-W 12-14	163	31.3	kaolinite, smectite, illite	11.50	18.12	15.48	54.91	0.63	0.74	0.85	1.35	0.71	10.14	1.00
1-H 2-W 18-20	169	33.7	kaolinite, smectite, illite	10.12	17.90	13.52	58.46	0.57	0.75	0.76	2.02	0.72	10.13	0.79
1-H 2-W 24-26	175	36.0	kaolinite, smectite, illite	10.91	16.57	14.85	57.67	0.66	0.73	0.90	1.48	0.76	10.25	0.86
1-H 2-W 30-32	181	42.7	kaolinite, smectite, illite	10.10	14.71	10.46	64.73	0.69	0.97	0.71	1.08	0.82	10.19	1.25
1-H 2-W 36-38	187	49.3	kaolinite, smectite, illite	12.41	8.76	15.73	63.10	1.42	0.79	1.80	1.82	0.72	10.15	1.20
1-H 2-W 42-44	193	56.0	kaolinite, smectite, illite	11.12	18.32	14.79	55.77	0.61	0.75	0.81	1.38	0.77	10.19	0.86
1-H 2-W 48-50	199	64.0	kaolinite, smectite, illite	16.89	21.85	13.70	47.57	0.77	1.23	0.63	1.45	0.75	10.19	0.76
1-H 2-W 54-56	205	67.2	kaolinite, smectite, illite	9.78	21.34	13.28	55.60	0.46	0.74	0.62	1.49	0.75	10.16	0.89
1-H 2-W 61-63	212	70.9	kaolinite, smectite, illite	9.45	17.87	15.13	57.55	0.53	0.63	0.85	1.45	0.71	10.26	0.81
1-H 2-W 66-68	217	73.9	kaolinite, smectite, illite	10.96	19.26	14.27	55.51	0.57	0.77	0.74	1.38	0.65	10.22	1.03
1-H 2-W 72-74	223	76.8	kaolinite, smectite, illite	10.48	29.78	16.86	42.88	0.35	0.62	0.57	1.46	0.68	10.27	0.74
1-H 2-W 78-80	229	80.0	kaolinite, smectite, illite	7.69	16.05	14.92	61.34	0.48	0.52	0.93	1.06	0.74	10.22	0.63
1-H 2-W 84-86	235	88.0	kaolinite, smectite, illite	7.26	19.03	17.11	56.60	0.38	0.42	0.90	1.33	0.62	10.26	0.63
1-H 2-W 90-92	241	92.0	kaolinite, smectite, illite	8.56	18.26	21.73	51.45	0.47	0.39	1.19	1.68	0.70	10.17	1.03
1-H 2-W 96-98	247	96.0	kaolinite, smectite, illite	8.29	16.72	17.97	57.02	0.50	0.46	1.07	1.43	0.73	10.22	0.58
1-H 2-W 102-104	253	100.0	kaolinite, smectite, illite	8.70	18.29	23.40	49.60	0.48	0.37	1.28	1.13	0.84	10.22	0.56
1-H 2-W 108-110	259	105.0	kaolinite, smectite, illite	6.75	16.24	16.23	60.78	0.42	0.42	1.00	1.27	0.89	10.20	0.58
1-H 2-W 114-116	265	110.0	kaolinite, smectite, illite	6.11	14.58	23.08	56.23	0.42	0.26	1.58	1.08	0.74	10.20	0.58
1-H 2-W 120-122	271	110.9	kaolinite, smectite, illite	13.05	16.02	16.34	54.59	0.81	0.80	1.02	1.46	0.72	10.15	0.85
1-H 2-W 132-134	283	112.6	kaolinite, smectite, illite	8.29	20.14	14.55	57.02	0.41	0.57	0.72	1.41	0.75	10.15	0.78
1-H 2-W 138-140	289	113.4	kaolinite, smectite, illite	6.97	11.16	15.32	66.55	0.62	0.46	1.37	1.45	0.76	10.16	0.75
1-H 2-W 144-146	295	114.3	kaolinite, smectite, illite	7.33	10.59	16.35	65.73	0.69	0.45	1.54	1.79	0.60	10.14	0.71

3.2 Median Grain-size and Grain-size Distribution

Median grain-size ranges from 0.39 μm, at various depths, to a maximum of 13.25 μm at a depth of 271 cm bsf (1H2W 120-122), as seen in Figure 3.5. There is another substantial peak (12.4270 μm) at 91 cm bsf (1H1W 90-92), as well as two smaller amplitude peaks, 7.38 μm and 8.12 μm, found at 247 and 601 cm bsf, samples 1H2W 96-98 and 1H5W 0-2, respectively. Median grain-size data is available in Table 3.3.

Figure 3.6 provides the grain-size distribution downcore with depth (cm bsf) and age (ky). Above 100 cm bsf, the dominant grain-size distribution exhibits an eolian pattern with occasional single samples exhibiting a hemipelagic grain-size distribution, based on Rea and Hovan (1995). Between 100 cm bsf and 250 cm bsf the dominant grain-size distribution exhibits a hemipelagic distribution with only intermittent eolian signals. Below 300 cm bsf, the sediment grain-size distributions are characterized by hemipelagic signals. Figure 3.7 provides examples of typical eolian and hemipelagic sediment grain-size distributions. Classification of grain-size distribution for each sample is available in Table 3.4.

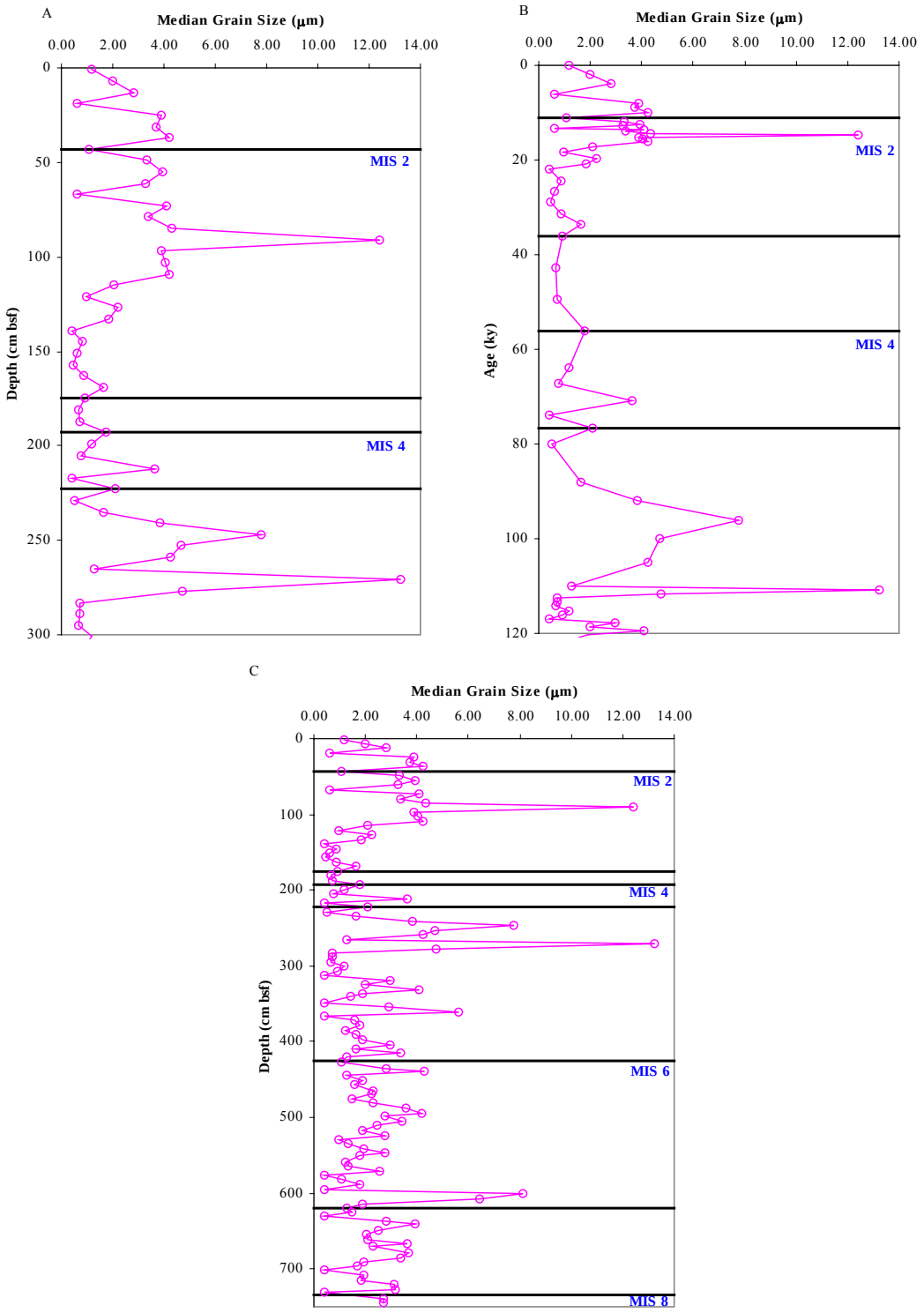

FIGURE 3.5: Median grain-size plotted against depth (A) and age (B) to the extent of the age model. Median grain-size plotted for all samples analyzed (C).

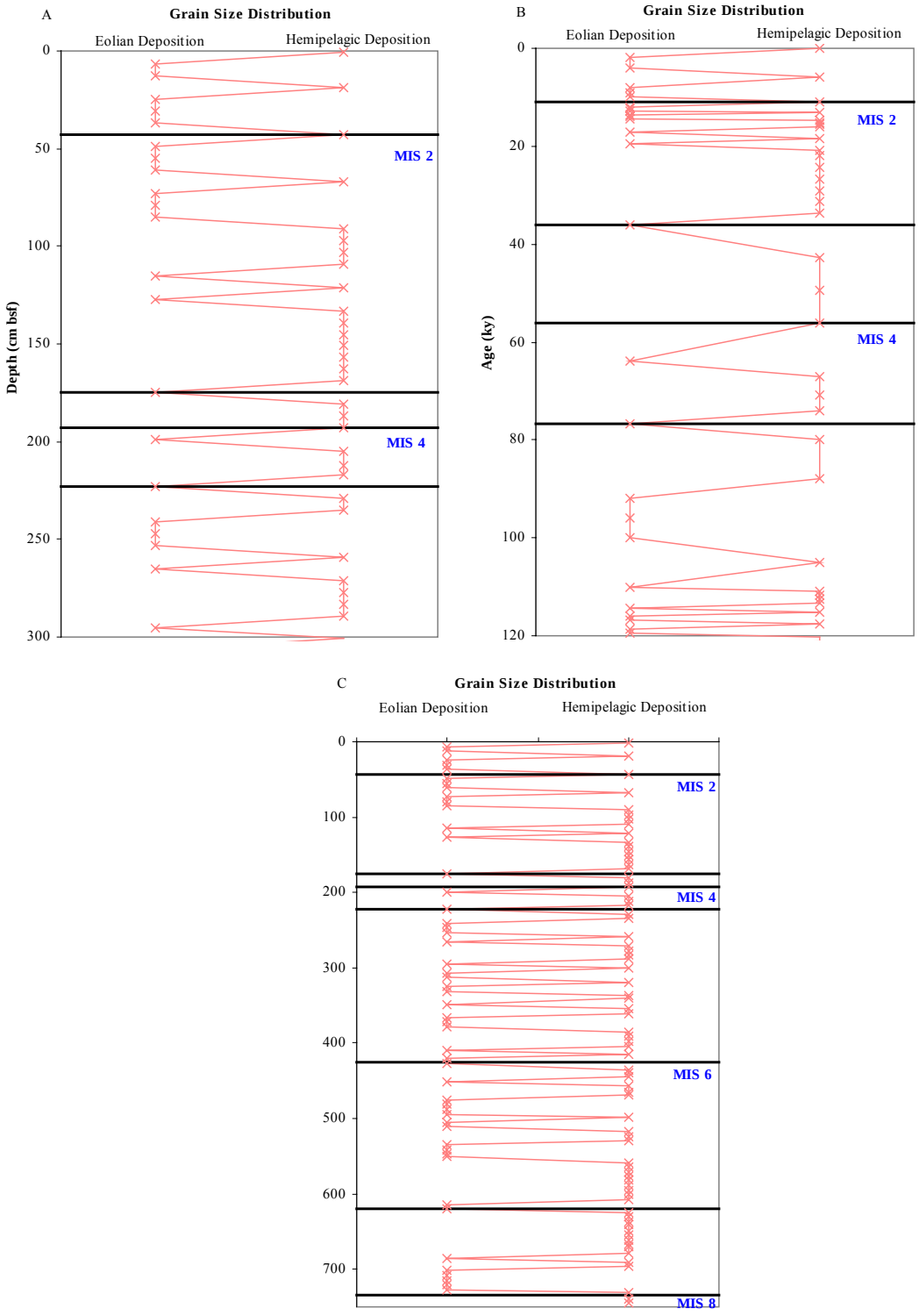

FIGURE 3.6: Grain-size distribution plotted against depth (A) and age (B) to the extent of the age model. Grain-size distribution plotted for all samples analyzed (C). Eolian and hemipelagic distributions based on Rea and Hovan (1995).

A Sample 1H1W 12-14

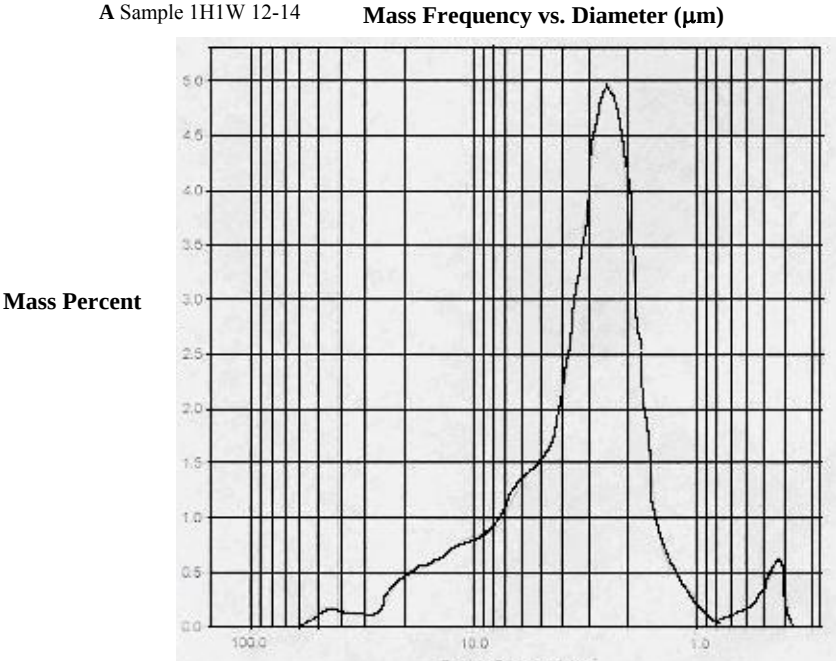

B Sample 1H1W 0-2

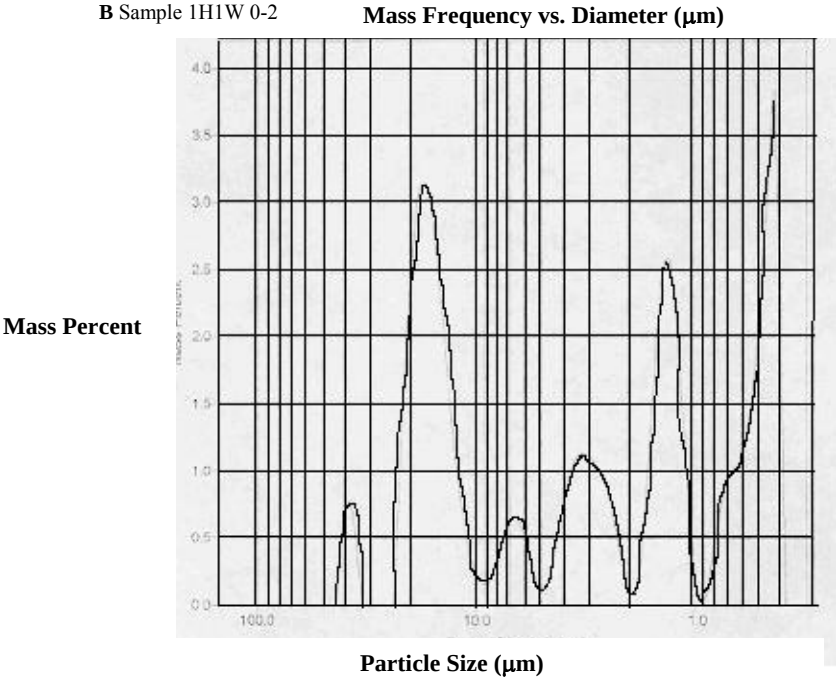

FIGURE 3.7: Example of typical eolian (A) and hemipelagic (B) grain-size distributions.

TABLE 3.3 Median grain-size and depth for all samples; age for samples 1-H 1-W 0-2 through 1-H 3-W 54-56

Sample	Depth (cm bsf)	Age (ky)	Median Grain Size (μm)
1-H 1-W 0-2	1	0.0	1.18
1-H 1-W 6-8	7	2.0	2.00
1-H 1-W 12-14	13	4.0	2.82
1-H 1-W 18-20	19	6.0	0.61
1-H 1-W 24-26	25	8.0	3.90
1-H 1-W 30-32	31	9.0	3.72
1-H 1-W 36-38	37	10.0	4.23
1-H 1-W 42-44	43	11.0	1.06
1-H 1-W 48-50	49	12.0	3.32
1-H 1-W 54-56	55	12.4	3.96
1-H 1-W 60-62	61	12.8	3.29
1-H 1-W 66-68	67	13.2	0.59
1-H 1-W 72-74	73	13.6	4.11
1-H 1-W 78-80	79	14.0	3.37
1-H 1-W 84-86	85	14.4	4.33
1-H 1-W 90-92	91	14.8	12.43
1-H 1-W 96-98	97	15.2	3.90
1-H 1-W 102-104	103	15.6	4.05
1-H 1-W 108-110	109	16.0	4.22
1-H 1-W 114-116	115	17.2	2.08
1-H 1-W 120-122	121	18.4	0.99
1-H 1-W 126-128	127	19.6	2.22
1-H 1-W 132-134	133	20.8	1.84
1-H 1-W 138-140	139	22.0	0.39
1-H 1-W 144-146	145	24.3	0.84

Sample	Depth (cm bsf)	Age (ky)	Median Grain Size (μm)
1-H 2-W 0-2	151	26.7	0.61
1-H 2-W 6-8	157	29.0	0.49
1-H 2-W 12-14	163	31.3	0.88
1-H 2-W 18-20	169	33.7	1.62
1-H 2-W 24-26	175	36.0	0.91
1-H 2-W 30-32	181	42.7	0.67
1-H 2-W 36-38	187	49.3	0.74
1-H 2-W 42-44	193	56.0	1.77
1-H 2-W 48-50	199	64.0	1.18
1-H 2-W 54-56	205	67.2	0.79
1-H 2-W 61-63	212	70.9	3.65
1-H 2-W 66-68	217	73.9	0.39
1-H 2-W 72-74	223	76.8	2.08
1-H 2-W 78-80	229	80.0	0.50
1-H 2-W 84-86	235	88.0	1.62
1-H 2-W 90-92	241	92.0	3.85
1-H 2-W 96-98	247	96.0	7.79
1-H 2-W 102-104	253	100.0	4.68
1-H 2-W 108-110	259	105.0	4.26
1-H 2-W 114-116	265	110.0	1.29
1-H 2-W 120-122	271	110.9	13.25
1-H 2-W 126-128	277	111.7	4.73
1-H 2-W 132-134	283	112.6	0.70
1-H 2-W 138-140	289	113.4	0.71
1-H 2-W 144-146	295	114.3	0.68

Sample	Depth (cm bsf)	Age (ky)	Median Grain Size (μm)
1-H 3-W 0-2	301	115.1	1.16
1-H 3-W 6-8	307	116.0	0.90
1-H 3-W 11-13	312	116.9	0.39
1-H 3-W 18-20	319	117.7	2.96
1-H 3-W 24-26	325	118.6	2.01
1-H 3-W 30-32	331	119.4	4.07
1-H 3-W 36-38	337	120.3	1.89
1-H 3-W 40-42	341	121.1	1.42
1-H 3-W 48-50	349	122.0	0.39
1-H 3-W 54-56	355	122.9	2.93
1-H 3-W 60-62	361		5.60
1-H 3-W 65-67	366		0.39
1-H 3-W 70-72	371		1.58
1-H 3-W 78-80	379		1.80
1-H 3-W 84-86	385		1.22
1-H 3-W 90-92	391		1.61
1-H 3-W 96-98	397		1.91
1-H 3-W 104-106	405		2.99
1-H 3-W 108-110	409		1.66
1-H 3-W 114-116	415		3.38
1-H 3-W 120-122	421		1.26
1-H 3-W 126-128	427		1.06
1-H 3-W 134-136	435		2.83
1-H 3-W 138-140	439		4.30
1-H 3-W 144-146	445		1.28

TABLE 3.3 (continued)

Sample	Depth (cm bsf)	Median Grain Size (μm)
1-H 4-W 0-2	451	1.89
1-H 4-W 6-8	457	1.61
1-H 4-W 14-16	465	2.28
1-H 4-W 18-20	469	2.26
1-H 4-W 24-26	475	1.49
1-H 4-W 30-32	481	2.30
1-H 4-W 36-38	487	3.59
1-H 4-W 44-46	495	4.19
1-H 4-W 48-50	499	2.77
1-H 4-W 54-56	505	3.42
1-H 4-W 60-62	511	2.47
1-H 4-W 66-68	517	1.90
1-H 4-W 74-76	525	2.75
1-H 4-W 78-80	529	0.96
1-H 4-W 84-86	535	1.33
1-H 4-W 90-92	541	1.94
1-H 4-W 96-98	547	2.76
1-H 4-W 100-102	551	1.78
1-H 4-W 108-110	559	1.23
1-H 4-W 114-116	565	1.31
1-H 4-W 120-122	571	2.53
1-H 4-W 126-128	577	0.39
1-H 4-W 130-132	581	1.09
1-H 4-W 138-140	589	1.79
1-H 4-W 144-146	595	0.39

Sample	Depth (cm bsf)	Median Grain Size (μm)
1-H 5-W 0-2	601	8.12
1-H 5-W 6-8	607	6.45
1-H 5-W 14-16	615	1.88
1-H 5-W 18-20	619	1.28
1-H 5-W 24-26	625	1.48
1-H 5-W 30-32	631	0.39
1-H 5-W 36-38	637	2.83
1-H 5-W 40-42	641	3.94
1-H 5-W 48-50	649	2.52
1-H 5-W 54-56	655	2.04
1-H 5-W 60-62	661	2.08
1-H 5-W 66-68	667	3.64
1-H 5-W 70-72	671	2.29
1-H 5-W 78-80	679	3.67
1-H 5-W 84-86	685	3.39
1-H 5-W 90-92	691	1.95
1-H 5-W 96-98	697	1.67
1-H 5-W 100-102	701	0.39
1-H 5-W 108-110	709	1.93
1-H 5-W 114-116	715	1.83
1-H 5-W 120-122	721	3.10
1-H 5-W 126-128	727	3.15
1-H 5-W 130-132	731	0.39
1-H 5-W 138-140	739	2.70
1-H 5-W 144-146	745	2.72

TABLE 3.4 Grain-size distribution and depth for all samples; age for samples 1-H 1-W 0-2 through 1-H 3-W 54-56
E indicates eolian deposition and H indicates hemipelagic deposition of sediment.

Sample	Depth (cm bsf)	Age (ky)	Distribution Classification
1-H 1-W 0-2	1	0.0	H
1-H 1-W 6-8	7	2.0	E
1-H 1-W 12-14	13	4.0	E
1-H 1-W 18-20	19	6.0	H
1-H 1-W 24-26	25	8.0	E
1-H 1-W 30-32	31	9.0	E
1-H 1-W 36-38	37	10.0	E
1-H 1-W 42-44	43	11.0	H
1-H 1-W 48-50	49	12.0	E
1-H 1-W 54-56	55	12.4	E
1-H 1-W 60-62	61	12.8	E
1-H 1-W 66-68	67	13.2	H
1-H 1-W 72-74	73	13.6	E
1-H 1-W 78-80	79	14.0	E
1-H 1-W 84-86	85	14.4	E
1-H 1-W 90-92	91	14.8	H
1-H 1-W 96-98	97	15.2	H
1-H 1-W 102-104	103	15.6	H
1-H 1-W 108-110	109	16.0	H
1-H 1-W 114-116	115	17.2	E
1-H 1-W 120-122	121	18.4	H
1-H 1-W 126-128	127	19.6	E
1-H 1-W 132-134	133	20.8	H
1-H 1-W 138-140	139	22.0	H
1-H 1-W 144-146	145	24.3	H

Sample	Depth (cm bsf)	Age (ky)	Distribution Classification
1-H 2-W 0-2	151	26.7	H
1-H 2-W 6-8	157	29.0	H
1-H 2-W 12-14	163	31.3	H
1-H 2-W 18-20	169	33.7	H
1-H 2-W 24-26	175	36.0	E
1-H 2-W 30-32	181	42.7	H
1-H 2-W 36-38	187	49.3	H
1-H 2-W 42-44	193	56.0	H
1-H 2-W 48-50	199	64.0	E
1-H 2-W 54-56	205	67.2	H
1-H 2-W 61-63	212	70.9	H
1-H 2-W 66-68	217	73.9	H
1-H 2-W 72-74	223	76.8	E
1-H 2-W 78-80	229	80.0	H
1-H 2-W 84-86	235	88.0	H
1-H 2-W 90-92	241	92.0	E
1-H 2-W 96-98	247	96.0	E
1-H 2-W 102-104	253	100.0	E
1-H 2-W 108-110	259	105.0	H
1-H 2-W 114-116	265	110.0	E
1-H 2-W 120-122	271	110.9	H
1-H 2-W 126-128	277	111.7	H
1-H 2-W 132-134	283	112.6	H
1-H 2-W 138-140	289	113.4	H
1-H 2-W 144-146	295	114.3	E

Sample	Depth (cm bsf)	Age (ky)	Distribution Classification
1-H 3-W 0-2	301	115.1	H
1-H 3-W 6-8	307	116.0	E
1-H 3-W 11-13	312	116.9	E
1-H 3-W 18-20	319	117.7	H
1-H 3-W 24-26	325	118.6	E
1-H 3-W 30-32	331	119.4	E
1-H 3-W 36-38	337	120.3	H
1-H 3-W 40-42	341	121.1	H
1-H 3-W 48-50	349	122.0	E
1-H 3-W 54-56	355	122.9	H
1-H 3-W 60-62	361		H
1-H 3-W 65-67	366		E
1-H 3-W 70-72	371		E
1-H 3-W 78-80	379		E
1-H 3-W 84-86	385		H
1-H 3-W 90-92	391		H
1-H 3-W 96-98	397		H
1-H 3-W 104-106	405		H
1-H 3-W 108-110	409		E
1-H 3-W 114-116	415		H
1-H 3-W 120-122	421		E
1-H 3-W 126-128	427		E
1-H 3-W 134-136	435		H
1-H 3-W 138-140	439		H
1-H 3-W 144-146	445		H

TABLE 3.4 (continued)

Sample	Depth (cm bsf)	Distribution Classification
1-H 4-W 0-2	451	E
1-H 4-W 6-8	457	H
1-H 4-W 14-16	465	H
1-H 4-W 18-20	469	H
1-H 4-W 24-26	475	E
1-H 4-W 30-32	481	E
1-H 4-W 36-38	487	E
1-H 4-W 44-46	495	E
1-H 4-W 48-50	499	H
1-H 4-W 54-56	505	E
1-H 4-W 60-62	511	E
1-H 4-W 66-68	517	H
1-H 4-W 74-76	525	H
1-H 4-W 78-80	529	H
1-H 4-W 84-86	535	E
1-H 4-W 90-92	541	E
1-H 4-W 96-98	547	E
1-H 4-W 100-102	551	E
1-H 4-W 108-110	559	H
1-H 4-W 114-116	565	H
1-H 4-W 120-122	571	H
1-H 4-W 126-128	577	H
1-H 4-W 130-132	581	H
1-H 4-W 138-140	589	H
1-H 4-W 144-146	595	H

Sample	Depth (cm bsf)	Distribution Classification
1-H 5-W 0-2	601	H
1-H 5-W 6-8	607	H
1-H 5-W 14-16	615	E
1-H 5-W 18-20	619	E
1-H 5-W 24-26	625	H
1-H 5-W 30-32	631	H
1-H 5-W 36-38	637	H
1-H 5-W 40-42	641	H
1-H 5-W 48-50	649	H
1-H 5-W 54-56	655	H
1-H 5-W 60-62	661	H
1-H 5-W 66-68	667	H
1-H 5-W 70-72	671	H
1-H 5-W 78-80	679	H
1-H 5-W 84-86	685	E
1-H 5-W 90-92	691	H
1-H 5-W 96-98	697	H
1-H 5-W 100-102	701	E
1-H 5-W 108-110	709	E
1-H 5-W 114-116	715	E
1-H 5-W 120-122	721	E
1-H 5-W 126-128	727	E
1-H 5-W 130-132	731	H
1-H 5-W 138-140	739	H
1-H 5-W 144-146	745	H

3.3 Weight Percent Sand and Color Reflectance

Weight percent sand (wt.% sand) is plotted against depth (cm bsf) and age (ky) in Figure 3.8. The overall average wt.% sand is 29.75. Between 0 and 80 cm bsf, there is little variation and an average wt.% sand of 21.06. A slightly larger average of 48.96 wt.% sand dominates between 85 to 151 cm bsf (samples 1H1W 84-86 through 1H2W 0-2). The average wt.% sand between 157 and 265 cm bsf (samples 1H2W 6-8 through 1H2W 114-116) is 32.20. There is a maximum peak in wt.% sand (73.26) at 271 cm bsf (1H2W 120-122) and below that until 457 cm bsf (1H4W 6-8), the average wt.% sand is 24.93. A second peak (44.85 wt.% sand) is seen at 465 cm bsf (1H4W 14-16) and below that, there is a relatively gradual change from lower weight percent sands to nearly 50%, followed by a shift back to lower weigh percent sands below 601 cm bsf (1H5W 0-2). The average wt.% sand of this interval is 28.36. The color reflectance was gathered shipboard (Vidal et al., 1998) and is also plotted with depth (cm bsf) and age (ky) in Figure 3.3. The average total color reflectance for the study interval is 49.82%. Table 3.5 provides the wt.% sand for all samples used in this study.

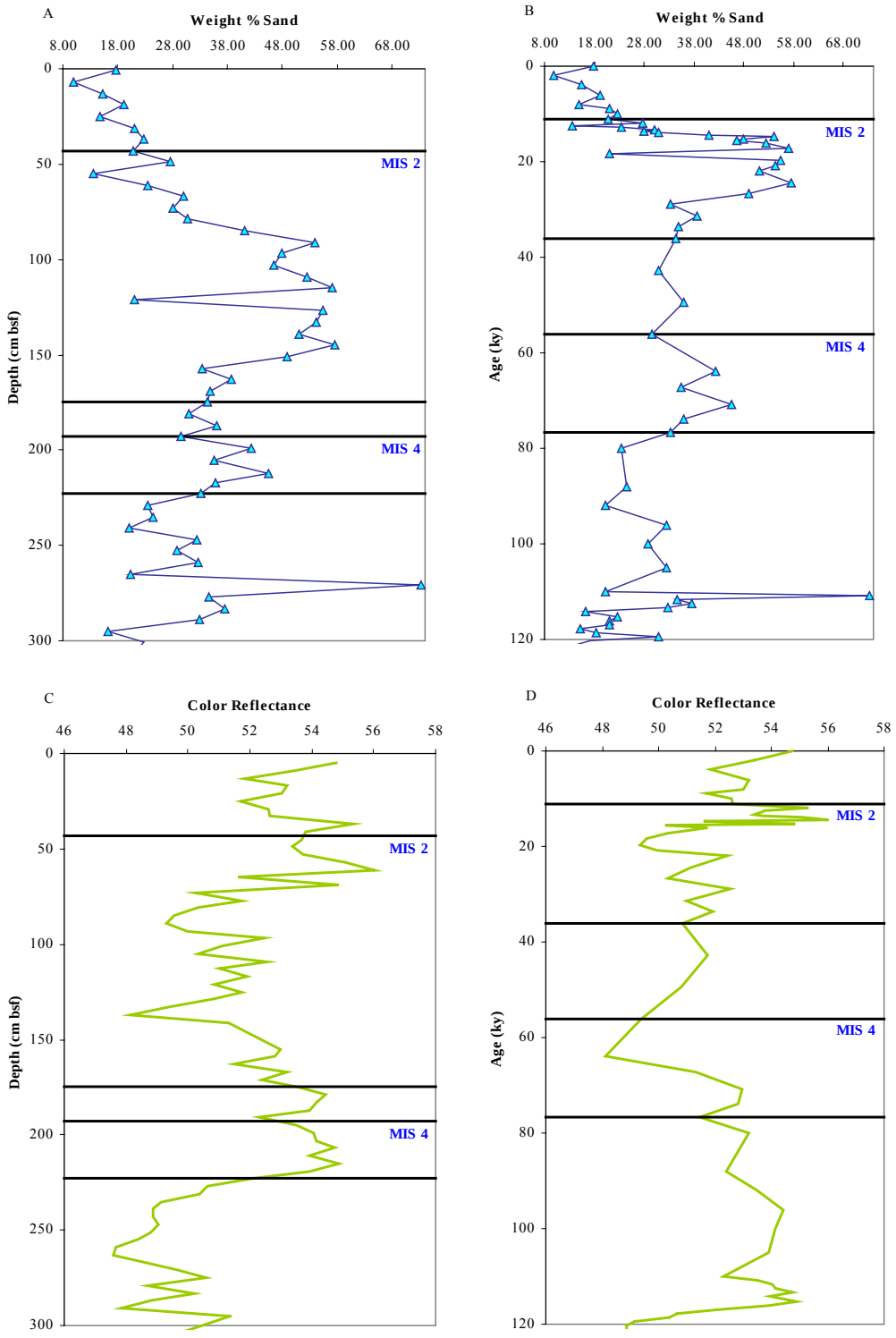
A
Weight % Sand
8.00 18.00 28.00 38.00 48.00 58.00 68.00
Depth (cm bsf)
0 50 100 150 200 250 300
MIS 2
MIS 4
B
Weight % Sand
8.00 18.00 28.00 38.00 48.00 58.00 68.00
Age (ky)
0 20 40 60 80 100 120
MIS 2
MIS 4
C
Color Reflectance
46 48 50 52 54 56 58
Depth (cm bsf)
0 50 100 150 200 250 300
MIS 2
MIS 4
D
Color Reflectance
46 48 50 52 54 56 58
Age (ky)
0 20 40 60 80 100 120
MIS 2
MIS 4

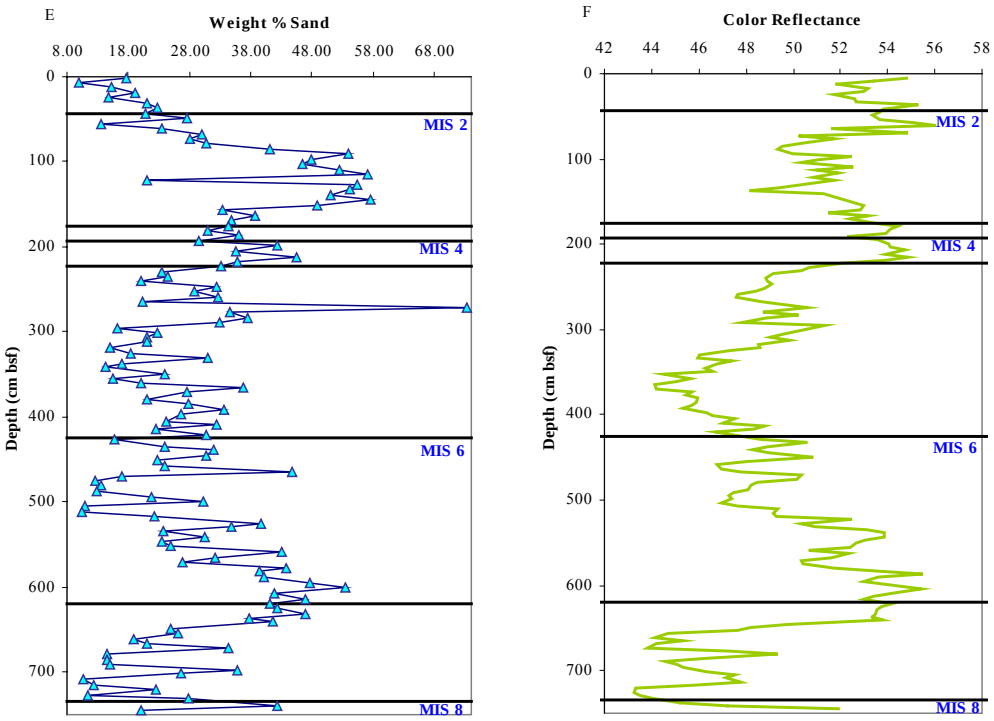

FIGURE 3.8: Weight % sand (A, B) and color reflectance (C, D) plotted against depth (A, C) and age (B, D) to the extent of the age model. Weight % sand (E) and color reflectance (F) plotted for all samples analyzed.

TABLE 3.5 Weight percent sand and depth for all samples; age for samples 1-H 1-W 0-2 through 1-H 3-W 54-56

Sample	Depth (cm bsf)	Age (ky)	Wt. % Sand
1-H 1-W 0-2	1	0.0	17.77
1-H 1-W 6-8	7	2.0	9.93
1-H 1-W 12-14	13	4.0	15.35
1-H 1-W 18-20	19	6.0	19.13
1-H 1-W 24-26	25	8.0	14.88
1-H 1-W 30-32	31	9.0	20.98
1-H 1-W 36-38	37	10.0	22.68
1-H 1-W 42-44	43	11.0	20.77
1-H 1-W 48-50	49	12.0	27.63
1-H 1-W 54-56	55	12.4	13.53
1-H 1-W 60-62	61	12.8	23.39
1-H 1-W 66-68	67	13.2	30.00
1-H 1-W 72-74	73	13.6	28.01
1-H 1-W 78-80	79	14.0	30.83
1-H 1-W 84-86	85	14.4	41.01
1-H 1-W 90-92	91	14.8	54.03
1-H 1-W 96-98	97	15.2	47.96
1-H 1-W 102-104	103	15.6	46.55
1-H 1-W 108-110	109	16.0	52.44
1-H 1-W 114-116	115	17.2	57.04
1-H 1-W 120-122	121	18.4	21.16
1-H 1-W 126-128	127	19.6	55.42
1-H 1-W 132-134	133	20.8	54.22
1-H 1-W 138-140	139	22.0	51.15
1-H 1-W 144-146	145	24.3	57.59

Sample	Depth (cm bsf)	Age (ky)	Wt. % Sand
1-H 2-W 0-2	151	26.7	48.91
1-H 2-W 6-8	157	29.0	33.39
1-H 2-W 12-14	163	31.3	38.63
1-H 2-W 18-20	169	33.7	34.77
1-H 2-W 24-26	175	36.0	34.25
1-H 2-W 30-32	181	42.7	30.90
1-H 2-W 36-38	187	49.3	35.95
1-H 2-W 42-44	193	56.0	29.46
1-H 2-W 48-50	199	64.0	42.39
1-H 2-W 54-56	205	67.2	35.45
1-H 2-W 61-63	212	70.9	45.49
1-H 2-W 66-68	217	73.9	35.81
1-H 2-W 72-74	223	76.8	33.17
1-H 2-W 78-80	229	80.0	23.38
1-H 2-W 84-86	235	88.0	24.40
1-H 2-W 90-92	241	92.0	20.17
1-H 2-W 96-98	247	96.0	32.51
1-H 2-W 102-104	253	100.0	28.74
1-H 2-W 108-110	259	105.0	32.54
1-H 2-W 114-116	265	110.0	20.33
1-H 2-W 120-122	271	110.9	73.26
1-H 2-W 126-128	277	111.7	34.62
1-H 2-W 132-134	283	112.6	37.47
1-H 2-W 138-140	289	113.4	32.81
1-H 2-W 144-146	295	114.29	16.31

Sample	Depth (cm bsf)	Age (ky)	Wt. % Sand
1-H 3-W 0-2	301	115.1	22.68
1-H 3-W 6-8	307	116.0	20.95
1-H 3-W 11-13	312	116.9	21.08
1-H 3-W 18-20	319	117.7	15.10
1-H 3-W 24-26	325	118.6	18.38
1-H 3-W 30-32	331	119.4	30.88
1-H 3-W 36-38	337	120.3	17.01
1-H 3-W 40-42	341	121.1	14.40
1-H 3-W 48-50	349	122.0	23.84
1-H 3-W 54-56	355	122.9	15.38
1-H 3-W 60-62	361		19.97
1-H 3-W 65-67	366		36.84
1-H 3-W 70-72	371		27.64
1-H 3-W 78-80	379		21.05
1-H 3-W 84-86	385		27.72
1-H 3-W 90-92	391		33.67
1-H 3-W 96-98	397		26.60
1-H 3-W 104-106	405		24.28
1-H 3-W 108-110	409		32.38
1-H 3-W 114-116	415		22.40
1-H 3-W 120-122	421		30.71
1-H 3-W 126-128	427		15.73
1-H 3-W 134-136	435		23.98
1-H 3-W 138-140	439		31.83
1-H 3-W 144-146	445		30.63

TABLE 3.5 (continued)

Sample	Depth (cm bsf)	Wt. % Sand	Sample	Depth (cm bsf)	Wt. % Sand
1-H 4-W 0-2	451	22.78	1-H 5-W 0-2	601	53.35
1-H 4-W 6-8	457	23.84	1-H 5-W 6-8	607	41.77
1-H 4-W 14-16	465	44.85	1-H 5-W 14-16	615	46.81
1-H 4-W 18-20	469	16.97	1-H 5-W 18-20	619	41.08
1-H 4-W 24-26	475	12.49	1-H 5-W 24-26	625	42.22
1-H 4-W 30-32	481	13.62	1-H 5-W 30-32	631	47.01
1-H 4-W 36-38	487	12.90	1-H 5-W 36-38	637	37.82
1-H 4-W 44-46	495	21.90	1-H 5-W 40-42	641	41.65
1-H 4-W 48-50	499	30.15	1-H 5-W 48-50	649	24.93
1-H 4-W 54-56	505	10.84	1-H 5-W 54-56	655	26.03
1-H 4-W 60-62	511	10.51	1-H 5-W 60-62	661	18.93
1-H 4-W 66-68	517	22.32	1-H 5-W 66-68	667	21.14
1-H 4-W 74-76	525	39.72	1-H 5-W 70-72	671	34.27
1-H 4-W 78-80	529	34.72	1-H 5-W 78-80	679	14.57
1-H 4-W 84-86	535	23.71	1-H 5-W 84-86	685	14.65
1-H 4-W 90-92	541	30.46	1-H 5-W 90-92	691	15.00
1-H 4-W 96-98	547	23.54	1-H 5-W 96-98	697	35.90
1-H 4-W 100-102	551	25.00	1-H 5-W 100-102	701	26.66
1-H 4-W 108-110	559	43.06	1-H 5-W 108-110	709	10.76
1-H 4-W 114-116	565	32.16	1-H 5-W 114-116	715	12.40
1-H 4-W 120-122	571	26.76	1-H 5-W 120-122	721	22.59
1-H 4-W 126-128	577	43.76	1-H 5-W 126-128	727	11.37
1-H 4-W 130-132	581	39.51	1-H 5-W 130-132	731	27.76
1-H 4-W 138-140	589	40.13	1-H 5-W 138-140	739	42.33
1-H 4-W 144-146	595	47.67	1-H 5-W 144-146	745	20.21

3.4 Percent Calcium Carbonate

The average concentration calcium carbonate (%$CaCO_3$) for this study is 70.55%, with a range of values between 54.30% (1H5W 96-98) and 83.08% (1H2W 48-50), as seen in Figure 3.9. Between 0 and 85 cm bsf, samples 1H1W 0-2 and 1H1W 84-86, the average %$CaCO_3$ is 72.76, with very little variation. There are two intervals in which the %$CaCO_3$ increases to just above 80% and then becomes lower again: 97 to 235 cm bsf (1H1W 96-98 to 1H2W 84-86) and 559 to 649 cm bsf (1H4W 108-110 to 1H5W 48-50). The absolute minimum %$CaCO_3$ value (54.30%) is at 697 cm bsf (1H5W 96-98) with a second minimum of 57.00% at 397 cm bsf (1H3W 96-98) and 405 cm bsf (1H3W 104-106). Table 3.6 provides results of %$CaCO_3$ analysis.

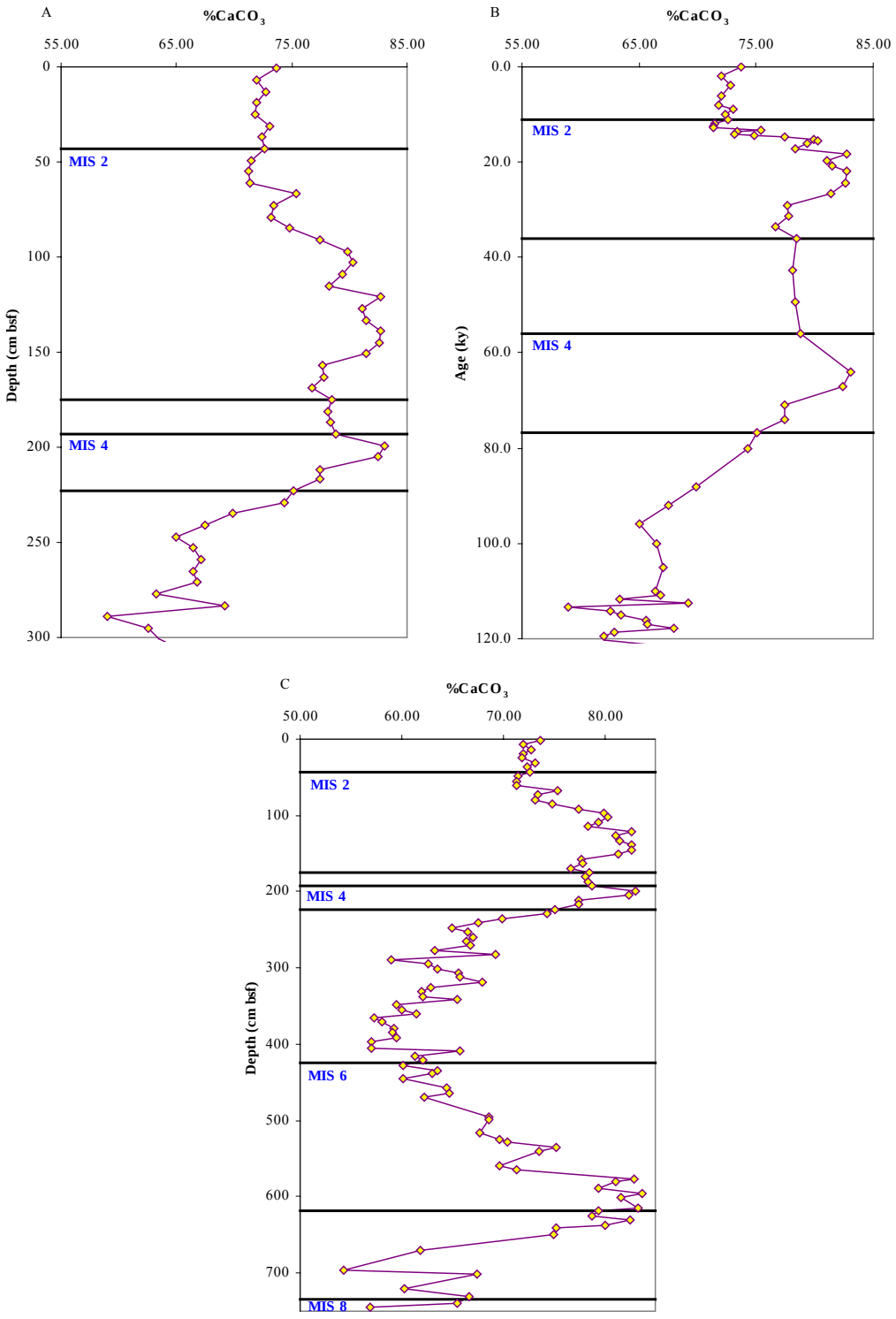

FIGURE 3.9: Percent $CaCO_3$ plotted against depth (A) and age (B) to the extent of the age model. Percent $CaCO_3$ plotted for all samples analyzed (C).

TABLE 3.6 Percent $CaCO_3$ and depth for selected samples; age for samples 1-H 1-W 0-2 through 1-H 3-W 54-56

Sample	Depth (cm bsf)	Age (ky)	%$CaCO_3$
1-H 1-W 0-2	1	0.0	73.70
1-H 1-W 6-8	7	2.0	72.00
1-H 1-W 12-14	13	4.0	72.80
1-H 1-W 18-20	19	6.0	72.00
1-H 1-W 24-26	25	8.0	71.80
1-H 1-W 30-32	31	9.0	73.10
1-H 1-W 36-38	37	10.0	72.40
1-H 1-W 42-44	43	11.0	72.60
1-H 1-W 48-50	49	12.0	71.50
1-H 1-W 54-56	55	12.4	71.30
1-H 1-W 60-62	61	12.8	71.40
1-H 1-W 66-68	67	13.2	75.40
1-H 1-W 72-74	73	13.6	73.40
1-H 1-W 78-80	79	14.0	73.20
1-H 1-W 84-86	85	14.4	74.80
1-H 1-W 90-92	91	14.8	77.40
1-H 1-W 96-98	97	15.2	79.90
1-H 1-W 102-104	103	15.6	80.30
1-H 1-W 108-110	109	16.0	79.40
1-H 1-W 114-116	115	17.2	78.3
1-H 1-W 120-122	121	18.4	82.70
1-H 1-W 126-128	127	19.6	81.10
1-H 1-W 132-134	133	20.8	81.50
1-H 1-W 138-140	139	22.0	82.70
1-H 1-W 144-146	145	24.3	82.60

Sample	Depth (cm bsf)	Age (ky)	%$CaCO_3$
1-H 2-W 0-2	151	26.7	81.40
1-H 2-W 6-8	157	29.0	77.70
1-H 2-W 12-14	163	31.3	77.80
1-H 2-W 18-20	169	33.7	76.70
1-H 2-W 24-26	175	36.0	78.50
1-H 2-W 30-32	181	42.7	78.16
1-H 2-W 36-38	187	49.3	78.40
1-H 2-W 42-44	193	56.0	78.80
1-H 2-W 48-50	199	64.0	83.08
1-H 2-W 54-56	205	67.2	82.45
1-H 2-W 61-63	212	70.9	77.40
1-H 2-W 66-68	217	73.9	77.40
1-H 2-W 72-74	223	76.8	75.10
1-H 2-W 78-80	229	80.0	74.30
1-H 2-W 84-86	235	88.0	69.90
1-H 2-W 90-92	241	92.0	67.50
1-H 2-W 96-98	247	96.0	65.00
1-H 2-W 102-104	253	100.0	66.50
1-H 2-W 108-110	259	105.0	67.10
1-H 2-W 114-116	265	110.0	66.40
1-H 2-W 120-122	271	110.9	66.80
1-H 2-W 126-128	277	111.7	63.30
1-H 2-W 132-134	283	112.6	69.20
1-H 2-W 138-140	289	113.4	59.00
1-H 2-W 144-146	295	114.3	62.60

Sample	Depth (cm bsf)	Age (ky)	%$CaCO_3$
1-H 3-W 0-2	301	115.1	63.50
1-H 3-W 6-8	307	116.0	65.60
1-H 3-W 11-13	312	116.9	65.70
1-H 3-W 18-20	319	117.7	67.92
1-H 3-W 24-26	325	118.6	62.90
1-H 3-W 30-32	331	119.4	62.00
1-H 3-W 36-38	337	120.3	62.10
1-H 3-W 40-42	341	121.1	65.46
1-H 3-W 48-50	349	122.0	59.50
1-H 3-W 54-56	355	122.9	60.01
1-H 3-W 60-62	361		61.45
1-H 3-W 65-67	366		57.30
1-H 3-W 70-72	371		58.10
1-H 3-W 78-80	379		59.25
1-H 3-W 84-86	385		59.10
1-H 3-W 90-92	391		59.50
1-H 3-W 96-98	397		57.00
1-H 3-W 104-106	405		57.00
1-H 3-W 108-110	409		65.76
1-H 3-W 114-116	415		61.28
1-H 3-W 120-122	421		62.10
1-H 3-W 126-128	427		60.10
1-H 3-W 134-136	435		63.50
1-H 3-W 138-140	439		62.96
1-H 3-W 144-146	445		60.10

TABLE 3.6 (continued)

Sample	Depth (cm bsf)	%$CaCO_3$
1-H 4-W 6-8	457	64.43
1-H 4-W 14-16	465	64.70
1-H 4-W 18-20	469	62.20
1-H 4-W 44-46	495	68.60
1-H 4-W 48-50	499	68.60
1-H 4-W 66-68	517	67.70
1-H 4-W 74-76	525	69.67
1-H 4-W 78-80	529	70.40
1-H 4-W 84-86	535	75.24
1-H 4-W 90-92	541	73.50
1-H 4-W 108-110	559	69.60
1-H 4-W 114-116	565	71.40
1-H 4-W 126-128	577	82.86
1-H 4-W 130-132	581	81.13
1-H 4-W 138-140	589	79.40
1-H 4-W 144-146	595	83.64

Sample	Depth (cm bsf)	%$CaCO_3$
1-H 5-W 0-2	601	81.60
1-H 5-W 14-16	615	83.28
1-H 5-W 18-20	619	79.42
1-H 5-W 24-26	625	78.70
1-H 5-W 30-32	631	82.59
1-H 5-W 36-38	637	80.00
1-H 5-W 40-42	641	75.30
1-H 5-W 48-50	649	74.93
1-H 5-W 70-72	671	61.90
1-H 5-W 96-98	697	54.30
1-H 5-W 100-102	701	67.40
1-H 5-W 120-122	721	60.30
1-H 5-W 130-132	731	66.66
1-H 5-W 138-140	739	65.48
1-H 5-W 144-146	745	56.88

3.6 C/N Ratio

The average C/N ratio is 7.99 with the majority of samples falling within the 4-10 range of marine algae (Meyers, 1994). The C/N ratio is plotted against depth (cm bsf) in Figure 3.10 and the data are provided in Table 3.7. Sample 1H3W 54-56, which is found at a depth of 355 cm bsf, has a C/N ratio of 23.9, suggesting a greater input of carbon from vascular land plants. The range of ratio values between 10 and 20 indicate mixing of carbon from both marine and terrigenous sources. Negative C/N ratios are seen in samples 1H4W 126-128, 577 cm bsf, and 1H4W 130-132 cm, 581 cm bsf. These negative values of –1.8 and –0.4, respectively, indicate an excess of refractory N in the system.

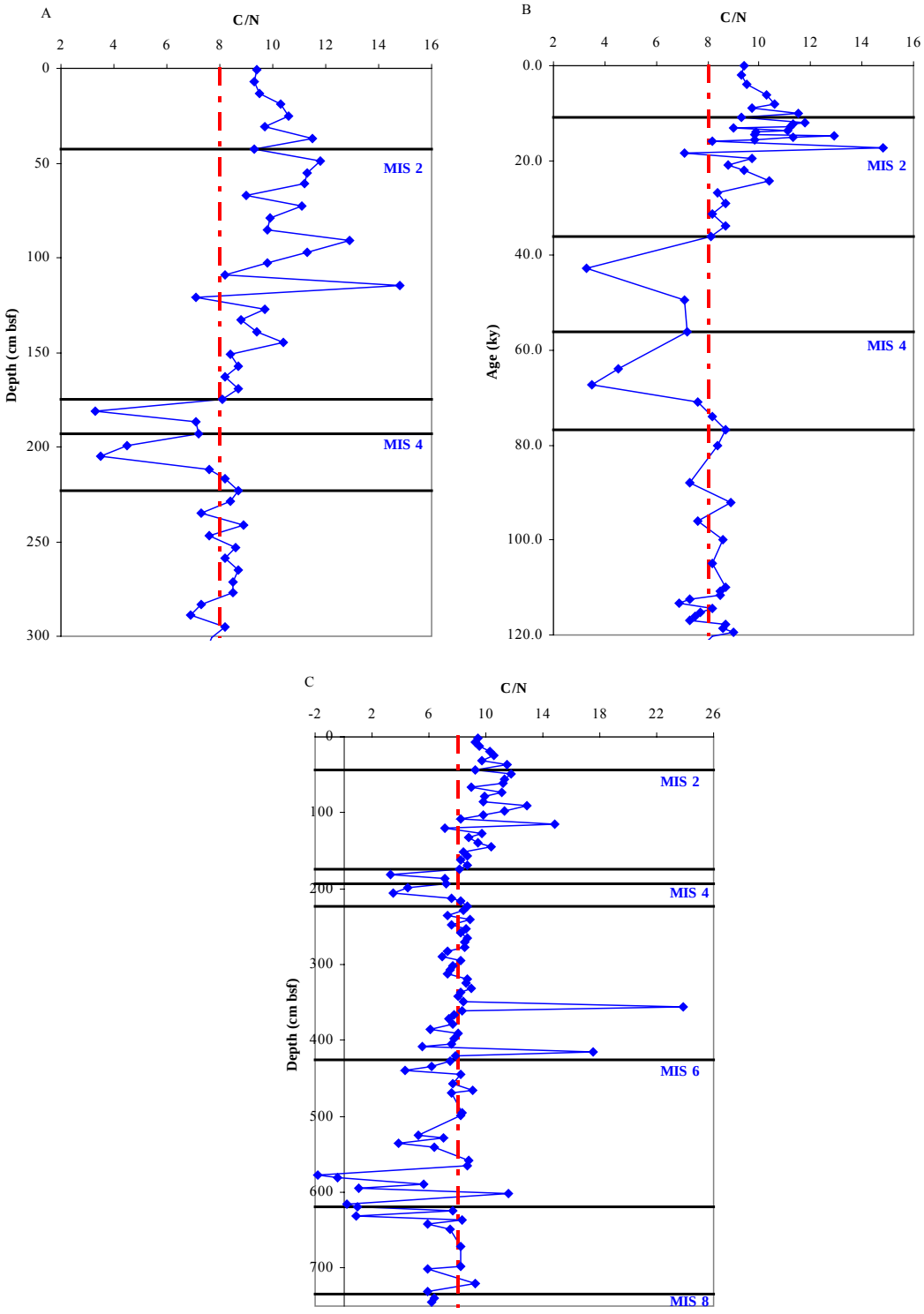

FIGURE 3.10: C/N ratio plotted against depth (A) and age (B) to the extent of the age model. C/N ratios plotted against depth for all samples analyzed (C). Values to the right of the dashed red line (C/N = 8) indicate a mixed source for carbon and values to the left indicate a marine source of carbon. C/N > 20 indicate carbon input from vascular land plants.

TABLE 3.7 C/N ratio and depth for selected samples; age for samples 1-H 1-W 0-2 through 1-H 3-W 54-56

Sample	Depth (cm bsf)	Age (ky)	C/N
1-H 1-W 0-2	1	0.0	9.4
1-H 1-W 6-8	7	2.0	9.3
1-H 1-W 12-14	13	4.0	9.5
1-H 1-W 18-20	19	6.0	10.3
1-H 1-W 24-26	25	8.0	10.6
1-H 1-W 30-32	31	9.0	9.7
1-H 1-W 36-38	37	10.0	11.5
1-H 1-W 42-44	43	11.0	9.3
1-H 1-W 48-50	49	12.0	11.8
1-H 1-W 54-56	55	12.4	11.3
1-H 1-W 60-62	61	12.8	11.2
1-H 1-W 66-68	67	13.2	9
1-H 1-W 72-74	73	13.6	11.1
1-H 1-W 78-80	79	14.0	9.9
1-H 1-W 84-86	85	14.4	9.8
1-H 1-W 90-92	91	14.8	12.9
1-H 1-W 96-98	97	15.2	11.3
1-H 1-W 102-104	103	15.6	9.8
1-H 1-W 108-110	109	16.0	8.2
1-H 1-W 114-116	115	17.2	14.8
1-H 1-W 120-122	121	18.4	7.1
1-H 1-W 126-128	127	19.6	9.7
1-H 1-W 132-134	133	20.8	8.8
1-H 1-W 138-140	139	22.0	9.4
1-H 1-W 144-146	145	24.3	10.4

Sample	Depth (cm bsf)	Age (ky)	C/N
1-H 2-W 0-2	151	26.7	8.4
1-H 2-W 6-8	157	29.0	8.7
1-H 2-W 12-14	163	31.3	8.2
1-H 2-W 18-20	169	33.7	8.7
1-H 2-W 24-26	175	36.0	8.1
1-H 2-W 30-32	181	42.7	3.3
1-H 2-W 36-38	187	49.3	7.1
1-H 2-W 42-44	193	56.0	7.2
1-H 2-W 48-50	199	64.0	4.5
1-H 2-W 54-56	205	67.2	3.5
1-H 2-W 61-63	212	70.9	7.6
1-H 2-W 66-68	217	73.9	8.2
1-H 2-W 72-74	223	76.8	8.7
1-H 2-W 78-80	229	80.0	8.4
1-H 2-W 84-86	235	88.0	7.3
1-H 2-W 90-92	241	92.0	8.9
1-H 2-W 96-98	247	96.0	7.6
1-H 2-W 102-104	253	100.0	8.6
1-H 2-W 108-110	259	105.0	8.2
1-H 2-W 114-116	265	110.0	8.7
1-H 2-W 120-122	271	110.9	8.5
1-H 2-W 126-128	277	111.7	8.5
1-H 2-W 132-134	283	112.6	7.3
1-H 2-W 138-140	289	113.4	6.9
1-H 2-W 144-146	295	114.3	8.2

Sample	Depth (cm bsf)	Age (ky)	C/N
1-H 3-W 0-2	301	115.1	7.7
1-H 3-W 6-8	307	116.0	7.5
1-H 3-W 11-13	312	116.9	7.3
1-H 3-W 18-20	319	117.7	8.7
1-H 3-W 24-26	325	118.6	8.6
1-H 3-W 30-32	331	119.4	9
1-H 3-W 36-38	337	120.3	8.2
1-H 3-W 40-42	341	121.1	8
1-H 3-W 48-50	349	122.0	8.4
1-H 3-W 54-56	355	122.9	23.9
1-H 3-W 60-62	361		8.3
1-H 3-W 65-67	366		7.8
1-H 3-W 70-72	371		7.4
1-H 3-W 78-80	379		7.7
1-H 3-W 84-86	385		6.1
1-H 3-W 90-92	391		8
1-H 3-W 96-98	397		7.8
1-H 3-W 104-106	405		7.6
1-H 3-W 108-110	409		5.5
1-H 3-W 114-116	415		17.5
1-H 3-W 120-122	421		7.9
1-H 3-W 126-128	427		7.5
1-H 3-W 134-136	435		6.2
1-H 3-W 138-140	439		4.3
1-H 3-W 144-146	445		8.2

TABLE 3.7 (continued)

Sample	Depth (cm bsf)	C/N
1-H 4-W 6-8	457	7.7
1-H 4-W 14-16	465	9.1
1-H 4-W 18-20	469	7.6
1-H 4-W 44-46	495	8.3
1-H 4-W 48-50	499	8.2
1-H 4-W 74-76	525	5.3
1-H 4-W 78-80	529	7
1-H 4-W 84-86	535	3.9
1-H 4-W 90-92	541	6.4
1-H 4-W 108-110	559	8.8
1-H 4-W 114-116	565	8.7
1-H 4-W 126-128	577	-1.8
1-H 4-W 130-132	581	-0.4
1-H 4-W 138-140	589	5.6
1-H 4-W 144-146	595	1.1

Sample	Depth (cm bsf)	C/N
1-H 5-W 0-2	601	11.6
1-H 5-W 14-16	615	0.2
1-H 5-W 18-20	619	1
1-H 5-W 24-26	625	7.7
1-H 5-W 30-32	631	0.9
1-H 5-W 36-38	637	8.3
1-H 5-W 40-42	641	5.9
1-H 5-W 48-50	649	7.5
1-H 5-W 70-72	671	8.2
1-H 5-W 96-98	697	8.2
1-H 5-W 100-102	701	5.9
1-H 5-W 120-122	721	9.3
1-H 5-W 130-132	731	5.9
1-H 5-W 138-140	739	6.4
1-H 5-W 144-146	745	6.2

3.5 Percent Total Organic Carbon

The percent of total organic carbon (%TOC) is plotted against depth (cm bsf) and age (ky) in Figure 3.11. The average %TOC is 1.02. There are two peaks in %TOC; a peak of 2.51 at a depth of 355 cm bsf (1H3W 54-56) and a peak of 2.45 at a depth of 415 cm bsf (1H3W 114-116). A minimum %TOC (0.03) is found in sample 1H5W 14-16, at a depth of 615 cm bsf. Table 3.8 provides the %TOC data for the selected samples.

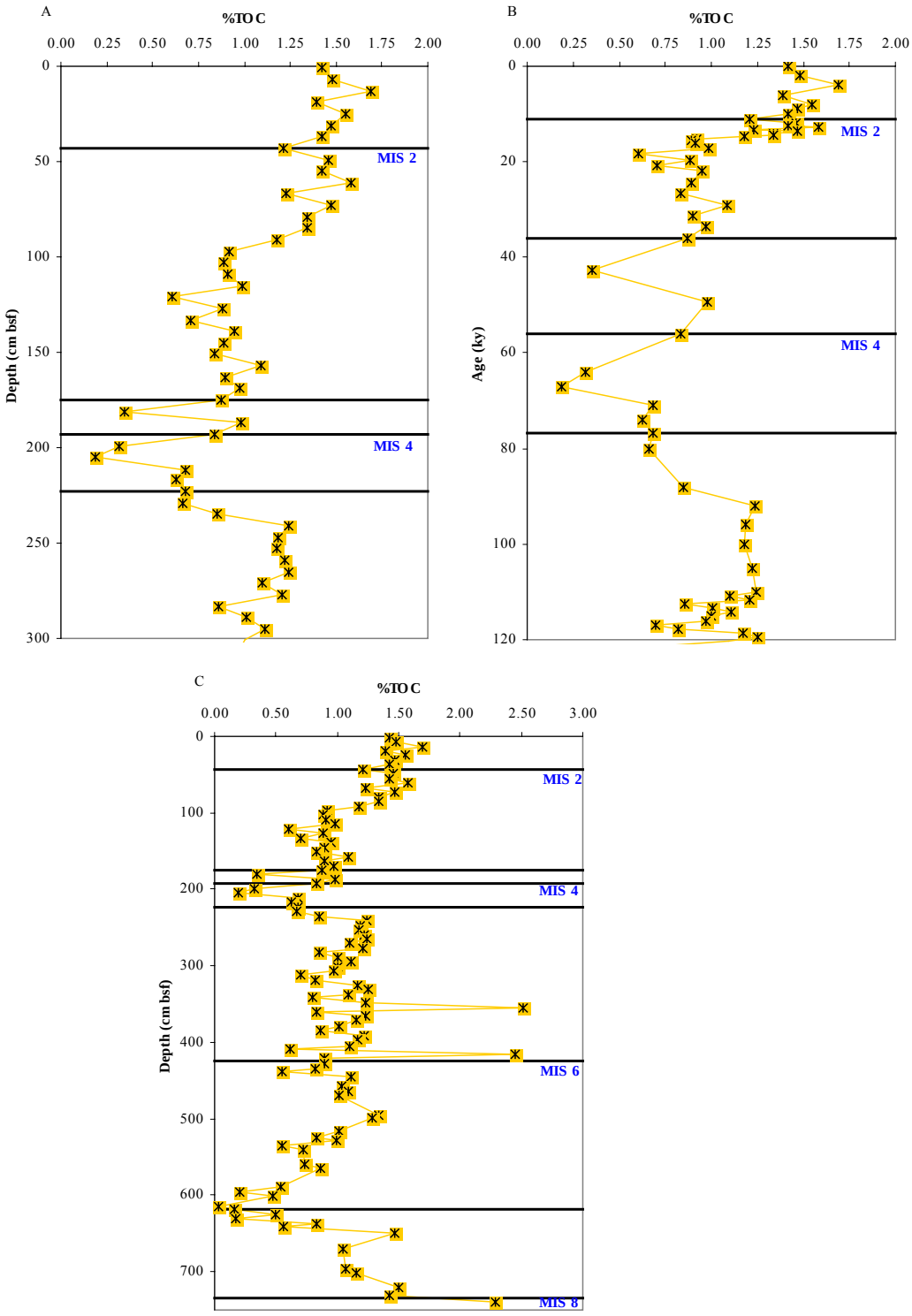

FIGURE 3.11: Percent TOC plotted against depth (A) and age (B) to the extent of the age model. Percent TOC plotted for all samples analyzed (C).

TABLE 3.8 Percent TOC and depth for selected samples; age for samples 1-H 1-W 0-2 through 1-H 3-W 54-56

Sample	Depth (cm bsf)	Age (ky)	%TOC
1-H 1-W 0-2	1	0.0	1.42
1-H 1-W 6-8	7	2.0	1.48
1-H 1-W 12-14	13	4.0	1.69
1-H 1-W 18-20	19	6.0	1.39
1-H 1-W 24-26	25	8.0	1.55
1-H 1-W 30-32	31	9.0	1.47
1-H 1-W 36-38	37	10.0	1.42
1-H 1-W 42-44	43	11.0	1.21
1-H 1-W 48-50	49	12.0	1.46
1-H 1-W 54-56	55	12.4	1.42
1-H 1-W 60-62	61	12.8	1.58
1-H 1-W 66-68	67	13.2	1.23
1-H 1-W 72-74	73	13.6	1.47
1-H 1-W 78-80	79	14.0	1.34
1-H 1-W 84-86	85	14.4	1.34
1-H 1-W 90-92	91	14.8	1.18
1-H 1-W 96-98	97	15.2	0.92
1-H 1-W 102-104	103	15.6	0.89
1-H 1-W 108-110	109	16.0	0.91
1-H 1-W 114-116	115	17.2	0.99
1-H 1-W 120-122	121	18.4	0.61
1-H 1-W 126-128	127	19.6	0.88
1-H 1-W 132-134	133	20.8	0.70
1-H 1-W 138-140	139	22.0	0.95
1-H 1-W 144-146	145	24.3	0.89

Sample	Depth (cm bsf)	Age (ky)	%TOC
1-H 2-W 0-2	151	26.7	0.84
1-H 2-W 6-8	157	29.0	1.09
1-H 2-W 12-14	163	31.3	0.90
1-H 2-W 18-20	169	33.7	0.97
1-H 2-W 24-26	175	36.0	0.87
1-H 2-W 30-32	181	42.7	0.35
1-H 2-W 36-38	187	49.3	0.98
1-H 2-W 42-44	193	56.0	0.84
1-H 2-W 48-50	199	64.0	0.32
1-H 2-W 54-56	205	67.2	0.19
1-H 2-W 61-63	212	70.9	0.68
1-H 2-W 66-68	217	73.9	0.62
1-H 2-W 72-74	223	76.8	0.68
1-H 2-W 78-80	229	80.0	0.66
1-H 2-W 84-86	235	88.0	0.85
1-H 2-W 90-92	241	92.0	1.24
1-H 2-W 96-98	247	96.0	1.19
1-H 2-W 102-104	253	100.0	1.18
1-H 2-W 108-110	259	105.0	1.22
1-H 2-W 114-116	265	110.0	1.24
1-H 2-W 120-122	271	110.9	1.10
1-H 2-W 126-128	277	111.7	1.21
1-H 2-W 132-134	283	112.6	0.86
1-H 2-W 138-140	289	113.4	1.01
1-H 2-W 144-146	295	114.3	1.11

Sample	Depth (cm bsf)	Age (ky)	%TOC
1-H 3-W 0-2	301	115.1	1.00
1-H 3-W 6-8	307	116.0	0.97
1-H 3-W 11-13	312	116.9	0.70
1-H 3-W 18-20	319	117.7	0.82
1-H 3-W 24-26	325	118.6	1.17
1-H 3-W 30-32	331	119.4	1.25
1-H 3-W 36-38	337	120.3	1.09
1-H 3-W 40-42	341	121.1	0.80
1-H 3-W 48-50	349	122.0	1.23
1-H 3-W 54-56	355	122.9	2.51
1-H 3-W 60-62	361		0.83
1-H 3-W 65-67	366		1.23
1-H 3-W 70-72	371		1.15
1-H 3-W 78-80	379		1.01
1-H 3-W 84-86	385		0.86
1-H 3-W 90-92	391		1.22
1-H 3-W 96-98	397		1.17
1-H 3-W 104-106	405		1.10
1-H 3-W 108-110	409		0.61
1-H 3-W 114-116	415		2.45
1-H 3-W 120-122	421		0.90
1-H 3-W 126-128	427		0.90
1-H 3-W 134-136	435		0.82
1-H 3-W 138-140	439		0.55
1-H 3-W 144-146	445		1.11

TABLE 3.8 (continued)

Sample	Depth (cm bsf)	%TOC
1-H 4-W 6-8	457	1.04
1-H 4-W 14-16	465	1.09
1-H 4-W 18-20	469	1.01
1-H 4-W 44-46	495	1.34
1-H 4-W 48-50	499	1.28
1-H 4-W 66-68	517	1.01
1-H 4-W 74-76	525	0.83
1-H 4-W 78-80	529	0.99
1-H 4-W 84-86	535	0.55
1-H 4-W 90-92	541	0.72
1-H 4-W 108-110	559	0.73
1-H 4-W 114-116	565	0.86
1-H 4-W 138-140	589	0.54
1-H 4-W 144-146	595	0.21

Sample	Depth (cm bsf)	%TOC
1-H 5-W 0-2	601	0.48
1-H 5-W 14-16	615	0.03
1-H 5-W 18-20	619	0.16
1-H 5-W 24-26	625	0.50
1-H 5-W 30-32	631	0.17
1-H 5-W 36-38	637	0.83
1-H 5-W 40-42	641	0.56
1-H 5-W 48-50	649	1.47
1-H 5-W 70-72	671	1.05
1-H 5-W 96-98	697	1.07
1-H 5-W 100-102	701	1.15
1-H 5-W 120-122	721	1.50
1-H 5-W 130-132	731	1.42
1-H 5-W 138-140	739	2.29

CHAPTER 4: DISCUSSION

The primary goal of this study was to establish the first continuous late Pleistocene paleoclimate record for the Southwest African Margin using the terrigenous component of marine sediment. Multiple proxies were used including weight percent sand, $\%CaCO_3$, color reflectance, %TOC, C/N, median grain-size, grain-size distribution, and clay mineralogy to constrain the climate in the region during the late Pleistocene. Although oxygen isotope data only provides ages to 122.9 ky, correlation of biostratigraphic data (Wefer et al., 1998) with the SPECMAP Oxygen Isotope Curve (Imbrie et al., 1984) allows for a rough age estimation and interpretation of glacial/interglacial cycles for the study site to MIS 8 (Table 4.1). The main focus, however, is from MIS 1 through MIS 5, since this is the extent of the clay data. Additionally, the relationship between SPECMAP and weight percent sand extends the correlation and allows for the interpretation of glacial/interglacial cycles further down in the core.

TABLE 4.1 Characteristics of MIS 1 – 8

MIS	Glacial/ Interglacial	Base Depth (cm bsf)	Age (ky)	Weight % Sand	% $CaCO_3$	Color Reflectance	%TOC	C/N	Grain Size Distribution	Median Grain Size
1	Interglacial	43	11	Lower	Avg. 72.55 Lower	Lower	Higher	~ 10 Mixed marine and terrigenous	Eolian	< 4 μm
2	Glacial	175	36	High peak	Avg. 77.68 High peak	Moderate	Higher	Large amplitude > 14, mixed marine/terrigenous one point < 8	Hemipelagic	Peak ~ 13 μm
3	Interglacial	193	56	Lower	Avg. 78.45 Lower	Higher	Lower	< 8 Marine	Hemipelagic	< 4 μm
4	Glacial	223	76.8	Higher	Avg. 79.09 High peak	Higher	Low peak	< 8 Marine	Hemipelagic	< 4 μm
5	Interglacial	425	At least 90 due to *E. huxleyi* acme datum at 529 cm bsf	Lower with single peak	Avg. 63.34 Lower	Low peak	Higher with 2 peaks >2	~ 8 Marine with single terrigenous peak	Hemipelagic	Mostly < 4 μm, 4 peaks 6 - 13 μm
6	Glacial	619	Younger than 260 due to *E. huxleyi* FO (610 - 910 cm bsf)	Higher	Avg. 71.48 Higher	Higher	Lower	< 8 Marine with 2 points of excess N	Hemipelagic	< 4 μm, 1 peak ~ 8 μm
7	Interglacial	734	Younger than 260 due to *E. huxleyi* FO (610 - 910 cm bsf)	Lower	Avg. 70.21 Low peak	Low peak	Higher	~ 8 Mixed marine and terrigenous	Hemipelagic	< 4 μm
8	Glacial		Potentially older than 260 due to *E. huxleyi* FO (mid. point 760 cm bsf)	Higher	Avg. 61.18 Moderate	Higher	High peak	< 8 Marine	Hemipelagic	< 4 μm

TABLE 4.1 (continued)

MIS	Glacial/ Interglacial	Base Depth (cm bsf)	Age (ky)	Clay
1	Interglacial	43	11	Illite and smectite rich; Broad source range for both
2	Glacial	175	36	Increased presence of kaolinite; Change of illite source to Angola Basin
3	Interglacial	193	56	Angola Basin source region for illite; some increase in presence of kaolinite
4	Glacial	223	76.8	Dominance by illite and smectite; source region for illite is the Angola Basin
5	Interglacial	425	At least 90 due to *E. huxleyi* acme datum at 529 cm bsf	Dominance by illite and smectite with a broad source region
6	Glacial	619	Younger than 260 due to *E. huxleyi* FO (610 - 910 cm bsf)	No data
7	Interglacial	734	Younger than 260 due to *E. huxleyi* FO (610 - 910 cm bsf)	No data
8	Glacial		Potentially older than 260 due to *E. huxleyi* FO (mid. point 760 cm bsf)	No data

4.0 The Continental Signal

Continental climate is addressed using the Southern Hemisphere solar insolation curve for January (austral summer) at 60ºS (Figure 4.1) and the relationships between that curve and our proxies. During periods of high SH solar insolation, climates are more humid and at periods of lower insolation, climates are more arid due to the migration of the ITCZ. The ITCZ is further south during humid times and further north during more arid times (Figure 1.9).

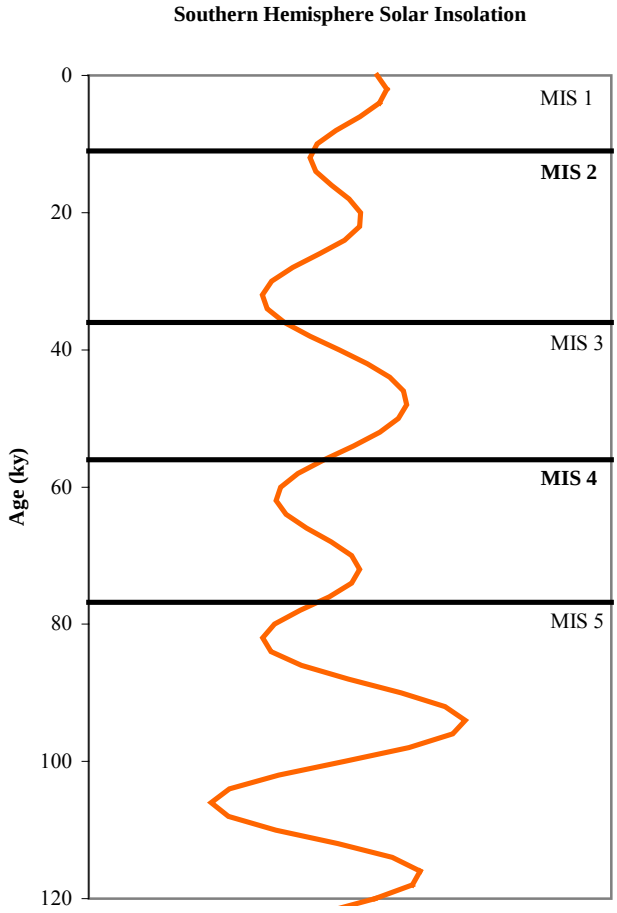

FIGURE 4.1: Southern Hemisphere solar insolation for January, 60ºS. Periods of higher SH solar insolation are to the right and periods of lower SH solar insolation are to the left on this chart.

The proxies that will potentially provide a continental signal include clay mineralogy, C/N, median grain-size, and grain-size distribution. In order to take away the dilution factor when analyzing the data, the mass accumulation rate (MAR) ($g/cm^2/ky$) was taken of all concentration percentages (see Equation 8). The BAR is provided by Christensen and determined by the sedimentation rate from the age-depth plot (Figure 4.2). No relationship is visible between any of the clay MAR data and SH solar insolation (Figure 4.3). This indicates that changes in the clay mineral assemblages found at Site 1085 reflect a marine influence and do not have a dominant continental source. The C/N ratios (Figure 4.4), likewise, show no relationship to SH solar insolation. This indicates that the influx of terrigenous carbon to the study area, during periods of C/N ratios greater than 8, is not governed by SH solar insolation.

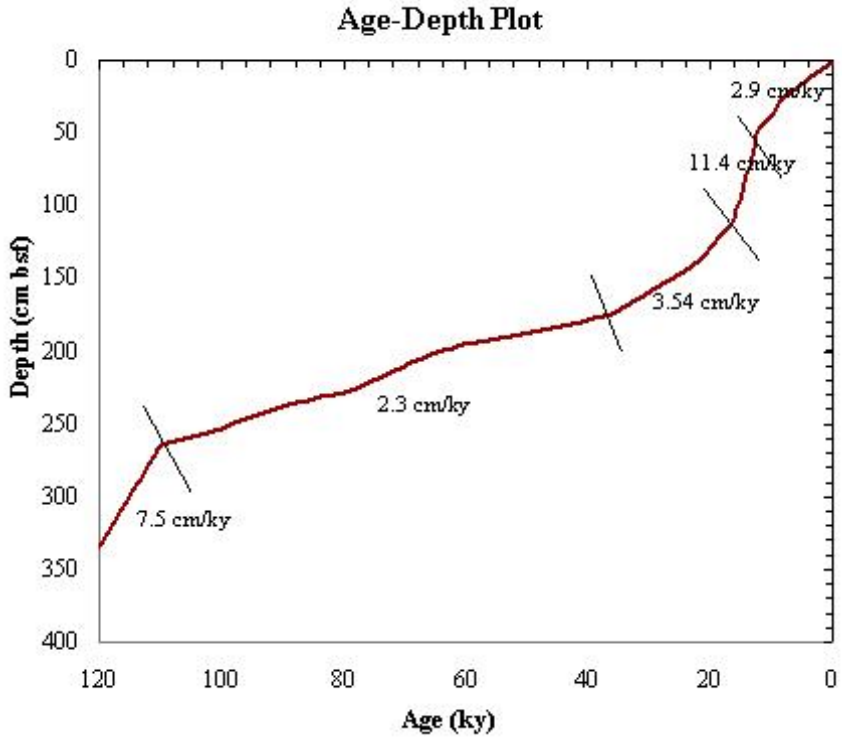

FIGURE 4.2: Age-Depth plot with sedimentation rates (provided by Christensen).

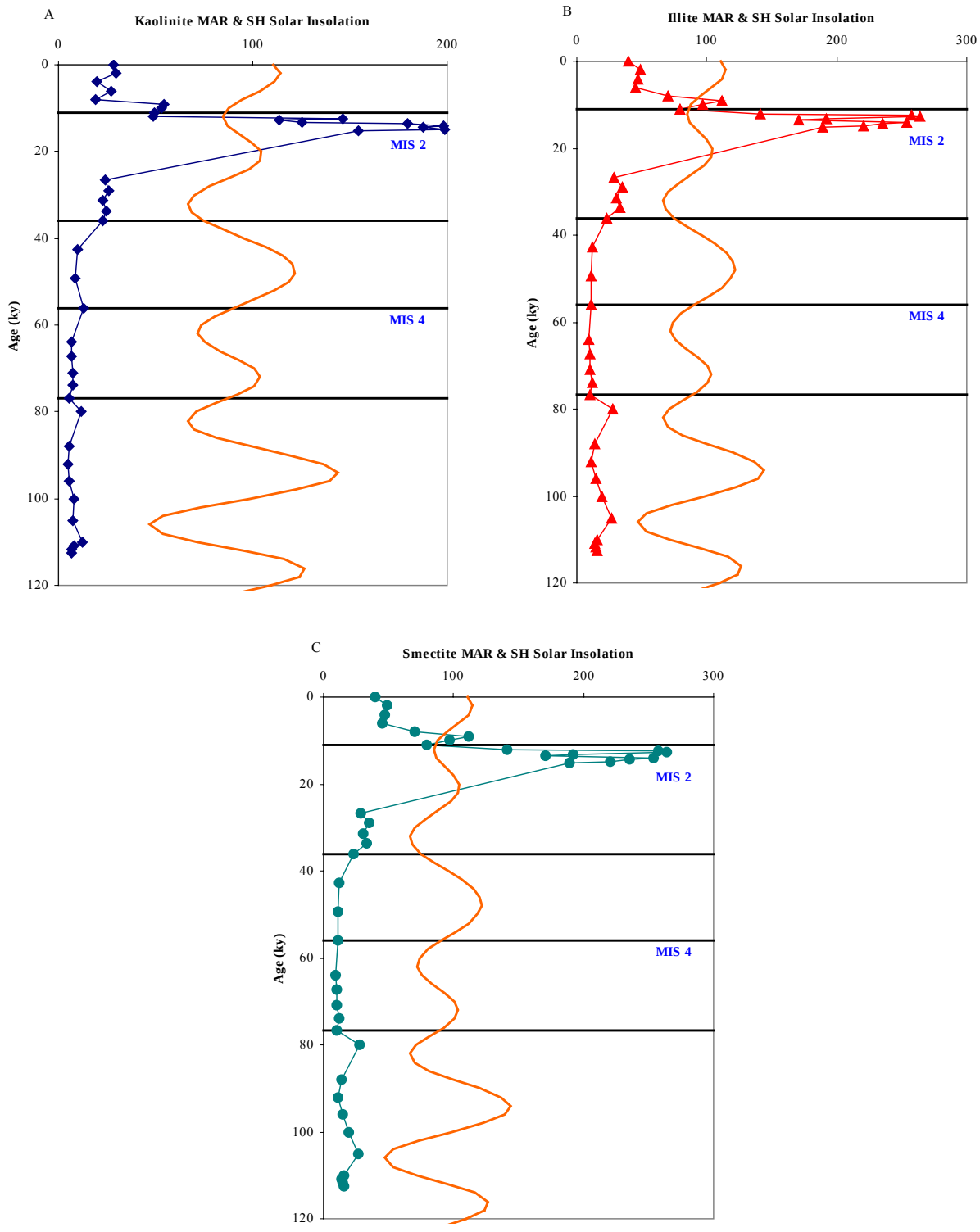

FIGURE 4.3: Clay MAR data for kaolinite (A), illite (B), and smectite (C) and SH solar insolation vs. age.

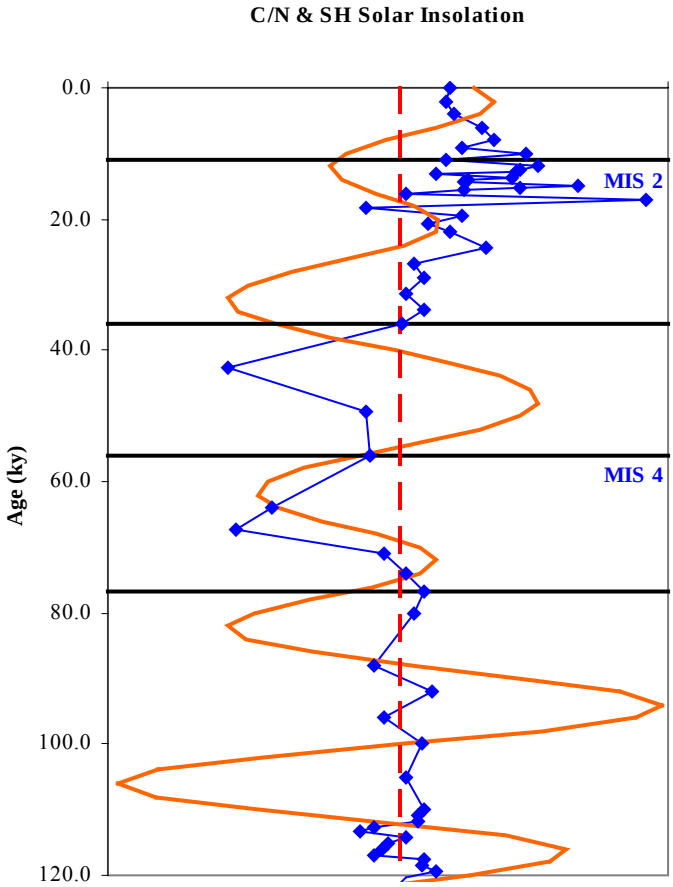

FIGURE 4.4: C/N and SH solar insolation vs. age. SH solar insolation is plotted in orange, C/N ratios are plotted with blue diamonds, and C/N = 8 is plotted as the red dashed line.

Median grain-size and grain-size distribution do exhibit relationships with SH solar insolation at specific intervals of time (Figure 4.5). SH solar insolation and median grain-size have a positive relationship in MIS 4 and 5. During these times, larger grain-sizes are associated with highs in solar insolation and smaller median grain-sizes are associated with lows in insolation. Since times of high insolation are associated with humid periods, this relationship indicates that fluvial strength would have increased in order to transport larger grains to the study site during these humid periods. In MIS 3, the relationship is reversed with a smaller median grain-size associated with the solar insolation high. MIS 2 shows a similar pattern as in MIS 4

and 5, with lower grain-size associated with insolation lows and drier periods and relatively higher grain-sizes associated with insolation highs and wetter periods. The relationship breaks down at the end of MIS 2 and through MIS 1. Although both insolation and median grain-size change throughout MIS 1, there is no longer any correlation between grain-size and SH solar insolation during this stage.

Grain-size distributions also show some correlation to the SH solar insolation curve. In MIS 5 there is an inverse relationship between the two with more arid periods being characterized by increased hemipelagic input to the study area and more humid periods being characterized by increased eolian input to the site. This relationship seems counterintuitive to the relationship seen with median grain-size and insolation, since that relationship indicates more humid conditions. More humid conditions should lead to increased hemipelagic input, however during this stadial, the climate was a bit more arid. There are two periods of low solar insolation during MIS 5 in our section and both of these are characterized by hemipelagic transport. Since MIS 5 is an interglacial period, it is more humid when compared to glacials and that increased humidity adds to hemipelagic transport, even during insolation lows.

The inverse relationship between grain-size distribution and insolation completely breaks down in MIS 4 and 3. MIS 4 and 3 are characterized by a positive correlation between the solar insolation and grain-size distribution curves. During these times, increased hemipelagic transport is associated with highs in solar insolation, indicating more humid conditions that provide increased fluvial input to the study area. Solar insolation lows are associated by peaks in eolian transport and indicate that during more arid conditions, either wind strength increased or fluvial transport decreased in strength. Because there is a dominant pattern of hemipelagic transport at this site in MIS 2 through 5, the peaks in eolian input indicate a brief increase in

wind strength when there is a positive relationship between grain-size distribution and the solar insolation curve.

In the beginning of MIS 2, the inverse correlation is again present, with more arid conditions associated with hemipelagic input to the study area. This is a similar situation to that seen in late MIS 5, which although part of interglacial MIS 5, has more of a glacial signal where increased aridity due to insolation is associated with hemipelagic transport. Around 20 ky, the relationship breaks down completely and the fluctuation in dominant grain-size distribution does not allow for a correlation between the proxy curve and the SH solar insolation curve. This breakdown comes around the same time as the breakdown in the relationship between median grain-size and solar insolation and is present all the way through MIS 1.

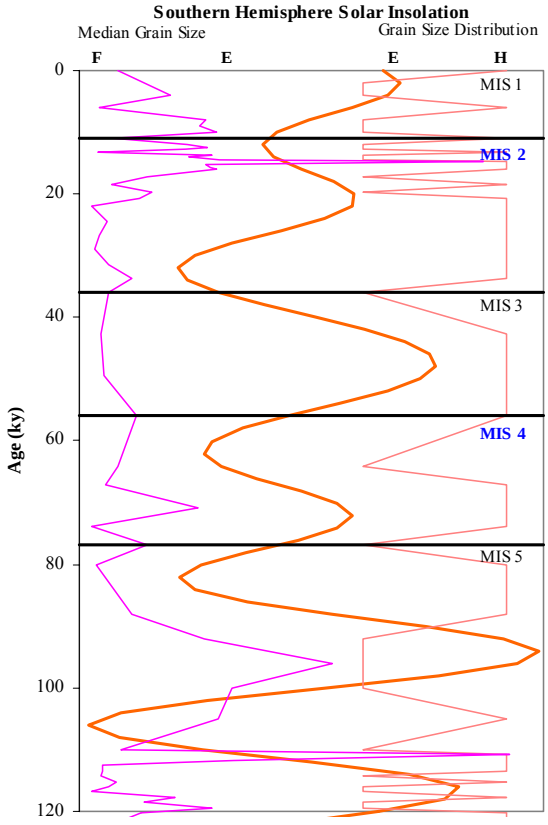

FIGURE 4.5: SH solar insolation for January, 60ºS, median grain-size and grain-size distribution. F indicates fluvial transport, E indicates eolian transport and H indicates hemipelagic transport.

4.1 The Marine Signal

The SPECMAP Oxygen Isotope Curve (Imbrie et al., 1984) is used to determine whether our proxy data provide a marine signal. SPECMAP is a stacked record of ice volume change recorded in the changes of $\delta^{18}O$ of benthic foraminifera. As the oxygen atoms in $CaCO_3$ deposited by marine organisms comes from the ocean water, the $CaCO_3$ tests must record changes in the $\delta^{18}O$ of the seawater over time (Broeker, 1995). During glacial periods, the ocean water is enriched in heavy ^{18}O, giving it a higher $\delta^{18}O$ ratio (MIS 2 and 4 in Figure 4.6). In contrast, interglacial times (MIS 1, 3, and 5 in Figure 4.6) have lower $\delta^{18}O$ values, seen as lows on the SPECMAP curve.

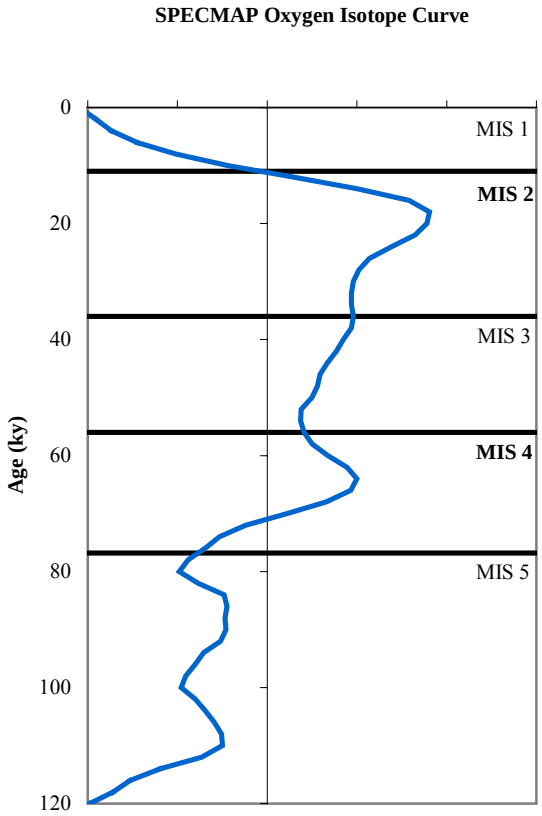

FIGURE 4.6: SPECMAP Oxygen Isotope Curve (Imbrie et al., 1984).

Since there is no continental signal in the clay mineralogy, it is expected that a marine signal will be evident in the clay mineralogical variations as well as the productivity, preservation/dissolution, and dilution proxies of MAR_{sand}, MAR_{CaCO3}, C/N ratios, and MAR_{TOC}. It may also be possible to see evidence of a correlation of median grain-size and grain-size distribution and SPECMAP, which would indicate that the signal evident in those proxy records is more complex than simply a continental signal.

MIS 2 is characterized by a pulse of increased kaolinite just prior to T1 (the boundary between MIS 2 and 1), closely associated with the peak glacial in MIS 2 (see Figure 4.6 and Figure 4.7). Potential sources for this kaolinite are (Figure 4.8): 1) the African continent; 2) transport from ridges and/or spreading centers in the Southern Atlantic (Petschick et al., 1996); 3) transport via the Agulhas Current (Rau et al., 2002); or 4) transport from the Angola Basin (Petschick et al., 1996). Dupont et al. (2003) provide evidence discarding the continent of Africa as a potential source of kaolinite during MIS 2. During glacial stages, Southern Africa becomes more arid, thereby reducing kaolinite production and keeping the continent from supplying kaolinite to the study area (Dupont et al., 2003). Transport from ridges and/or spreading centers in the Southern Atlantic would indeed bring in relatively large quantities of kaolinite to the Southern Cape Basin, however the clay mineral assemblages would show evidence of chlorite as well (Petschick et al., 1996). On an X-ray diffractogram (see Appendix for XRD patterns), chlorite will have a 14 to 14.4Å peak (Moore and Reynolds, 1997) that will be present on the pattern even with solvation in ethylene glycol and heating to 550ºC. Since such a peak is not found in the XRD patterns for the 40 samples analyzed, absence of chlorite is presumed. Because of this, transport of reworked and resuspended clays from the Southern Atlantic followed by deposition in the Cape Basin is not considered the source of this kaolinite influx.

Kaolinite can be transported via the Agulhas Current from the Indian Ocean (Rau et al., 2002). As previously stated, the Agulhas Current leakage has not been cut off for the past 450 ky. If the Agulhas were the main source of kaolinite to the Southern Cape Basin, it is expected that there would be relatively constant concentrations of this mineral in all analyzed samples as opposed to a single pulse during MIS 2. Because Agulhas Current leakage has not been cut off, it is assumed that some of the background kaolinite is transported from the Indian Ocean, however the pulse would have to come from elsewhere.

The final possible source for the pulse of kaolinite seen during MIS 2 is the Angola Basin. The Angola Counter Current runs along the shelf bringing water and sediment from the Angola Basin poleward towards the Cape Basin (Figure 1.2) (Wefer et al., 1998). As sea level falls during glacial periods, sediment previously deposited along the shelf can become exposed to both eolian and fluvial transport mechanisms. Kaolinite can become resuspended, either in winds or river water, and transported to the study area where it is redeposited during glacial periods. Because Site 1085 is off of a very broad shelf (Figure 1.7), the Angola Counter Current can transport material farther and spread out along the shelf, aiding in transport of the kaolinite to the study area. Further evidence for the source of kaolinite comes from the other clay minerals present, namely, illite (Figure 4.7). The intensity ratio (IR) of the 5Å (002) and 10Å (001) peaks of illite can constrain source (Petschick et al., 1996) and in this instance, there is a change in source around T1 (Figure 3.4 B). In MIS 1 and prior to MIS 2, illite has a very broad source, based solely on IR. In MIS 2, however, the IR constrains the source of the illite to a fairly small area in the Angola Basin (Petschick et al., 1996). Transport of illite to the Cape Basin follows the model previously discussed with respect to kaolinite, i.e., transport by the

poleward Angola Counter Current along the shelf. The clay mineralogical assemblages found at Site 1085, therefore, provide a marine signal of origin and transport for the late Pleistocene.

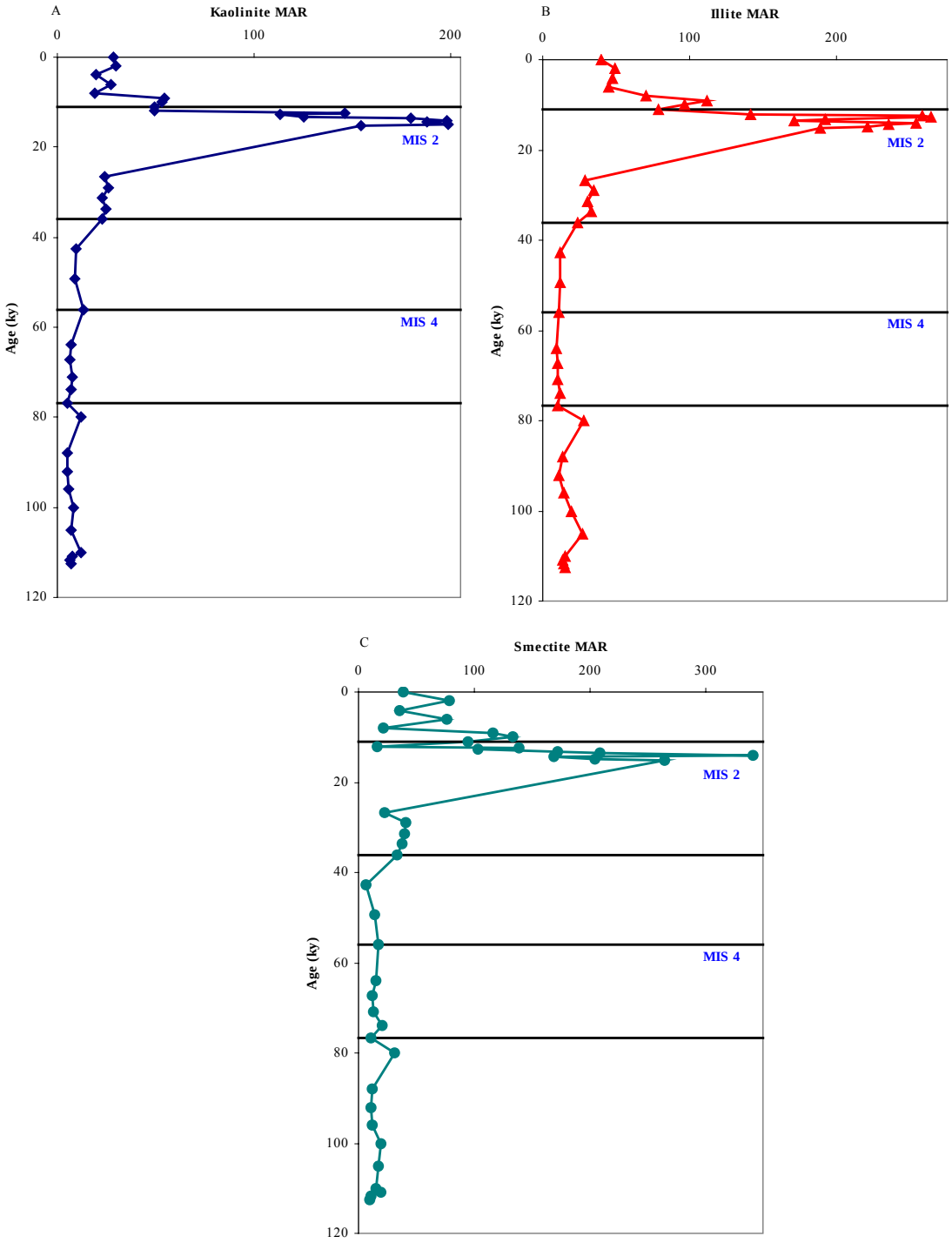

FIGURE 4.7: Clay MAR vs. Age (ky). (A) kaolinite, (B) illite, (C) smectite.

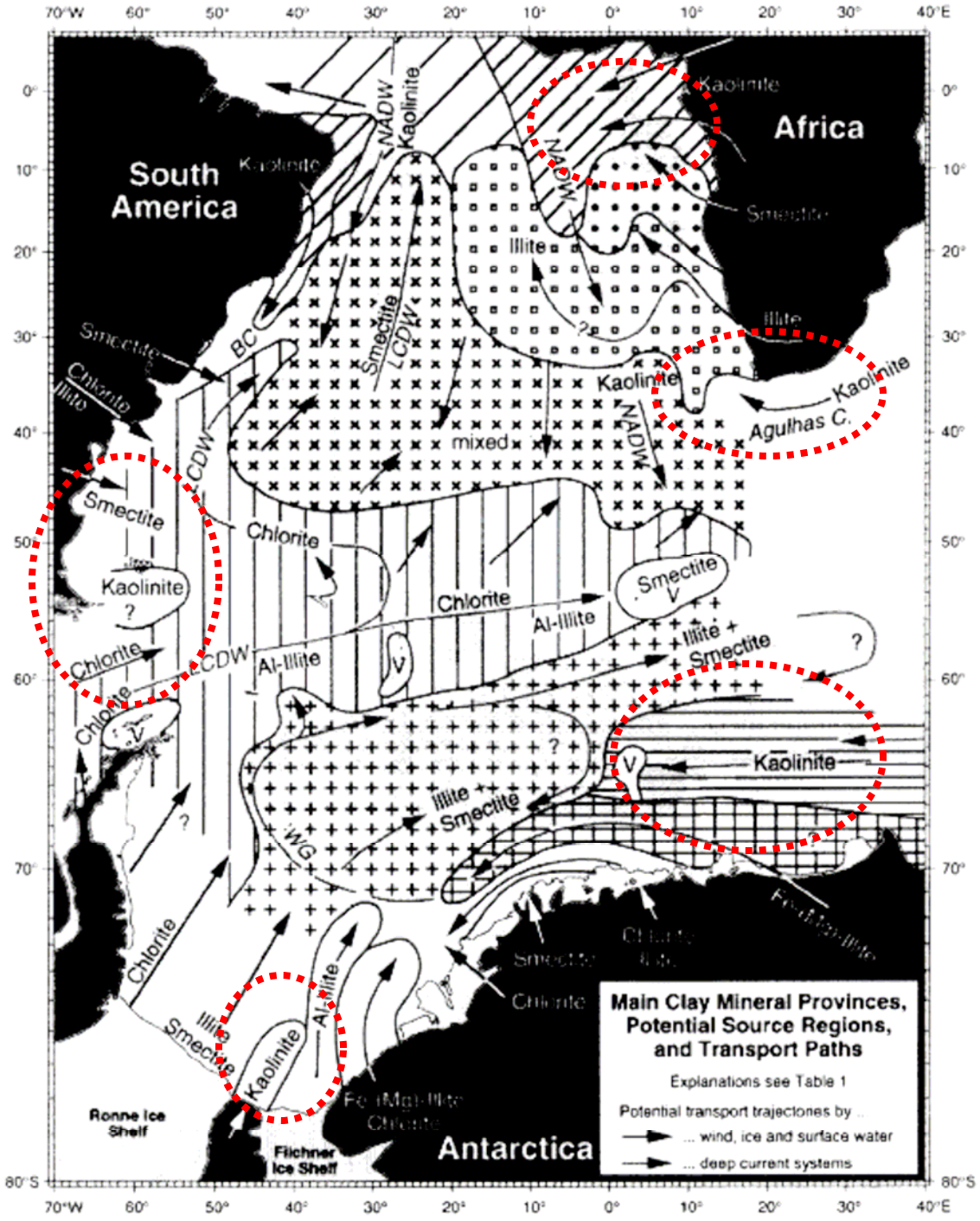

FIGURE 4.8: Potential sources of kaolinite, circled in red (from Petschick et al., 1996).

Glacial MIS 2 is characterized by higher weight percent sand, higher MAR_{CaCO3}, moderate color reflectance, higher MAR_{TOC} and a mixed organic carbon source (C/N > 8; see Figure 3.10). The increased weight percent sand could be caused by a couple of factors including a pulse of cold surface water creating higher productivity at the surface or increased preservation due to an increase in AAIW and/or rapid burial (sedimentation) rate (Figure 4.2). Rau et al. (2002) suggests a reduction in NADW during glacial periods and enhanced productivity as seen by the inverse correlation between $\delta^{13}C$ and MAR_{sand}. During glacial periods, cold subantarctic surface waters reach a northerly extent of 36ºS, as seen by the increase in the abundance of planktonic cold-water foraminifera (Rau et al., 2002). Should this advancement of cold subantarctic surface water extend to the Southern Cape Basin study area, it could provide a mechanism for the high peak in sand accumulation, and therefore MAR_{CaCO3} and color reflectance, seen at Site 1085. However, since 450 ky, there is no evidence that the Agulhas Current leakage has been cut off (Rau et al., 2002), so the increase in weight percent sand is not due to a pulse of cold subantarctic surface water reaching all the way into the Southern Cape Basin.

The other possibility for the observed increase in sand accumulation is an increase in preservation and sedimentation rate (Rau et al., 2002). During MIS 2, at the study site, both increased sedimentation rate (11.4cm/ky) (Figure 4.2) and less dissolution of the $CaCO_3$ are visible (Figures 4.9 and 4.10). In both figures, the proxy and SPECMAP follow similar patterns, indicating a marine control on sand and $CaCO_3$ accumulation. The cause of increased sand and $CaCO_3$ accumulation is increased AAIW during glacial MIS 2, in contrast to the greater dissolution caused by older NADW during interglacial MIS 1. MIS 4 and late MIS 5 show more of an inverse relationship between SPECMAP and the accumulation rates of sand and

$CaCO_3$. It is possible for increased sand and $CaCO_3$ accumulation during interglacials due to a more vigorous Benguela Upwelling System and therefore, increased surface productivity (Jahn et al., 2003). During times of increased NADW, there should be greater dissolution of $CaCO_3$, however, due to increased surface productivity, it is possible for there to be an associated increase in sand and $CaCO_3$ accumulation with a much lower dissolution signature simply because of the increase in material.

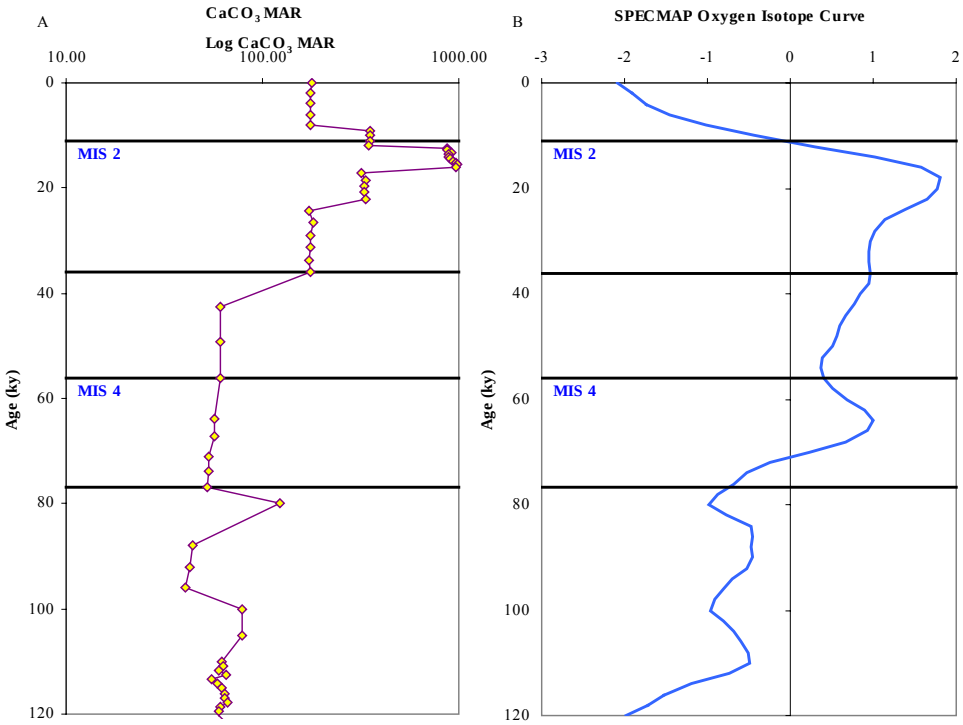

FIGURE 4.9: MAR_{CaCO3} (A) and SPECMAP Oxygen Isotope Curve (B).

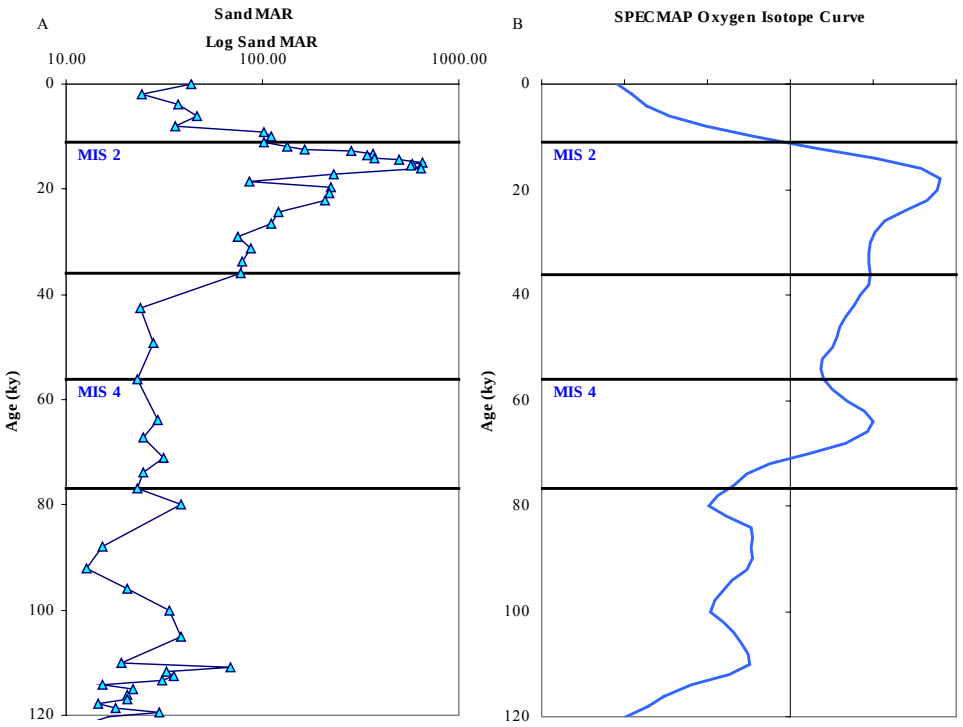

FIGURE 4.10: MAR_{sand} (A) and SPECMAP Oxygen Isotope Curve (B).

The final proxy that could show a marine signal is the accumulation of TOC (Figure 4.11). The only real relationship between SPECMAP and the MAR_{TOC} curves is during MIS 2, where there is a peak in the accumulation of TOC at the same point as the peak of the glacial stage. This peak in MAR_{TOC} coincident with the peak glacial indicates an increase in primary surface productivity just prior to T1.

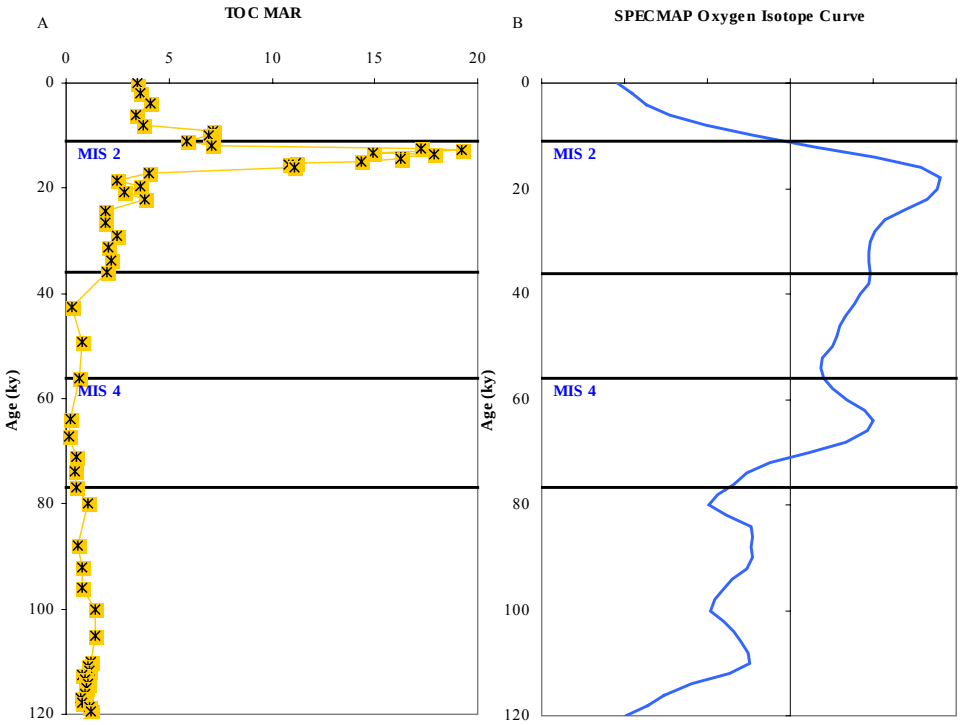

FIGURE 4.11: MAR_{TOC} (A) and SPECMAP Oxygen Isotope Curve (B).

4.2 A Combined Signal

Proxies with a marine signal and those with a continental signal all face some breakdown in relationship with either SPECMAP or the SH solar insolation curve at the end of MIS 2 and throughout MIS 1. Figure 4.12 shows these two curves plotted against depth and there is no real relationship between the two until they both reach higher values around 20 ky. The local maximum of the solar insolation curve indicates a more humid climate while the local maximum of the SPECMAP curve indicates cooler, glacial climatic conditions. These two peaks amplify one another and cause the breakdown in the relationships seen prior to that point in time.

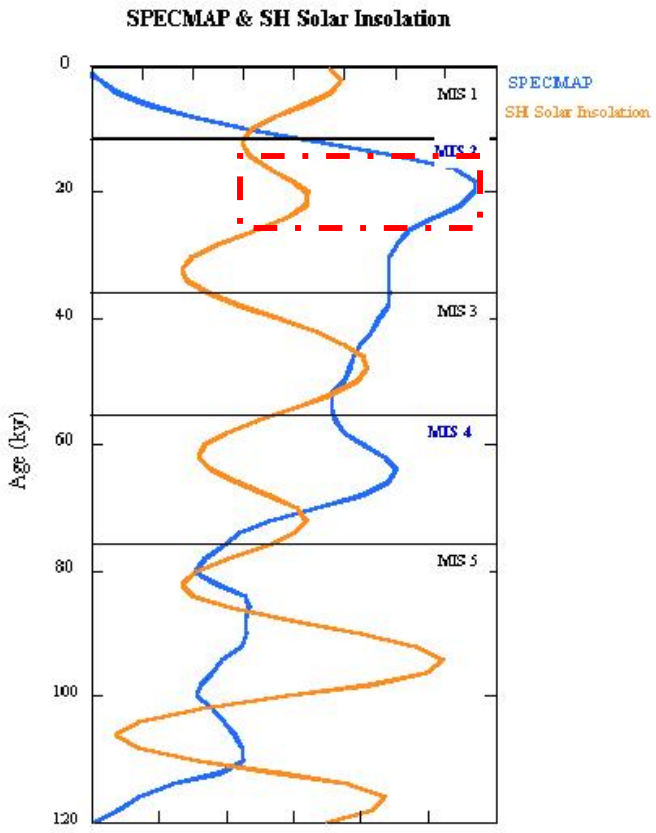

FIGURE 4.12: SPECMAP (blue) and SH solar insolation (orange). The dashed red box indicates coincident peaks between the SPECMAP and SH solar insolation curves.

Median grain-size and grain-size distribution for the study area do not follow the same pattern seen in the Northern Benguela system by Jahn et al. (2003). In that study, dust contribution from 300 ky to the present was found to follow Northern Hemisphere glacial/interglacial cycles. This is a different signal from the Southern Cape Basin at Site 1085 which shows dominant hemipelagic input, based on grain-size distribution, prior to MIS 1 and no relationship with glacial/interglacial cycles. Pulses of larger grain-sizes are found in both glacial MIS 2 and interglacial MIS 5 indicating that there are different mechanisms at work transporting larger material to the study area at different periods throughout geologic time. If the Southern Cape Basin sediment showed a similar cycle to that of the Northern Benguela system, dust input would mimic the SPECMAP (Imbrie et al., 1984) curve. Since this does not occur, there must be another driving mechanism for eolian input to the study area. This is a complex system, not simply controlled by the migration of the APF (Rau et al., 2002).

CHAPTER 5: CONCLUSIONS

The following are the conclusions resulting from the research conducted on the upper 7.2 m of ODP Leg 175 Site 1085B core:

1. Clay mineralogy does not provide a continental signal at Site 1085 for the late Pleistocene.

2. Clay mineralogy does provide a marine signal in the form of source region and probable transport to Site 1085. Phyllosilicate clays are transported poleward along the shelf via the Angola Counter Current. During glacial intervals sediments are exposed to eolian and fluvial transport mechanisms that can transport the kaolinite and illite to the Southern Cape Basin.

3. Prior to MIS 2, there is a continental signal seen in the grain-size data, however there is no relationship between the grain-size data and the productivity proxies for the late Pleistocene.

4. MAR_{CaCO3} and MAR_{sand} provide evidence for increased preservation/decreased dissolution during MIS 2, possibly due to increased AAIW influence at the study site.

5. MAR_{TOC} correlate with MIS 2 and 1 and provide evidence of increased primary productivity during MIS 2.

6. There is no simple relationship between C/N values and glacial/interglacial cycles for the late Pleistocene, indicating that Northern Hemisphere glaciation may not drive the carbon source to Site 1085.

7. Site 1085 is a dynamic system with paleoclimate signals indicating both continental and marine control. These different controls indicate a very complex climatic system for Southern Africa during the late Pleistocene.

REFERENCES

Berger, W.H., Wefer, G., 1996. Expeditions into the past: Paleoceanographic studies in the South Atlantic. In: Wefer, G., Berger, W.H., Siedler, G., Webb, D.J., (Eds.), The South Atlantic: Present and Past Circulation. Springer-Verlag, Berlin, pp. 363-410.

Berger, W.H., Wefer, G., Richter, C., Lang, C.B., Giraudeau, J., Hermelin, O., and Shipboard Scientific Party, 1998. The Angola-Benguela Upwelling System: Paleoceanographic synthesis of shipboard results from Leg 175. In: *Proceedings of the Ocean Drilling Program, Initial Reports*, Vol. 175.

Berger, W.H., Lange, C.B., and Wefer, G., 2002. Upwelling history of the Benguela-Namibia system: a synthesis of Leg 175 results. In Wefer, G., Berger, W.H., Richter, C. (Eds.), Proc. ODP Sci. Results 175, 1-103 [Online].

Broeker, W.S., 1995. *The Glacial World According to Wally*. New York: Eldigio Press.

Charnook, H., 1996. The Atmosphere and the Ocean. In: *Oceanography, an Illustrated Guide*, edited by C.P. Summerhayes and S.A. Thorpe. New York: John Wiley & Sons.

deMenocal, P., 1995. Plio-Pleistocene African Climate. Science. 270, 53-59.

Diekmann, B., Kuhn, G., Mackensen, A., Petschick, R., Fütterer, D.K., Gersonde, R., Rühlemann, C., and Niebler, H.-S., 1999. Kaolinite and Chlorite as Tracers of Modern and Late Quaternary Deep Water Circulation in the South Atlantic and the Adjoining Southern Ocean. In: *Uses of Proxies in Paleoceanography: Examples from the South Atlantic*, edited by G. Fischer and G. Wefer. Berlin: Springer-Verlag, pp 285-313.

Diester-Haass, L., Meyers, P.A., Vidal, L., 2002. The late Miocene onset of high productivity in the Benguela Current upwelling system as part of a global pattern. Marine Geology. 180, 87-103.

Dupont, L.M. and Wyputta, U., 2003. Reconstructing pathways of Aeolian pollen transport to the marine sediments along the coastline of SW Africa. Quaternary Science Reviews. 22, 157-174.

Holmgren, K., Lee-Thorp, J.A., Cooper, G.R.J., Lundblad, K., Partridge, T.C., Scott, L., Sithaldeen, R., Talma, A.S., Tyson, P.D., 2003. Persistent millennial-scale climatic variability over the past 25,000 years in Southern Africa. Quaternary Science Reviews. 22, 2311-2326.

Hovan, S.A. and Rea, D.K., 1992. The Cenozoic record of continental mineral deposition on Broken and Ninetyeast Ridges, Indian Ocean: Southern African aridity and sediment delivery from the Himalayas. Paleoceanography. 7, 833-860.

Imbrie, J., Hays, J.D., Martinson, D.G., McIntyre, A., Mix, A.C., Morley, J.J., Pisias, N.G., Prell, W.L., and Shackleton, N.J., 1984. The orbital theory of Pleistocene climate: support from a revised chronology of the marine d18O record. In Berger, A., Imbrie, J., Hays, J., Kukla, G., Saltzman, B. (eds.), Milankovitch and Climate, Understanding the Response to Astronomical Forcing, NATO Advanced Science Institute Series. D. Reidel Publishing Company, Dordrecht, p. 510.

Jackson, M.L., 1979, Soil Chemical Analysis -- Advanced Course, 2nd edition: M.L. Jackson, p. 34-45.

Joseph, L.H., Rea, D.K., and van der Pluijm, B.A., 1998. Use of grain-size and magnetic fabric analyses to distinguish among depositional environments. Paleoceanography. 13, 491-501.

Jahn, B., Donner, B., Müller, P.J., Röhl, U., Schneider, R.R., Wefer, G., 2003. Pleistocene variations in dust input and marine productivity in the northern Benguela Current: Evidence of evolution of global glacial-interglacial cycles. Palaeogeography, Palaeoclimatology, Palaeoecology. 193, 515-533.

Little, M.G., Schneider, R.R., Kroon, D., Price, B., Bickert, T., Wefer, G., 1997. Rapid palaeoceanographic changes in the Benguela Upwelling System for the last 160,000 years as indicated by abundances of planktonic foraminifera. Palaeogeography, Palaeoclimatology, Palaeoecology. 130, 135-161.

Meyers, P.A., 1994. Preservation of elemental and isotopic source identification of sedimentary organic matter. Chemical Geology. 114, 289-302.

Meyers, P.A., 1997. Organic geochemical proxies of paleoceanographic, paleolimnologic, and paleoclimatic processes. Organic Geochemistry. 27, 213-250.

Micromeritics Products, 2002. Sedigraph analysis techniques. www.micrometirics.com.

Moore, D.M. and Reynolds, R.C., 1997, X-ray diffraction and the identification and analysis of clay minerals: New York, Oxford University Press, 332 p.

Murray, R.W., Christensen, B.A., Kalbas, J.L., and Kryc, K.A., 2002. Pliocene export production and terrigenous provenance of the Southern Cape Basin, southwest African margin. Marine Geology. 180, 133-150.

Partridge, T.C., 1993. Warming phases in Southern Africa during the last 150,000 years: an overview. Palaeogeography, Palaeoclimatology, Palaeoecology, 101, 237-244.

Partridge, T.C., deMenocal, P.B., Lorentz, S.A., Paiker, M.J., Vogel, J.C., 1997. Orbital forcing of climate over South Africa: a 200,000-year rainfall record from the Pretoria Saltpan. Quaternary Science Reviews, 16, 1125-1133.

Petschick, R., Kuhn, G., Gingele, F., 1996. Clay mineral distribution in surface sediments of the South Atlantic: sources, transport, and relation to oceanography. Marine Geology. 130, 203-229.

Petschick, R., 2002. MacDiff 4.2.5 Manual. http://servermac.geolgie.uni-frankfurt.de/Rainer.hmtl

Pye, K., 1989, Processes of fine particle formation, dust source regions, and climate changes. In: *Paleoclimatology and Paleometeorology: Modern and Past Patterns of Global Atmospheric Transport*, edited by M. Leinen and M. Sarnthein, Kluwer Academic, Boston, pp. 3-30.

Rau, A.J., Rogers, J., Lutjeharms, J.R.E., Giraudeau, J., Lee-Thorp, J.A., Chen, M.-T., and Waelbroeck, C., 2002. A 450-kyr record of hydrological conditions on the western Agulhas Bank Slope, south of Africa. Marine Geology. 180, 183-301.

Rea, D.K. and Hovan, S.A., 1995. Grain-size distribution and depositional processes of the mineral component of abyssal sediments: Lessons from the North Pacific. Paleoceanography. 10, 251-258.

Reid, J.L.,1989. On the total geostrophic circulation of the South Atlantic Ocean: Flow patterns, tracers, and transports. Progr. Oceanography. 23: 14-244.

Robinson, R.S., Meyers, P.A., and Murray, R.W., 2002. Geochemical evidence for variations in delivery and deposition of sediment in Pleistocene light-dark color cycles under the Benguela Current Upwelling System. Marine Geology. 180, 249-270.

Russell, J.M., Johnson, T.C., Talbot, M.R., 2003. A 725 yr cycle in the climate of central Africa during the late Holocene. Geology. 31, 677-680.

Seisser, W.G., 1980. Late Miocene origin of the Benguela upwelling system off northern Namibia. Science. 208, 125-146.

Stuut, J.W., Prins, M.A., Schneider, R.R., Weltje, G.J., Jansen, J.H.F., Postma, G., 2002. A 300-kyr record of aridity and wind strength in southwestern Africa: inferences from grain-size distributions of sediments on Walvis Ridge, SE Atlantic. Marine Geology. 180, 221-233.

Sun, D., Bloemendal, J., Rea, D.K., Vandenberghe, J., Jiang, F., An, Z., and Su, R., 2002. Grain-size distribution function of polymodal sediments in hydraulic and Aeolian environments, and numerical partitioning of the sedimentary components. Sedimentary Geology. 152, 263-277.

Twitchell, S.C., Meyers, P.A., and Diester-Haass, L., 2002. Significance of high C/N ratios in organic-carbon-rich Neogene sediments under the Benguela Current upwelling system. Organic Geochemistry. 33, 715-722.

Tyson, P.D., 1999. Atmospheric circulation changes and palaeoclimates of southern Africa. South African Journal of Science. 95, 194-201.

Tyson, P.D. and Preston-Whyte, R.A., 2000, The Weather and Climate of Southern Africa, 2nd edition: Oxford, Oxford University Press.

Tyson, P.D. and Partridge, T.C., 2002. Evolution of Cenozoic Climates. In: *Oxford Monographs on Geology and Geophysics No. 40: The Cenozoic of Southern Africa*, edited by T.C. Partridge and R.R. Maud. New York: Oxford University Press, pp. 371-387.

Vidal, L., Brüchert, U., and Shipboard Scientific Party, 1998. Regional and stratigraphic patterns in color reflectance of sediments from Leg 175. In: *Proceedings of the Ocean Drilling Program, Initial Reports*, Vol. 175.

Wefer, G., Berger, W.H., Bijma, J., Fischer, G., 1999. Clues to Ocean History: A Brief Overview of Proxies, *Use of Proxies in Paleoceanography: Examples from the South Atlantic*, Springer-Verlag Berlin Heidelberg, pp 1-68.

Wefer, G., Berger, W.H., Richter, C., and the Shipboard Scientific Party, 1998. Proceedings of the Ocean Drilling Program, Initial Reports, 175, College Station, TX.

APPENDIX

XRD Pattern Key:

S: Smectite

I: Illite

K: Kaolinite

Q: Quartz

(00*l*): Miller Index

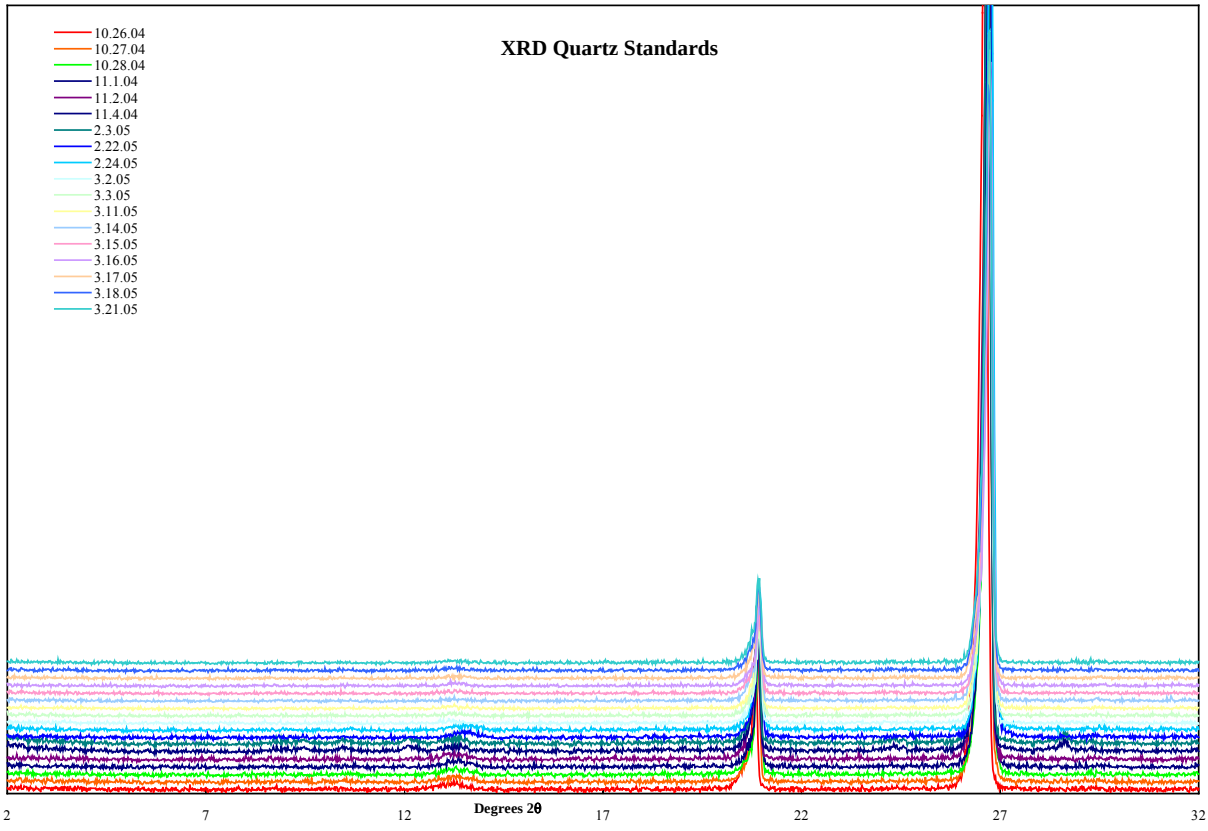
XRD Quartz Standards
10.26.04
10.27.04
10.28.04
11.1.04
11.2.04
11.4.04
2.3.05
2.22.05
2.24.05
3.2.05
3.3.05
3.11.05
3.14.05
3.15.05
3.16.05
3.17.05
3.18.05
3.21.05
2
7
12
17
22
27
32
Degrees 2θ

Sample 1H1W 0-2

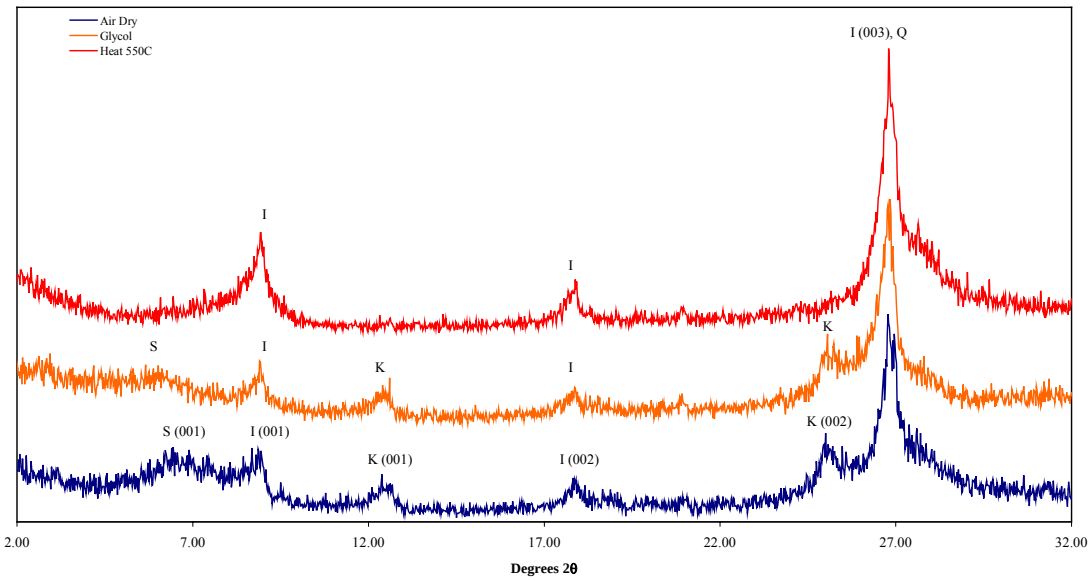

Sample 1H1W 6-8

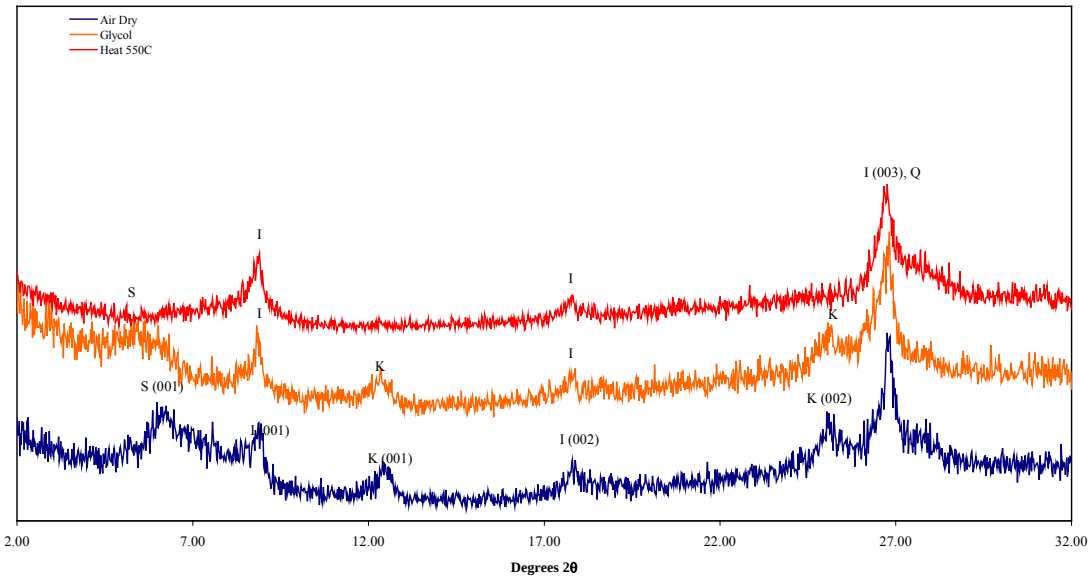

Sample 1H1W 12-14

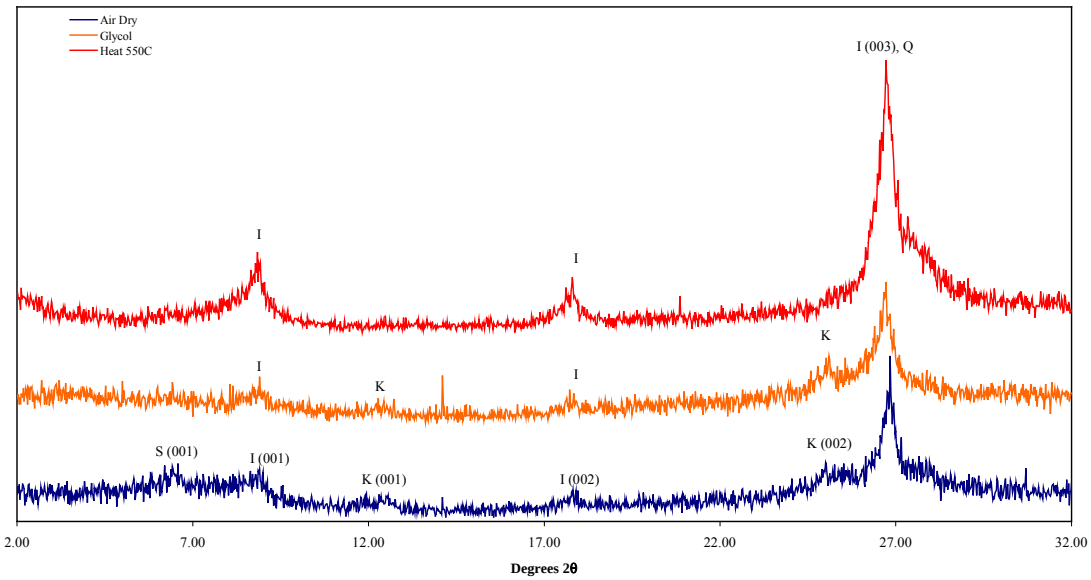

Sample 1H1W 18-20

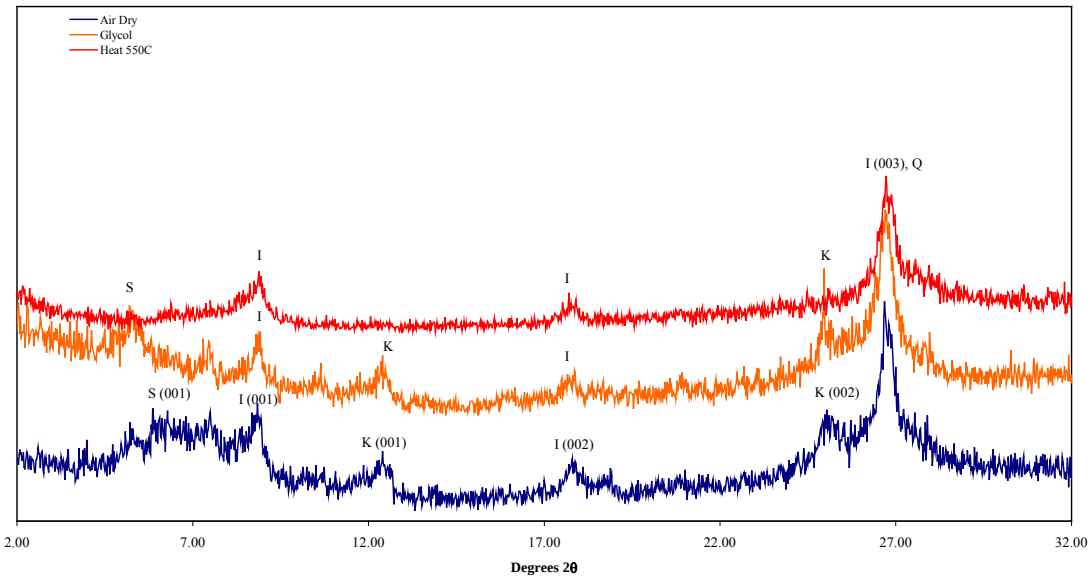

Sample 1H1W 24-26

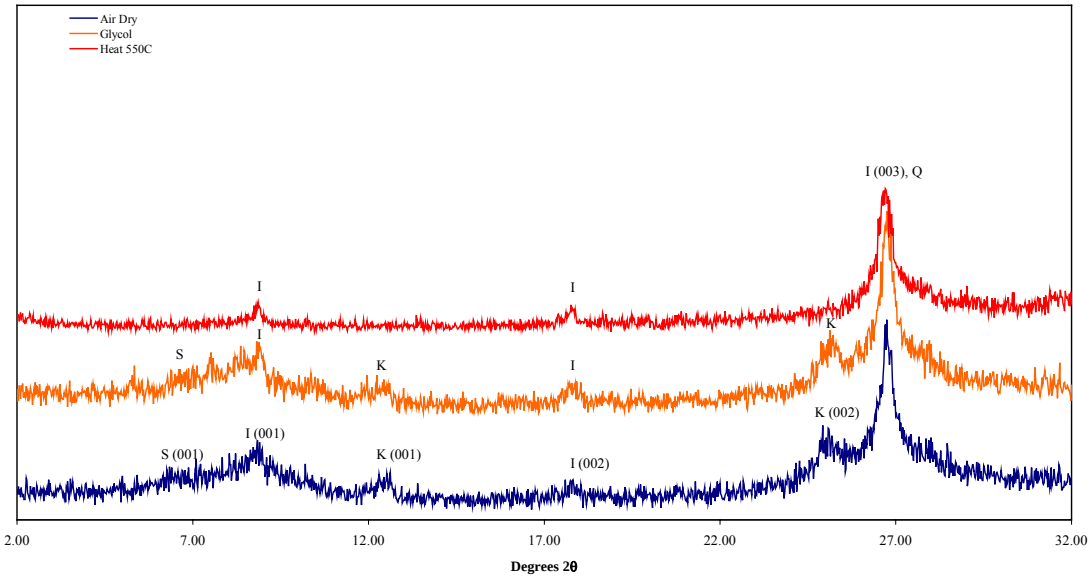

Sample 1H1W 30-32

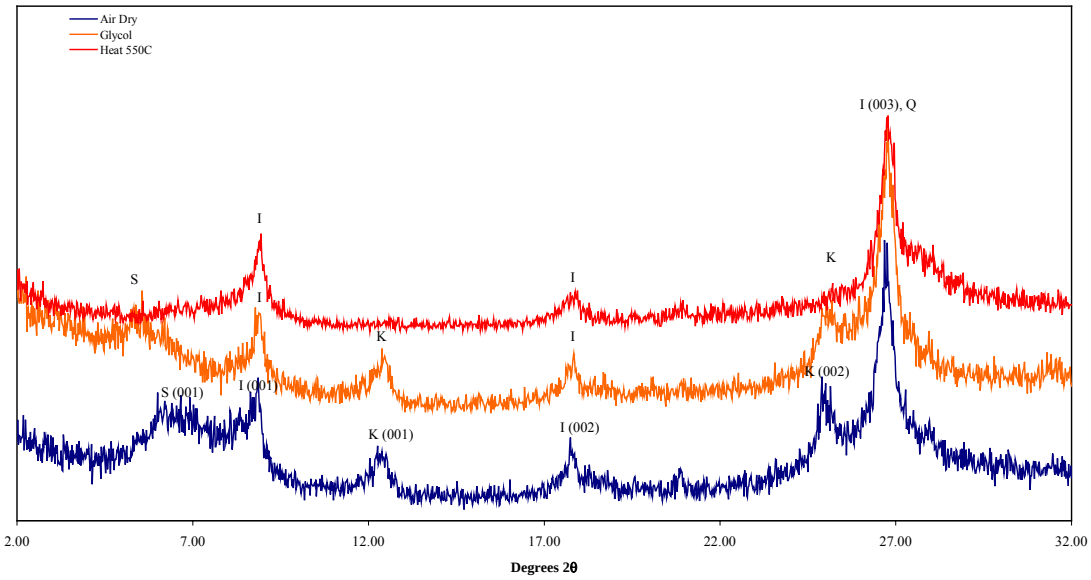

Sample 1H1W 36-38

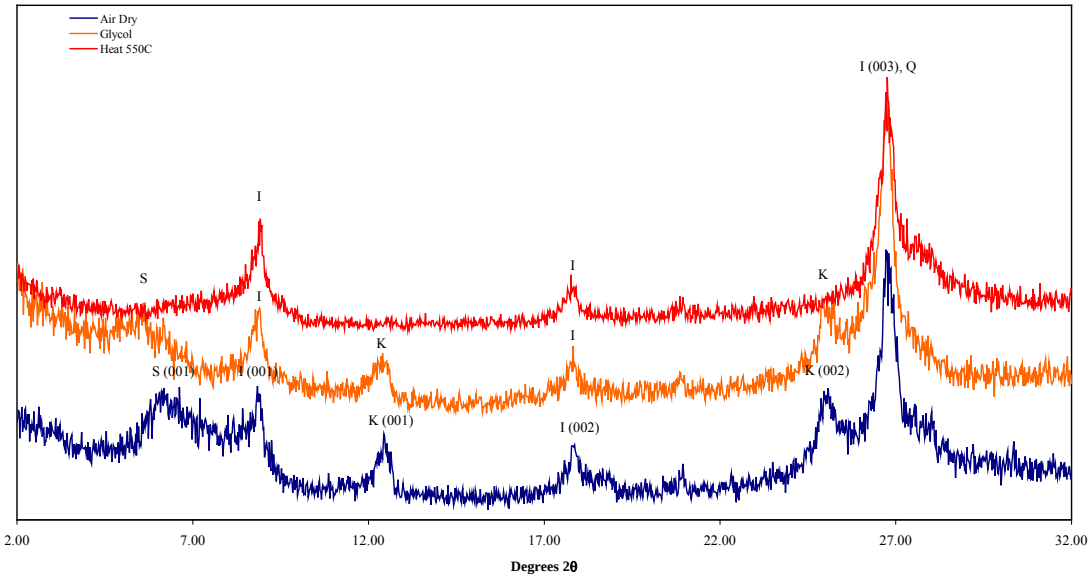

Sample 1H1W 42-44

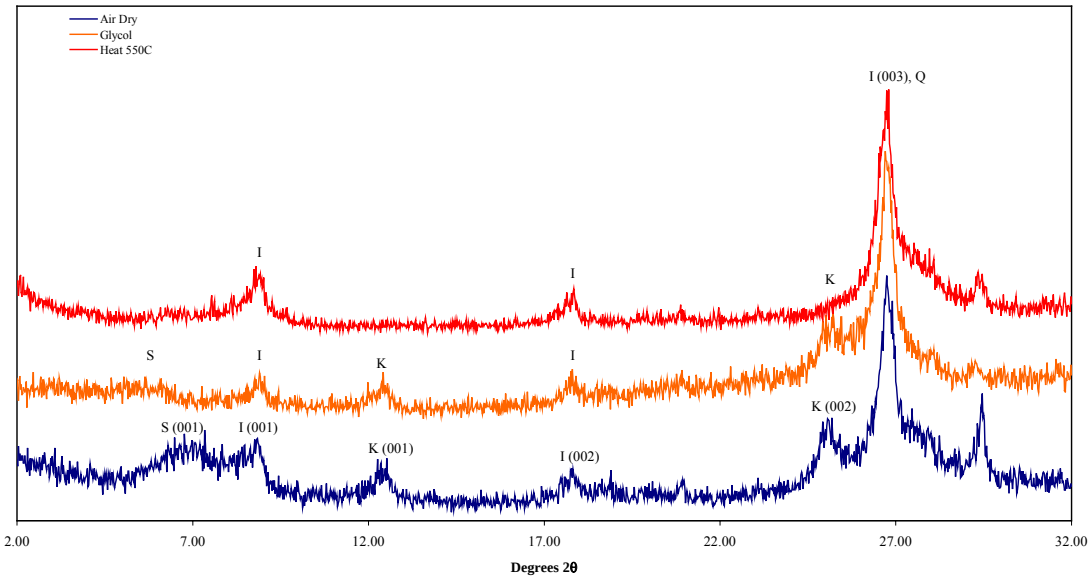

Sample 1H1W 48-50

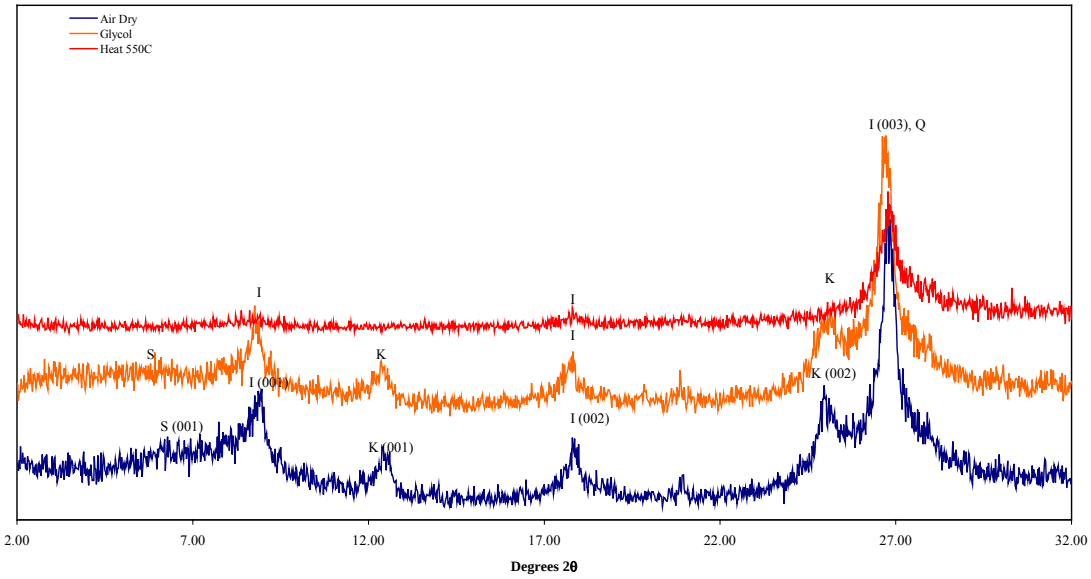

Sample 1H1W 54-56

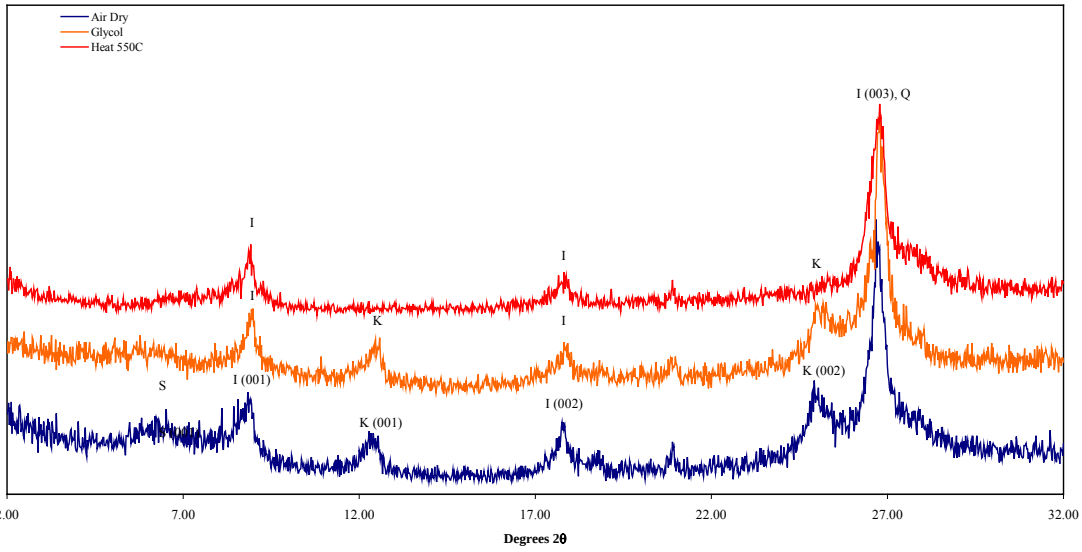

Sample 1H1W 60-62

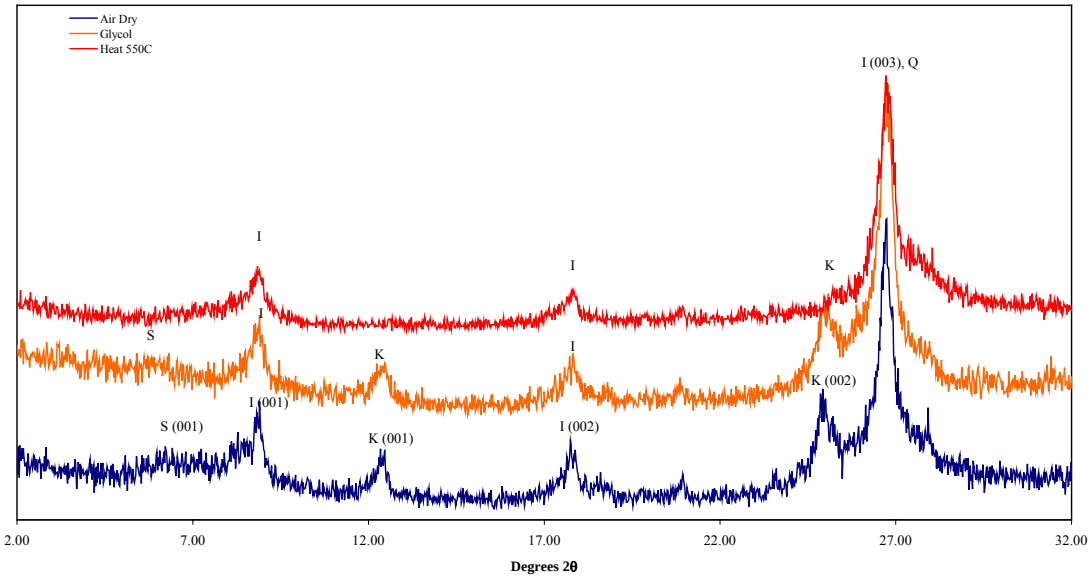

Sample 1H1W 66-68

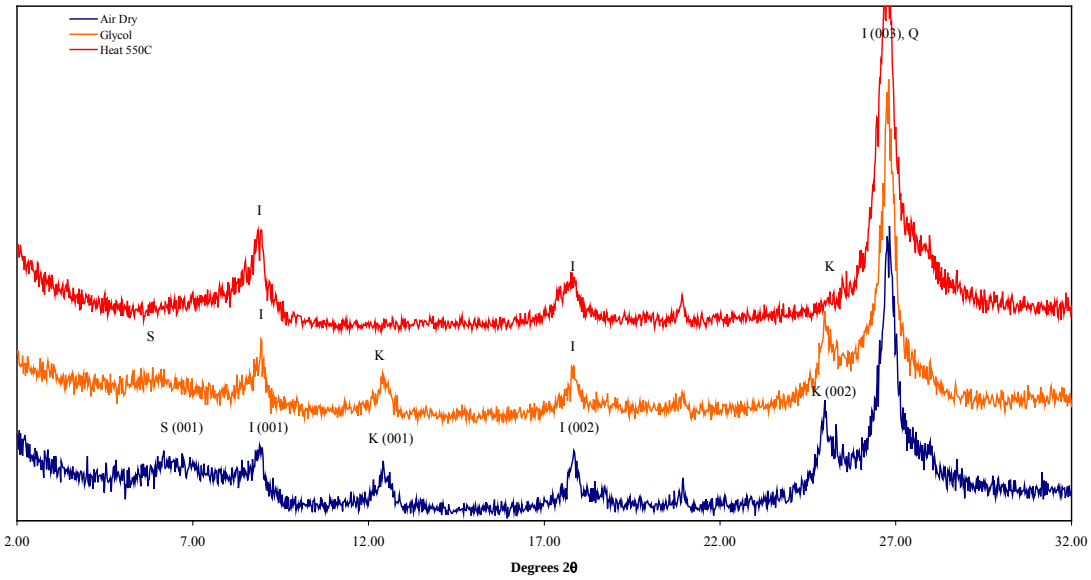

Sample 1H1W 72-74

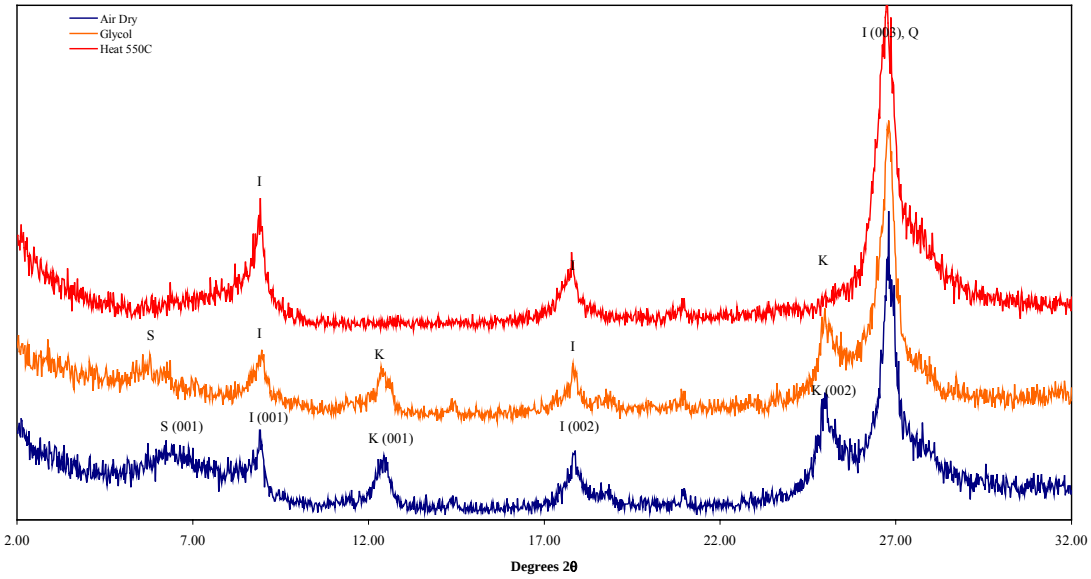

Sample 1H1W 78-80

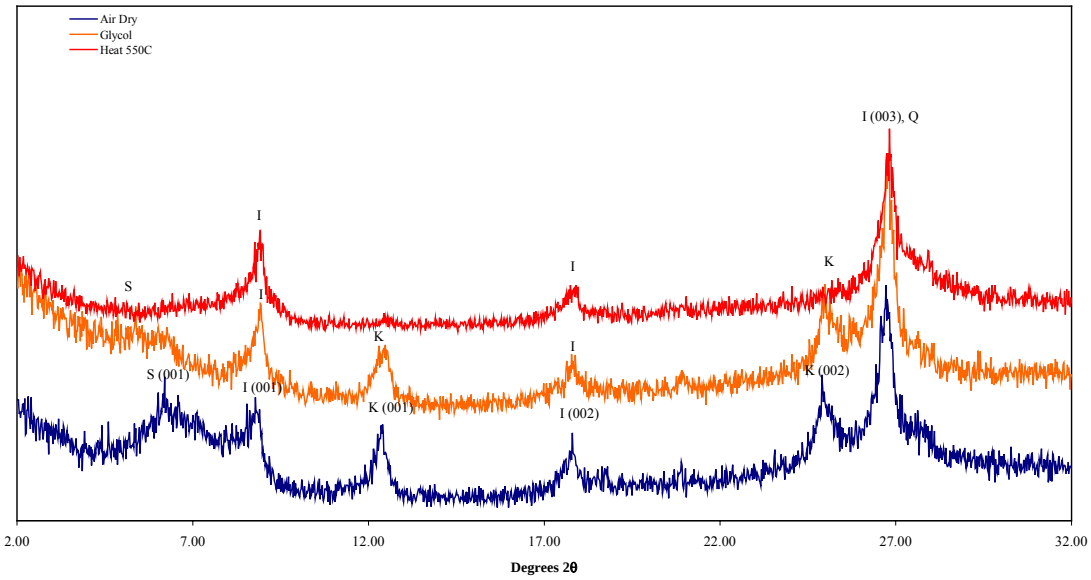

Sample 1H1W 84-86

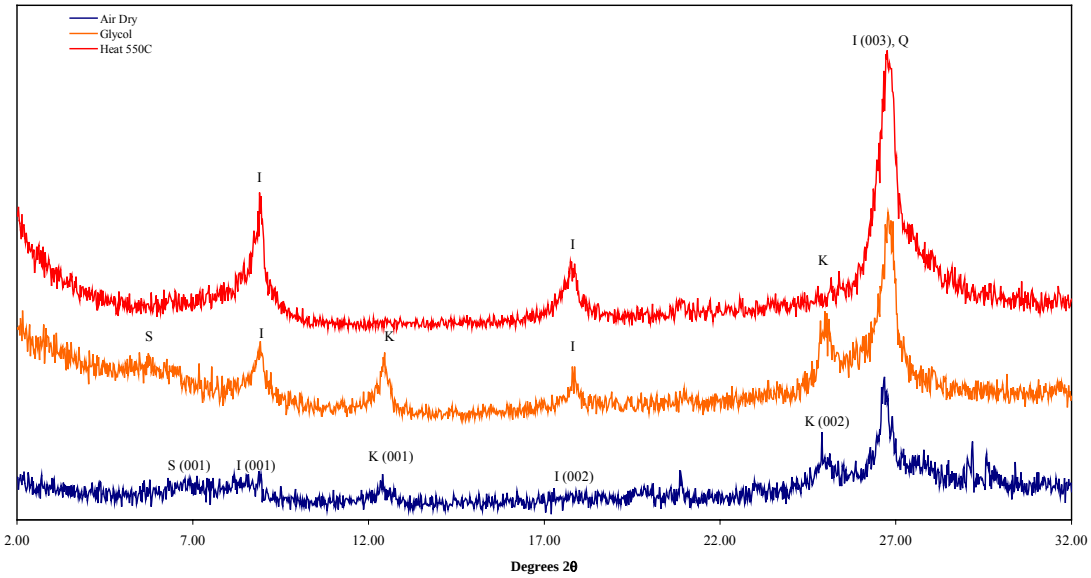

Sample 1H1W 90-92

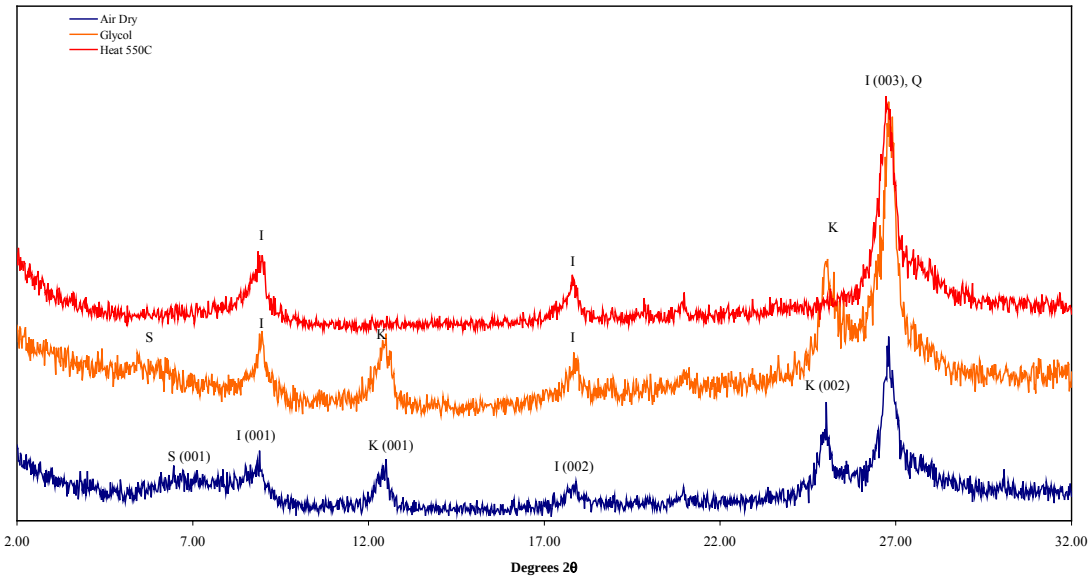

Sample 1H2W 0-2

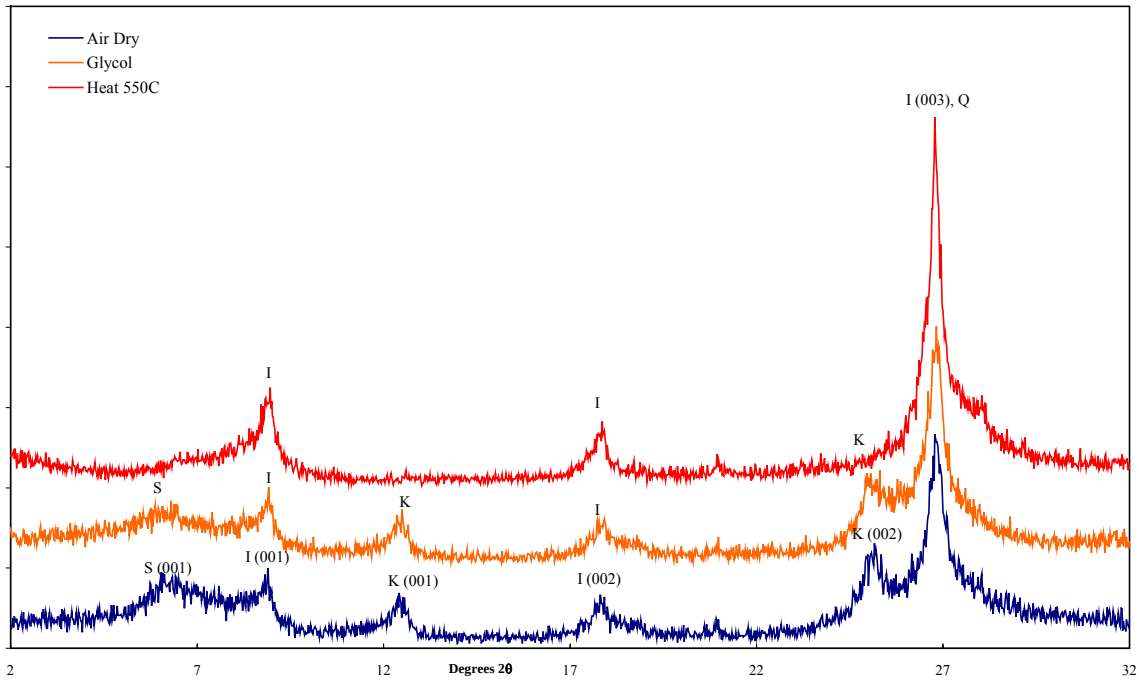

Sample 1H2W 6-8

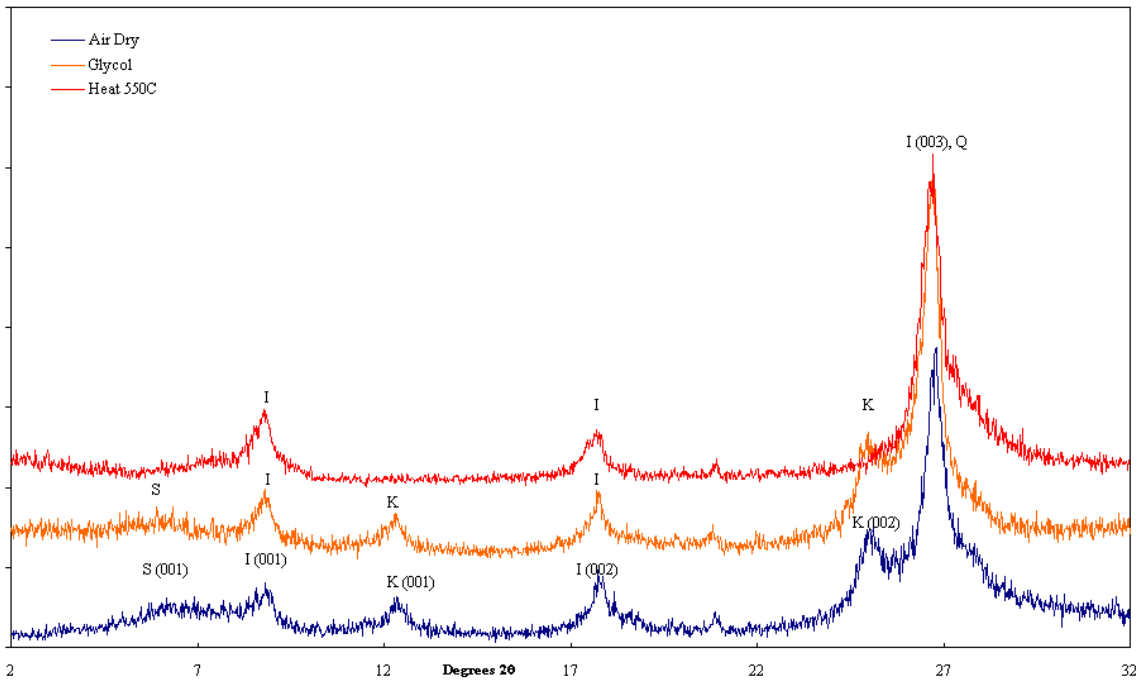

Sample 1H2W 12-14

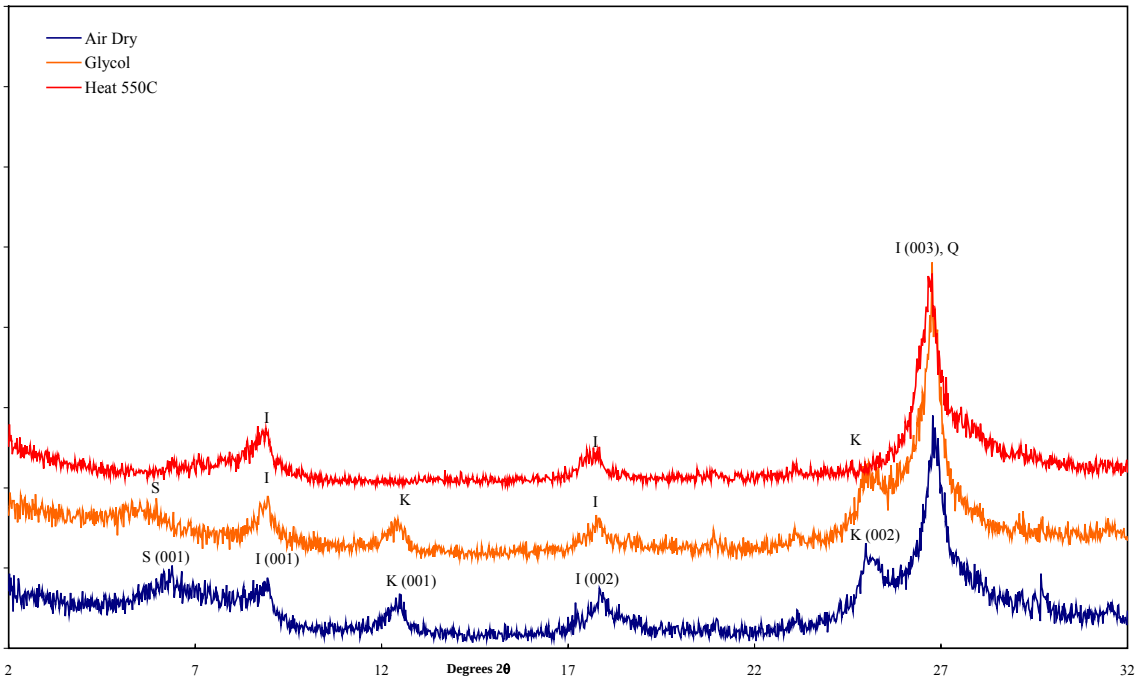

Sample 1H2W 18-20

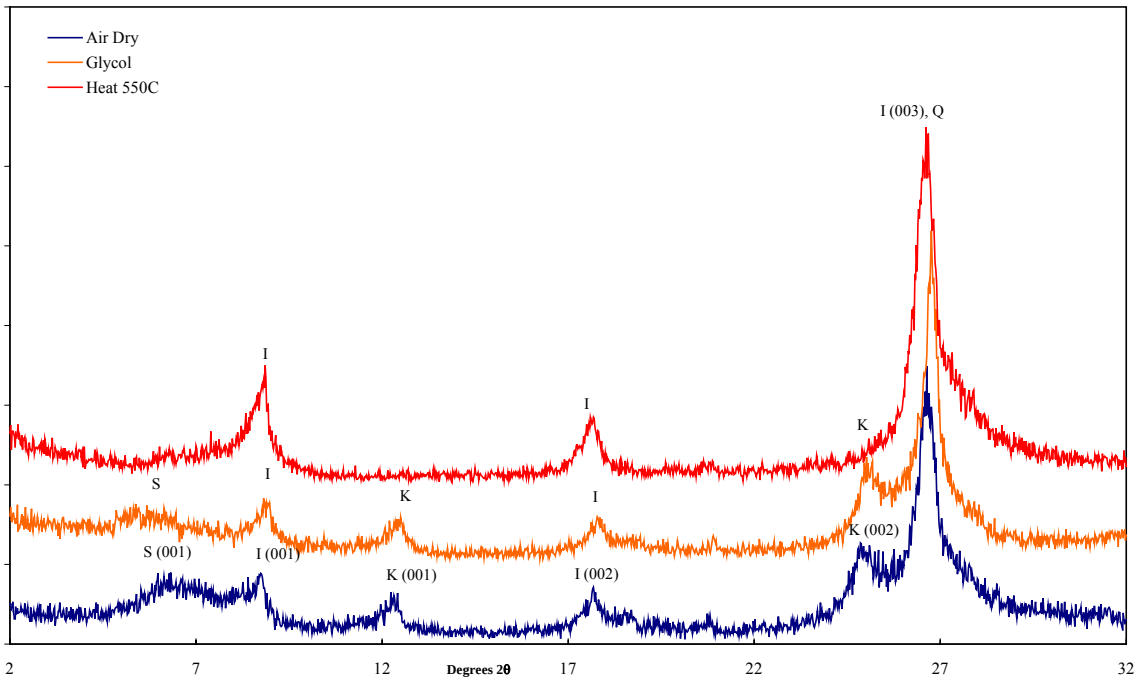

Sample 1H2W 24-26

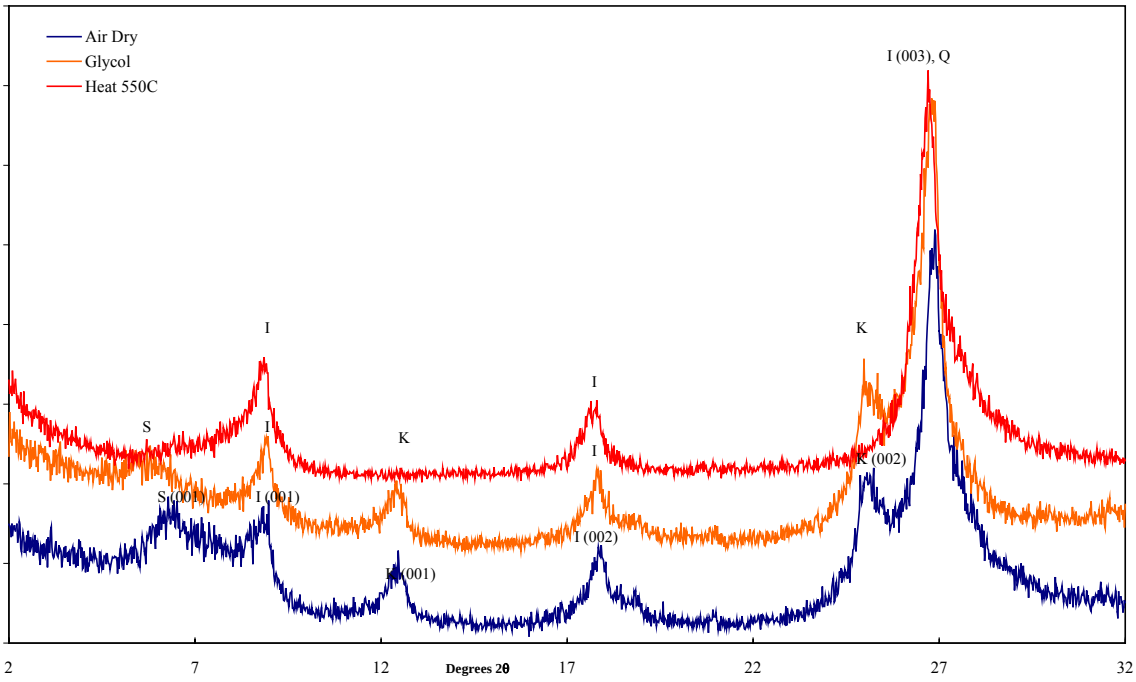

Sample 1H2W 30-32

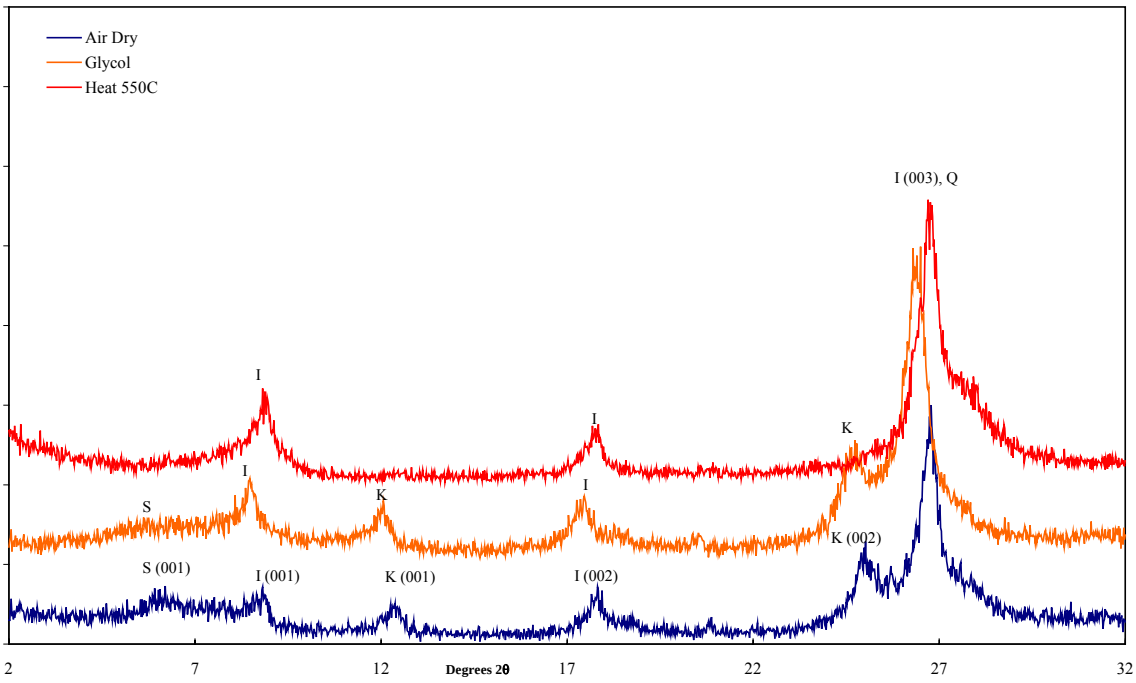

Sample 1H2W 36-38

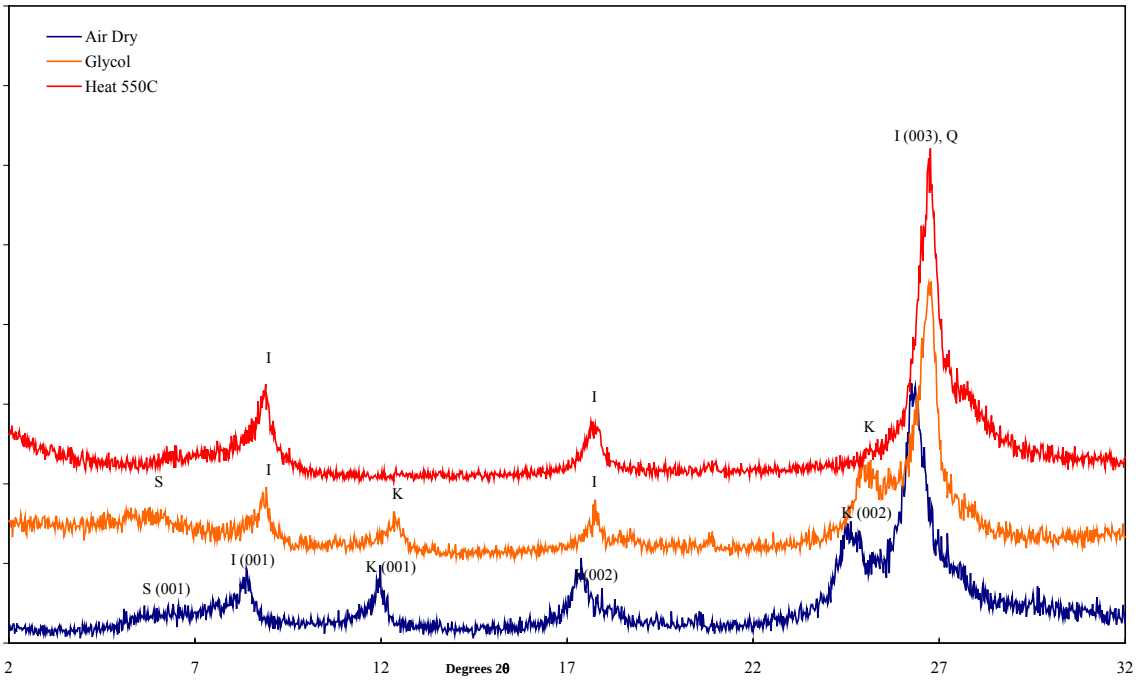

Sample 1H2W 42-44

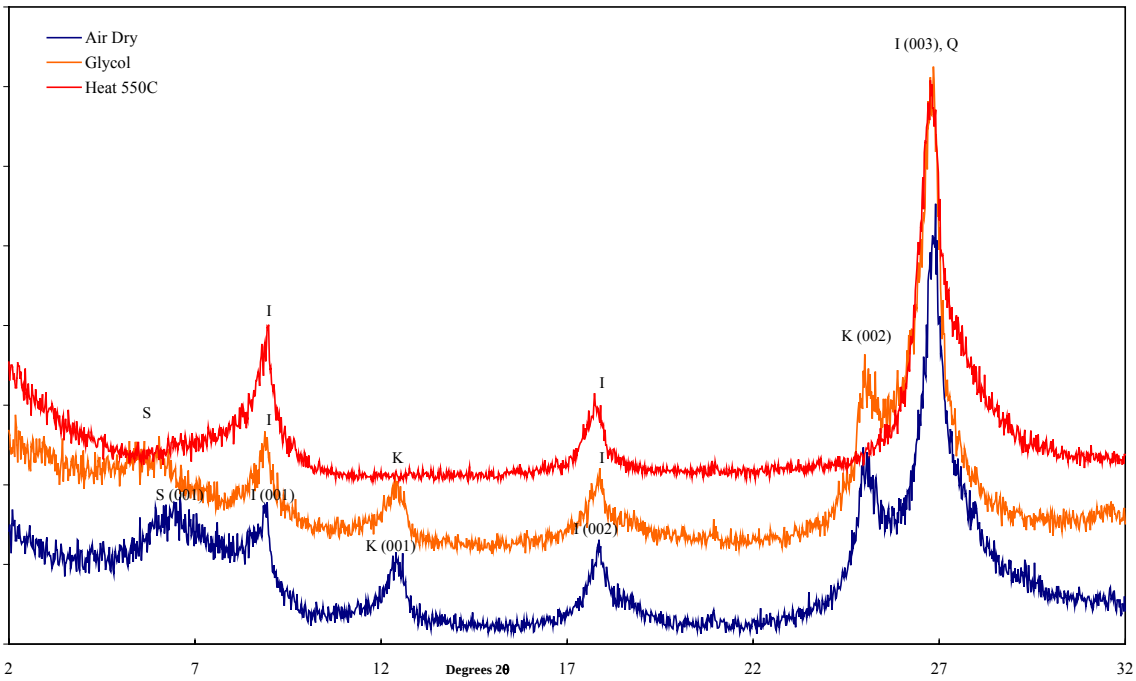

Sample 1H2W 48-50

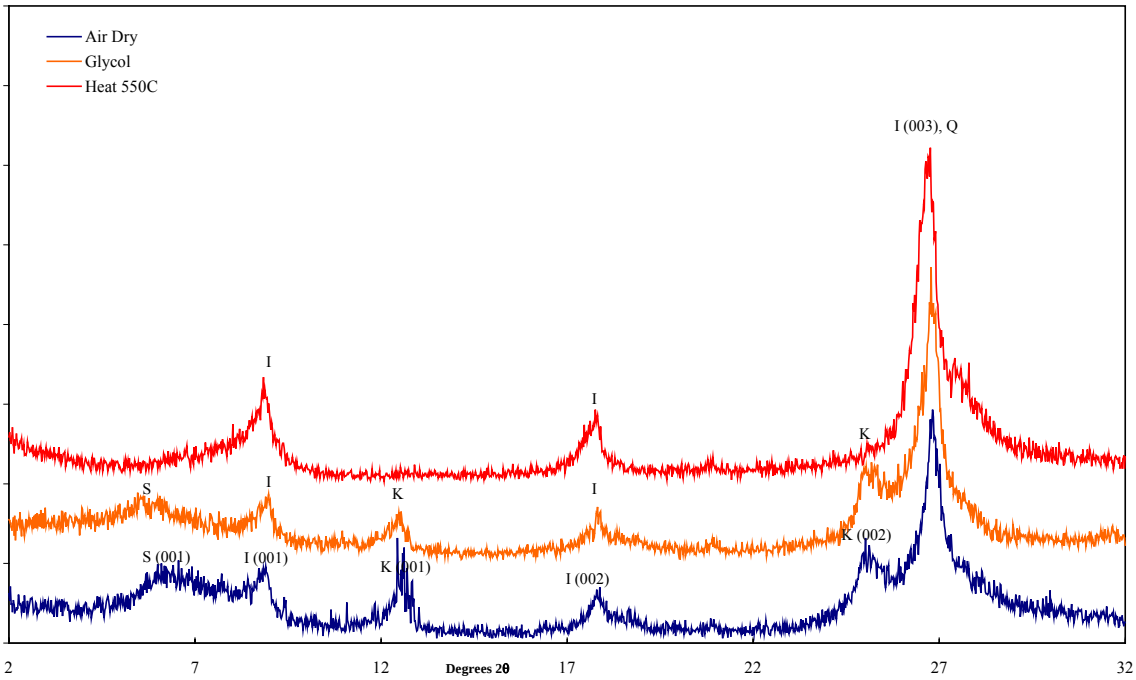

Sample 1H2W 54-56

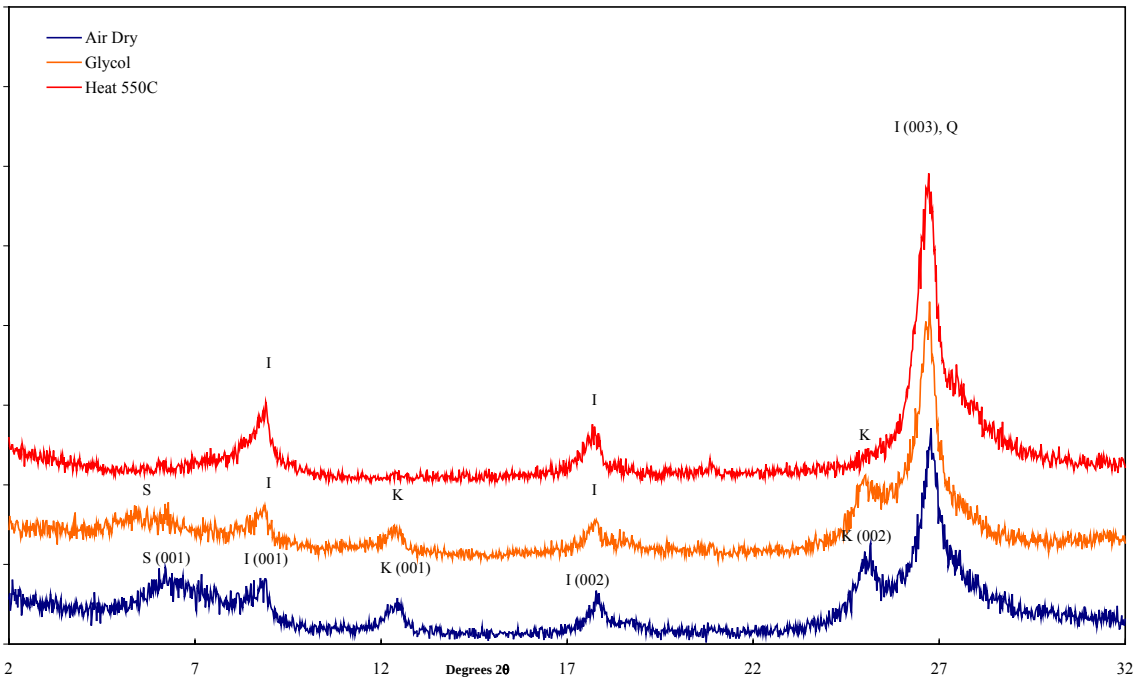

Sample 1H2W 61-63

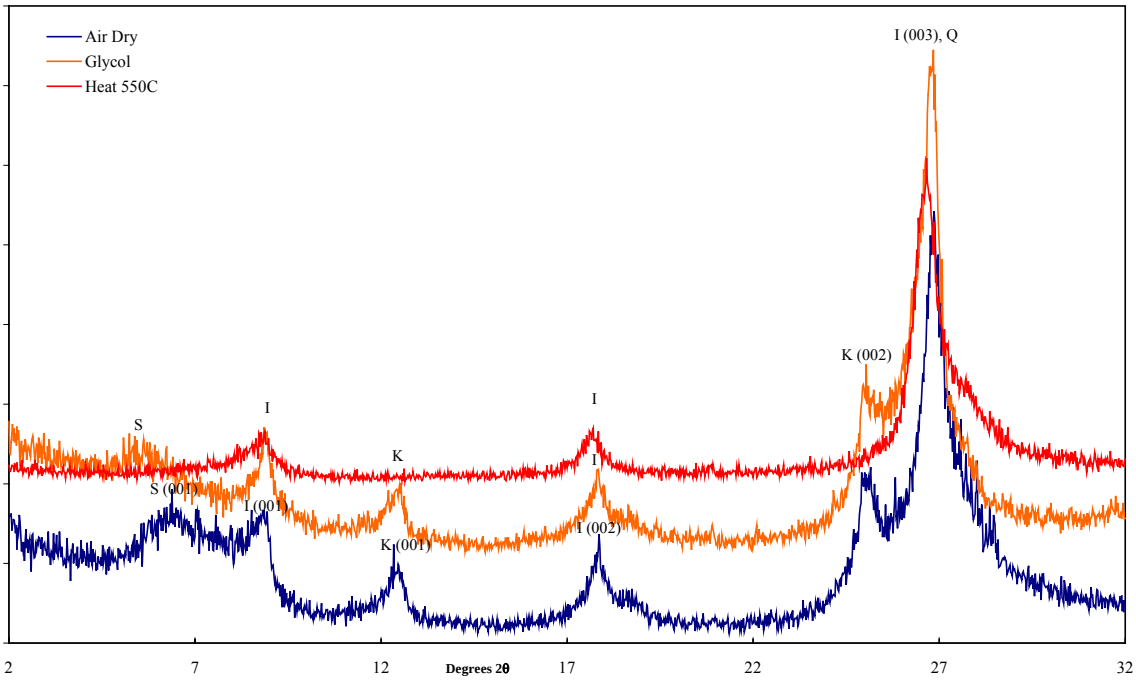

Sample 1H2W 66-68

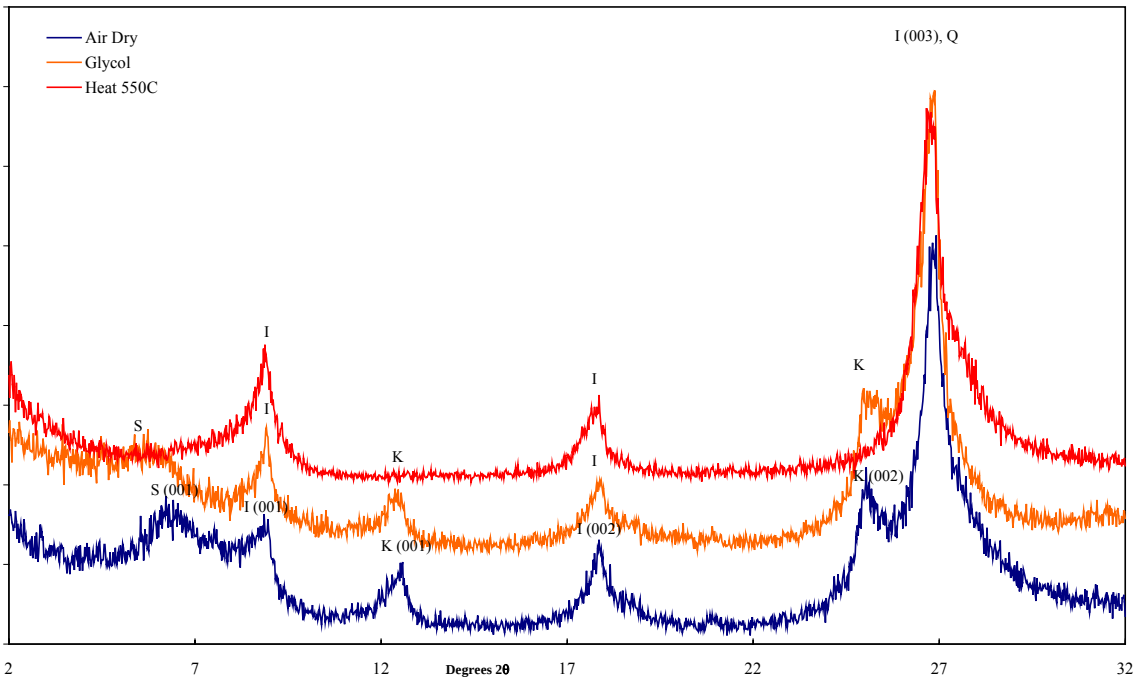

Sample 1H2W 72-74

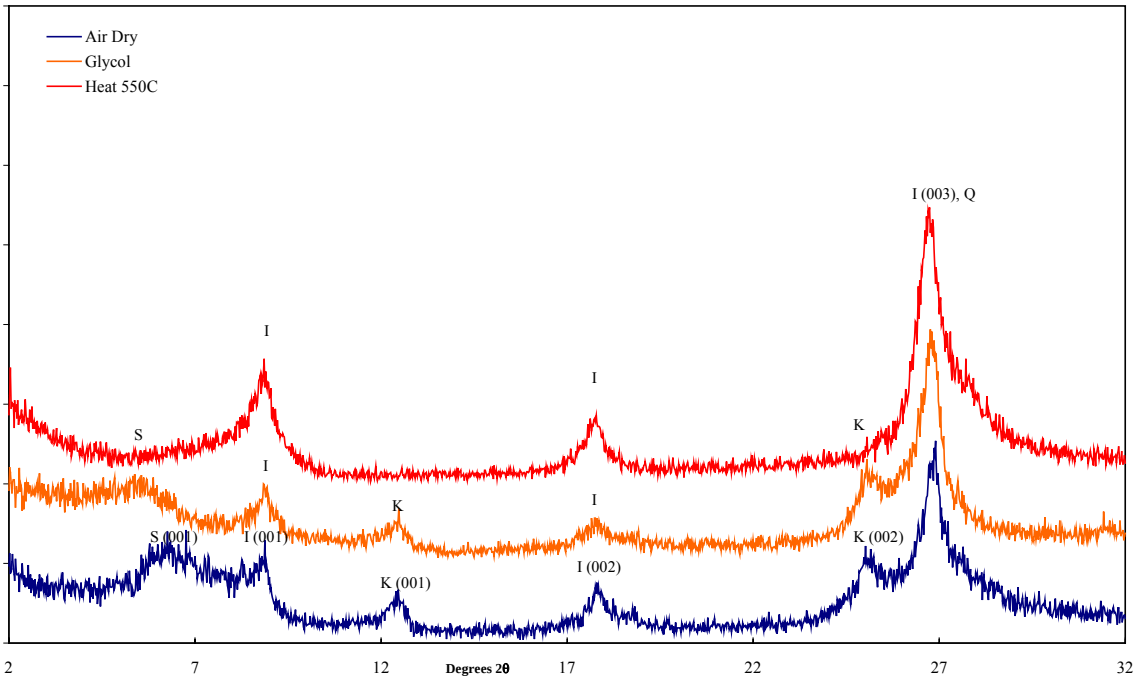

Sample 1H2W 78-80

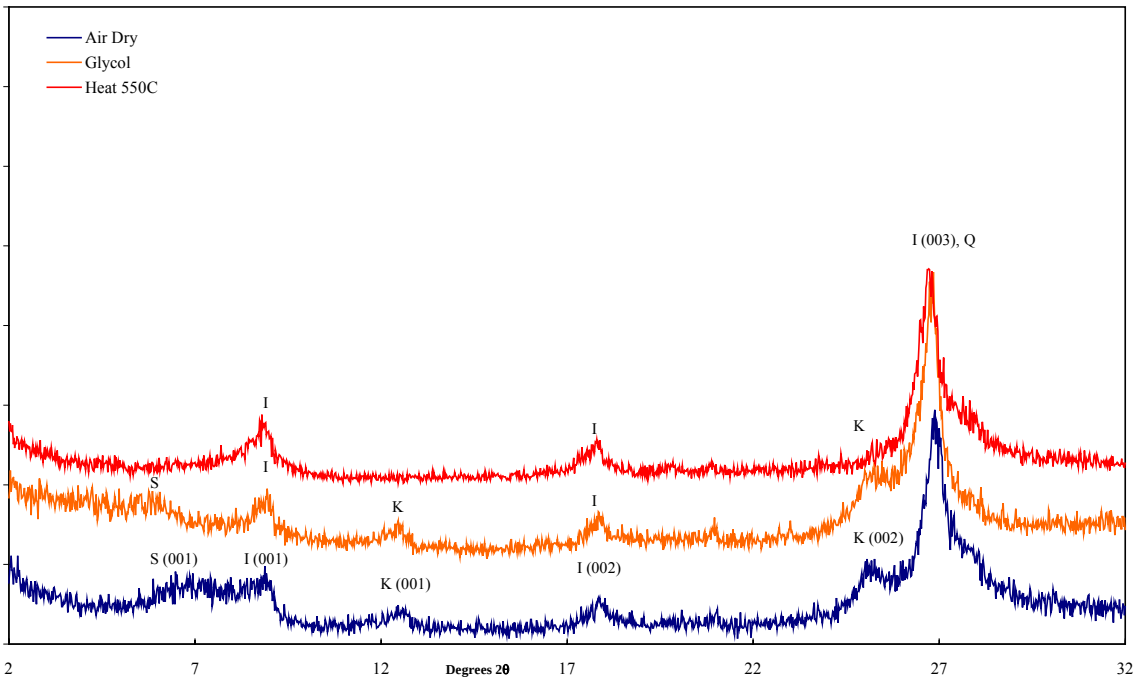

Sample 1H2W 84-86

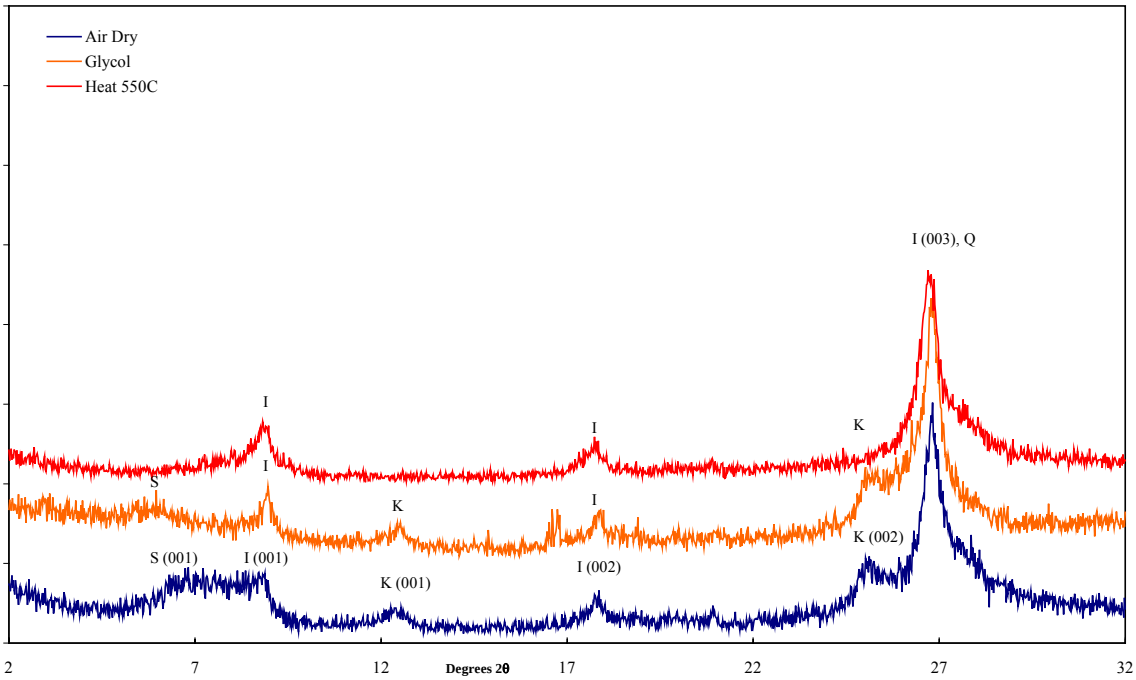

Sample 1H2W 90-92

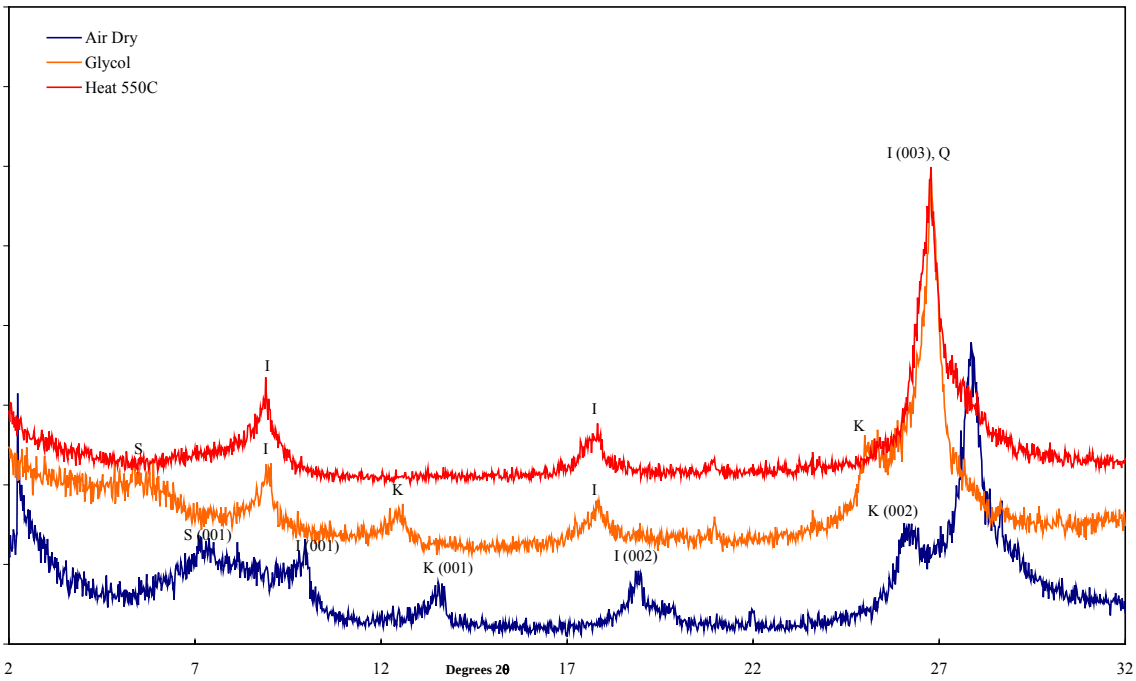

Sample 1H2W 96-98

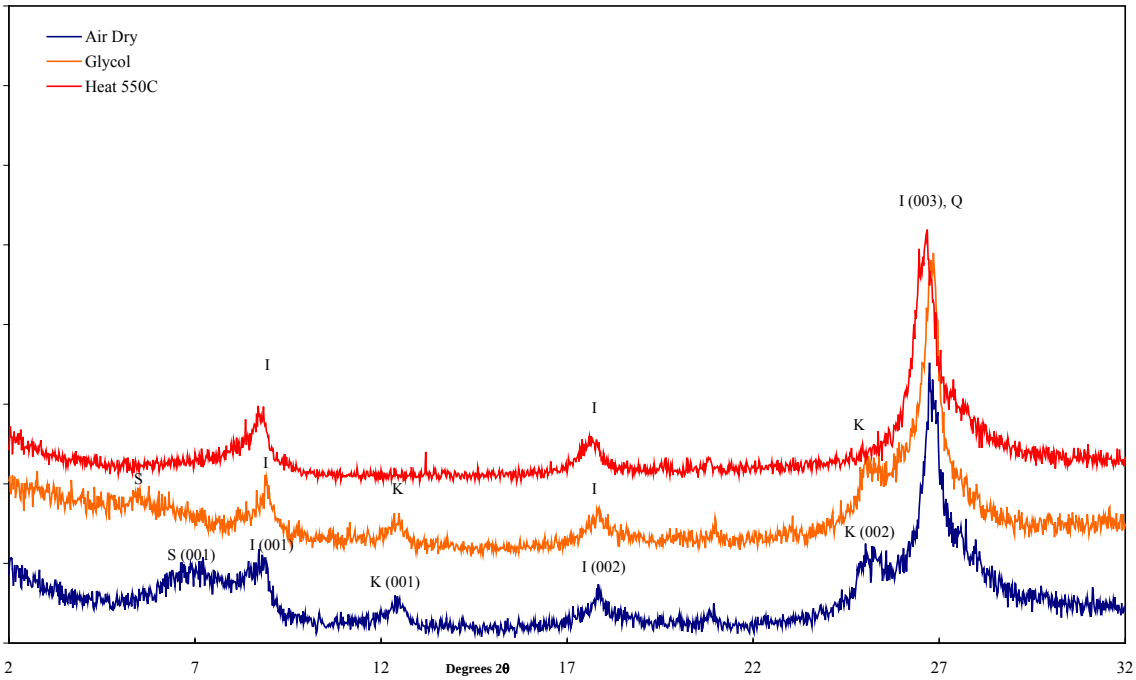

Sample 1H2W 102-104

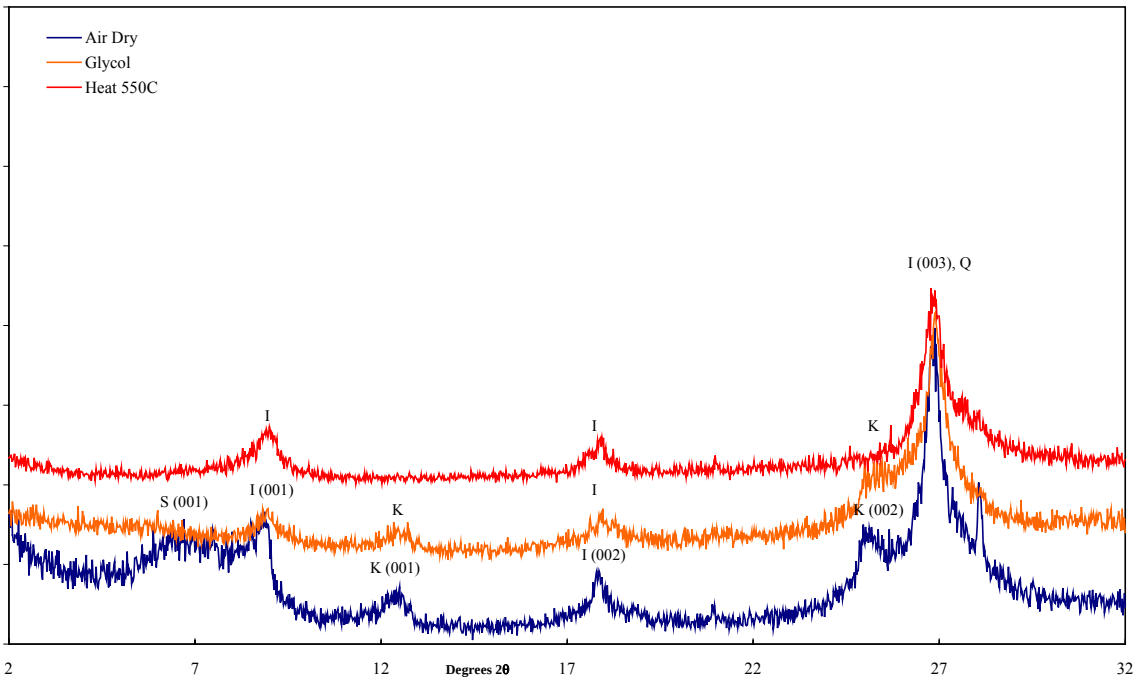

Sample 1H2W 108-110

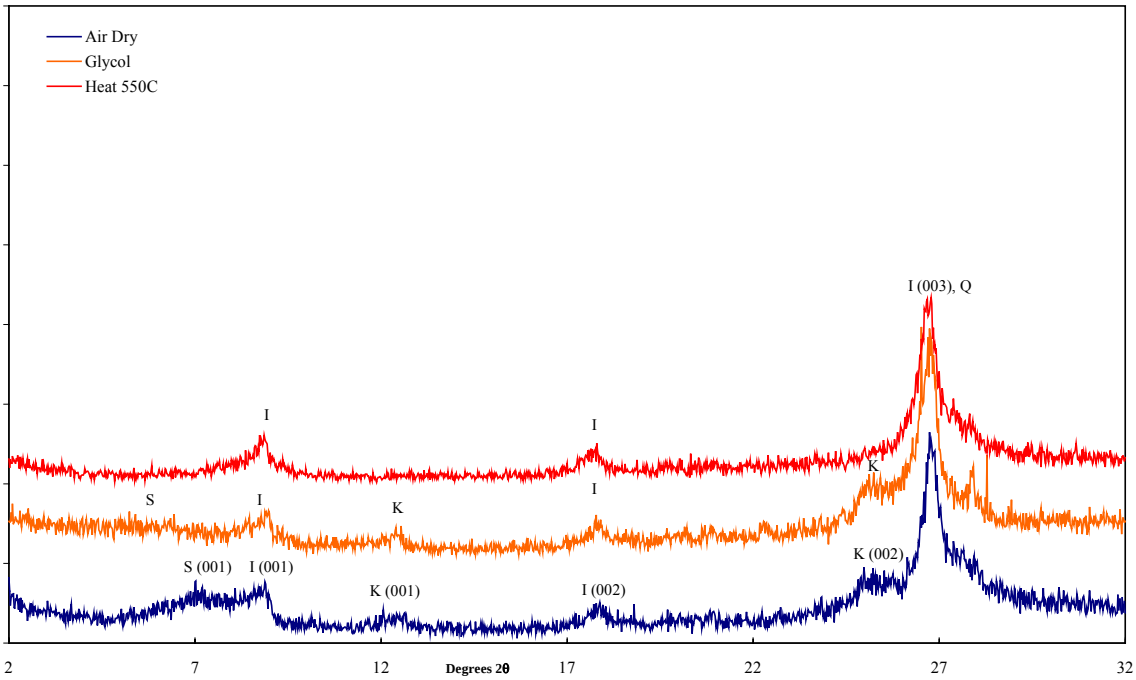

Sample 1H2W 114-116

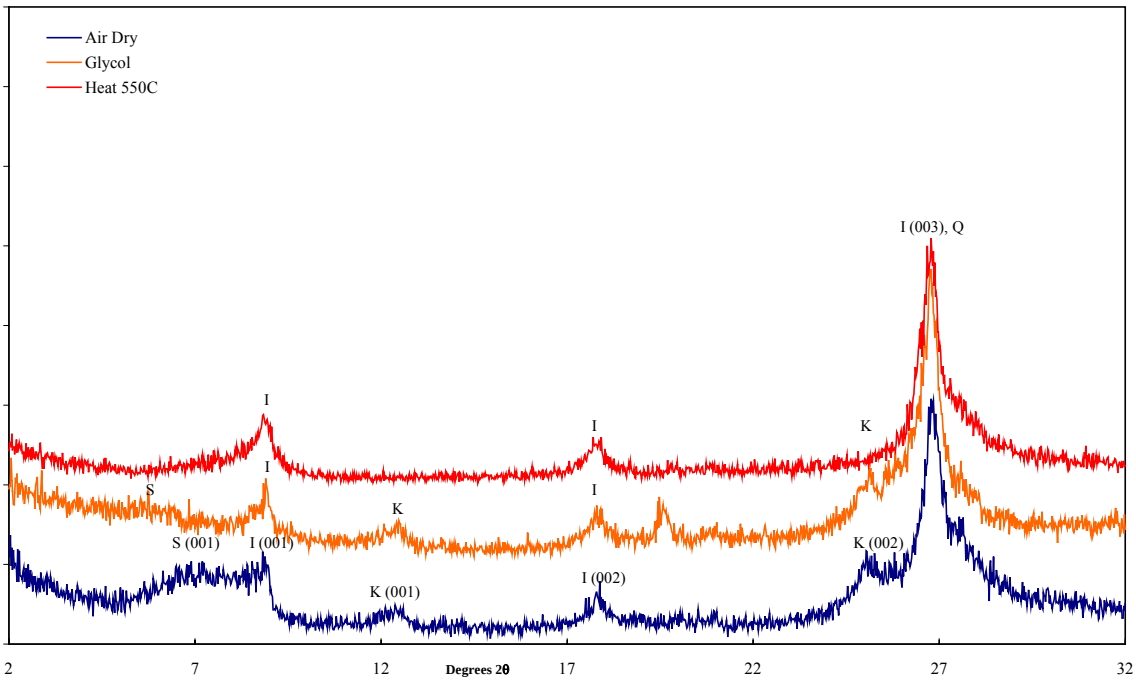

Sample 1H2W 120-122

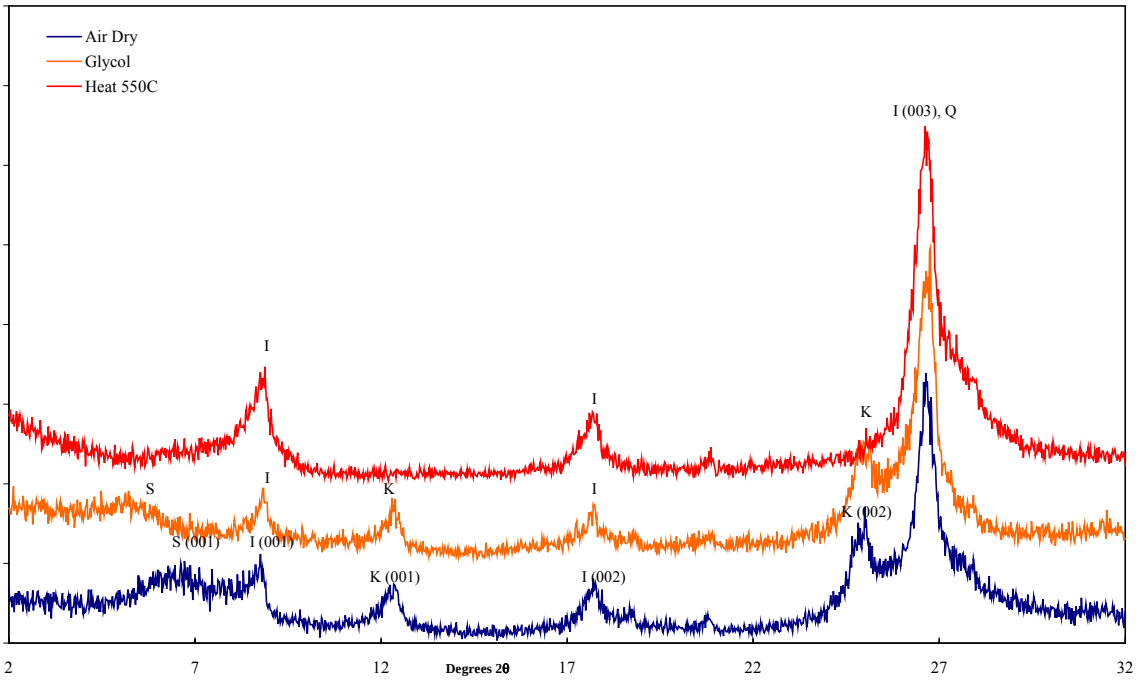

Sample 1H2W 132-134

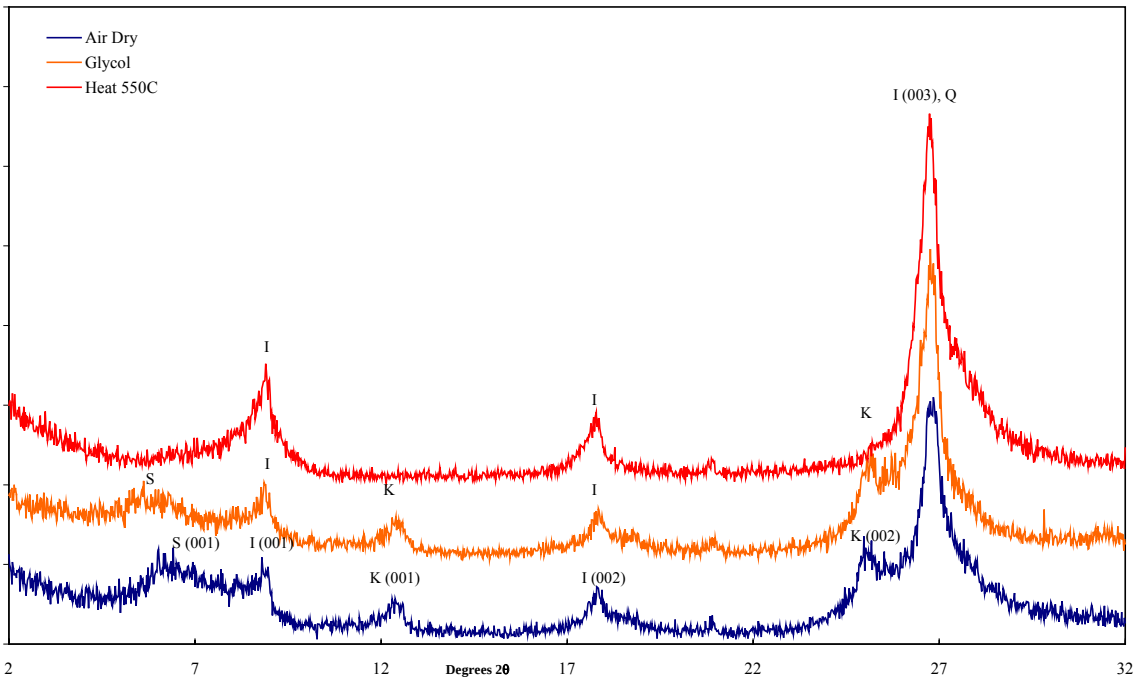

Sample 1H2W 138-140

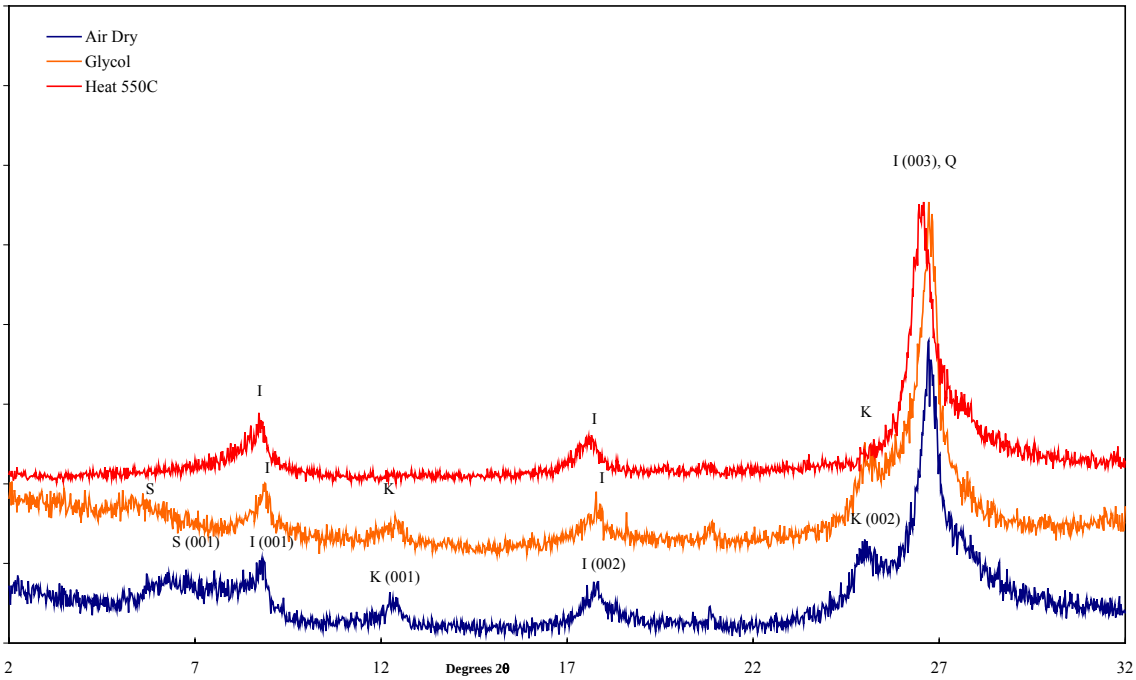

Sample 1H2W 144-146